Doping-driven evolution of the superconducting state from a doped Mott insulator: Cluster dynamical mean-field theory

M. Civelli
Theory Group, Institute Laue Langevin, 6 rue Jules Horowitz, 38042 Grenoble Cedex, France
(Received 29 August 2008; revised manuscript received 11 February 2009; published 15 May 2009)

In this paper we investigate the zero-temperature doping-driven evolution of a superconductor toward the Mott insulator in a two-dimensional electron model, relevant for high-temperature superconductivity. To this purpose we use a cluster extension of dynamical mean-field theory. Our results show that a standard *d*-wave superconductor, realized at high doping, is driven into the Mott insulator via an intermediate superconducting state displaying unconventional physical properties. By restoring the translational invariance of the lattice, we give an interpretation of these findings in momentum space. In particular, we show that at a finite doping a strong momentum-space differentiation takes place: non-Fermi liquid and insulatinglike (pseudogap) characters rise in some regions (antinodes), while Fermi liquid quasiparticles survive in other regions (nodes) of momentum space. We describe the consequence of these happenings on the spectral properties, stressing in particular the behavior of the superconducting gap, which reveals two distinct nodal and antinodal energy scales as a function of doping, detected in photoemission and Raman spectroscopy experiments. We study and compare with experimental results the doping-dependent behavior of other physical quantities, such as for instance, the nodal quasiparticle velocity (extracted in angle-resolved photoemission) and the low-energy slopes of the local density of states and of the Raman scattering response. We then propose a description of the evolution of the electronic structure while approaching the Mott transition. We show that, within our formalism, a strong asymmetry naturally arises in the local density of states, measured in scanning tunneling spectroscopy. We investigate in detail the doping evolution of the electronic bands, focusing on the kinklike quasiparticle dispersion observed with angle-resolved photoemission in specific cuts of the momentum-energy space. We finally show the consequences of the properties presented above in the doping dependence of the Hall resistivity, measured in magnetotransport experiments.

DOI: 10.1103/PhysRevB.79.195113 PACS number(s): 71.10.Fd, 74.20.−z, 74.72.−h

I. INTRODUCTION

High-temperature (H-T_C) superconductors at zero doping can be considered strongly correlated two-dimensional Mott insulators. The understanding of the connection between the superconductor and the Mott insulator hits at the heart of the H-T_C superconducting mechanism.[1] Much effort has been therefore devoted by the scientific community to understand this phenomenon since the discovery of the H-T_C superconductivity in copper-oxide materials in 1986,[2] but its key properties remain still not well understood. On the experimental side, the complexity of H-T_C cuprate materials, which present a rich phase diagram with many competing instabilities, has made it impossible to perform resolutive experiments. On the theoretical side, many theories have been proposed, but a general consensus has not been achieved yet because of the lack of tools capable to perform reliable calculations. The strongly interacting many-body nature of these systems makes, in fact, standard techniques hardly applicable. The recent discovery of high-temperature superconductivity in a family of materials[3] (for a perspective see, e.g., Ref. 4), with a general composition $LaFeAsO_{1-x}F_x$ different from the typical Cu-O plane structure of all known H-T_C compounds, has revitalized the attention on the origin of the H-T_C mechanism.

The aim of this paper is to investigate the doping-driven evolution of the superconducting state of a doped Mott insulator in a two-dimensional lattice model of strongly correlated electrons. To this purpose we employ a cluster extension of dynamical mean-field theory (DMFT) (Ref. 5) (for a review see Ref. 6).

(1) *Dynamical mean-field theory and its cluster extensions to study* H-T_C *superconductivity*. DMFT has in recent years proved very successful in revealing the physics of the Mott transition in three-dimensional compounds,[7] such as, e.g., vanadium oxide. DMFT is a self-consistent mean-field method, which maps a lattice problem onto a single-impurity embedded in a bath of free electrons. It is exact in the limit of infinite dimension, where the physics is purely local and DMFT virtually provides the complete solution. Its strength stands in the ability of treating on the same footing high and low energy physics, capturing in one framework both the Mott insulating state as well as the metallic state, and hence allowing nonperturbative investigations. DMFT has also provided a successful description of the local correlation in magnetically ordered phases, such as, e.g., antiferromagnetism[8–11] (AF) and spiral spin order.[12] It has already proved to be able to capture some of the properties of hole-doped cuprate materials, whenever the momentum dependence included via the one-particle dispersion suffices. For example, in Ref. 11, where the stripe phase of hole-doped cuprates is considered, DMFT has successfully explained the doping-dependent differentiation of spectral weight between the $k=(\pi,0)$ and $k=(\pi/2,\pi/2)$ regions of momentum space. Single-site DMFT in conjunction with electronic structure methods has provided results in excellent agreement with experiments on numerous three-dimensional compounds (with valence electrons in the *sp* shell,[13] 3*d* shell, 4*d* shell,[14]

 ©2009 The American Physical Society

$4f$ shell,[15,16] and $5f$ shell[17]). For some recent reviews of this field, see, e.g., Ref. 18.

In spite of these successes in genuine strongly correlated materials, DMFT has also well understood limitations, mainly due to its purely local character. It does not capture, for example, the feedback of collective modes, such as magnetic fluctuations on the single particle quantities. One consequence of this shortcoming is that the effective mass diverges as the Mott transition is approached, while in finite dimensions exchange effects should remove this enhancement in the region where the renormalized kinetic energy is of the order of the superexchange interaction or the temperature. These effects are negligible whenever strong frustration, finite temperature, or orbital degeneracy helps justifying a local approximation. The DMFT approach, however, breaks down in the cuprate-based superconductors, whose physics is two dimensional and which have a large superexchange. As the Mott transition is approached, in fact, experimental evidence, as, e.g., in angle resolved photoemission spectroscopy (ARPES),[19,20] shows that the effective mass remains finite and that scattering properties are strongly momentum dependent. Being a local theory, DMFT does not describe by construction a strong momentum dependence of the scattering rate. The task of this paper is to improve the local approximation scheme of single-site DMFT by including the momentum dependence of the scattering rate (i.e., of the self-energy), which appears to be an important effect in low-dimensional systems such as the H-T_C superconductors.

Recently, cluster extensions of DMFT capable to go beyond the local approximation have been developed (for reviews see, e.g., Refs. 21–25). The cellular dynamical mean-field theory (CDMFT) (Ref. 26) is a cluster method which retains the real space representation of single-site DMFT but incorporates nonperturbative momentum dependence. It replaces the single site of DMFT by a cluster of impurities, offering the possibility of well describing short-ranged spatial correlation and providing a first correction to momentum-dependent properties. It also allows us to naturally include nonlocal spatial fluctuations of the order parameter of broken-symmetry phases. CDMFT can improve, for example, former DMFT studies on AF (see, for example, Refs. 10 and 27, where the spatial spin correlation is neglected by construction) or introduce into its scheme d-wave superconductivity (dSC) by describing a superconducting order parameter which is sign bond alternating by x- and y-axis inversion. The first cluster-DMFT studies of the Hubbard model in two dimensions were carried out on a 2×2 plaquette in Refs. 23 and 24. These groups have shown the existence of antiferromagnetism, pseudogap, and superconductivity, focusing on relatively small values of the on-site interaction (mostly $U=4t$), for which the Fye-Hirsch quantum Monte Carlo (QMC) (Refs. 28 and 29) method is applicable in implementing the cluster DMFT. One school of thought, for example, in Refs. 30–32, advocates the study of large clusters, at present possible for relatively small interactions. In this latter case, however, it is not yet known what aspects of the Mott physics are captured. Cluster DMFT implemented on the 2×2 plaquette for stronger values of U (the Mott regime) was the subject of several publications[33–36] on the Hubbard model.

(2) 2×2 *plaquette cellular DMFT study*. Following the cluster DMFT studies mentioned above, we focus in this paper on a two-dimensional 2×2 cluster plaquette. According to our viewpoint, elucidating the physical content of the mean-field theory on a plaquette is a very important step to accomplish before proceeding to realistic studies of the actual instabilities that govern the phase diagram of the model. The works in Refs. 37–41 on small clusters have, in fact, shown that there are several competing phases and possible phase separation, which could lead to complicate patterns in real space[42] depending on the boundary conditions or on various terms not explicitly included in the Hamiltonian. A proper investigation of those states in the framework of DMFT-based methods requires therefore an understanding of the pure phases of the simple cluster plaquette.

Implementation of CDMFT on a 2×2 plaquette for large values of the interaction has already revealed several interesting effects not present in single-site DMFT, indicative of a very rich physics. For example, publications[33,34] reveal that the approach to the Mott transition as a function of doping occurs in a very anisotropic way in momentum space. In the Hubbard model (relevant for the description of hole-doped cuprates), the spectral weight disappears much more rapidly in the antinodal than in the nodal region of momentum space, where quasiparticles survive close to the Mott transition at a fixed temperature. Evidence for the formation of a pseudogap in the one electron spectra can be seen in other cluster-DMFT studies.[40,43,44] CDMFT allows a natural interpolation of the nodal and antinodal spectral functions, and it opens the way to study the k dependence of the one-electron spectra in the Mott insulator.[35] The origin of the pseudogap can be traced to the growth of the self-energy in certain parts of k space, where eventually at zero temperature lines of poles of the self-energy (i.e., zeroes of the one-particle Green's function) appear.[45–48] In this latter case, the Fermi arcs observed in ARPES are interpreted as the result of a binding of segments of Fermi surface and of a line of zeroes of the Green's function. Results along those lines beyond mean-field theory can be found in Ref. 49. Within CDMFT not only the underdoped regime is anomalous. At optimal doping, where the maximum of the critical temperature occurs, a maximum in the one electron scattering rate and the presence of power laws in the optical conductivity are found.[50]

(3) *Goals of this paper*. In this paper we study the superconducting state which arises upon doping a Mott insulator by implementing the 2×2 plaquette CDMFT with exact diagonalization[51] (ED-CDMFT) at zero temperature (Lanczos method). Our work is complementary to the 2×2 plaquette CDMFT study in Ref. 52, where the continuous time quantum Monte Carlo (CTQMC) at finite temperature was used as impurity solver. As compared with QMC methods, ED allows us to extract in an unbiased way real frequency quantities, which can be more easily physically interpreted. This turns out to be fundamental in interpreting our CDMFT results and making important connection with experiments (as we will widely present throughout the paper). The Lanczos method, on the other hand, is limited by the finite size of the system used to describe an effective impurity model, associated with the original lattice model (see the

following discussion on the ED-CDMFT procedure). If rightly implemented, however, it is able to well capture the difficult physics of the finite dimensional Mott transition (see, for example, Refs. 18, 53, and 54). We will, in fact, show that the physics described by our results well compares (at least at the qualitative level) with the CTQMC-CDMFT results in Ref. 52, where finite size limitations are absent.

Earlier studies[36,37] with ED-CDMFT have compared the phase diagram of the two-dimensional Hubbard model with the one of cuprate-based materials, focusing on the interplay between the superconducting and antiferromagnetic instabilities, either in the hole- or electron-doped side. In this paper we focus instead on the paramagnetic superconducting mean-field phase by constraining the CDMFT equations, and we study its evolution as a function of doping through all the phase diagram, thus completing the work presented in a previous short publication.[55] The constrains imposed also exclude by construction the possibility of exploring other spontaneous breaking of the square lattice symmetry, such as, for example, stripe formation, dimerization, or flux phases. All these states, including antiferromagnetism, can in principle be investigated within CDMFT once the constrains have been relaxed (see, e.g., for an early study with a two-site cluster DMFT, Ref. 41 and, a recent CDMFT study, Ref. 56). Even if our paramagnetic solution does not represent the real ground state of the system in some region of the phase diagram (e.g., at very low doping we expect definitively antiferromagnetism to take over), under the mean-field viewpoint it is a well-defined problem investigating the physics underlying the evolution of a paramagnetic doped Mott insulator. We leave open the question of what physical term could be added in our model in order to make the physical properties we find the ground-state ones for real materials.

We show in particular that, in a small region around optimal doping, properties appear in the superconducting state which are not ascribable to the standard Bardeen-Cooper-Schrieffer (BCS) theory of superconductivity. The most striking phenomenon, as widely presented in publication,[55] is the rising of two distinct doping-dependent energy scales, which do not fit neither into the framework of BCS approaches nor within the most popular theories of H-T_C superconductivity, such as, for instance, the resonating valence bond (RVB) (Ref. 1 theories for a recent review see, e.g., Ref. 57). We interpret our cluster results extracting the momentum dependence (i.e., restoring the translational invariance of the lattice) of the electronic structure as a function of doping. According to our physical picture, the Fermi liquid description holds at low energies in the nodal region of momentum space, where the d-wave superconducting gap is zero. We show that this fact is best described in momentum space introducing a periodizing scheme based on the local (within cluster) self-energy.[33,58] On the other hand, in the antinodal region, where the d-wave gap is maximal, besides the superconducting contribution, a further contribution to the one-particle gap appears also in the normal component at the finite critical doping. In this case we show that the periodization of another local quantity, the irreducible two-point cumulant, offers a more adequate description.[46,59] We employ therefore a mixed-periodization scheme, which was foreshadowed in a phenomenological approach to the transport properties of cuprate materials in the normal state[60] and in a previous CDMFT publication,[55] and confront the resulting picture of the electronic evolution as a function doping with photoemission, scanning tunneling experiments, and magnetotransport on cuprate materials.

(4) *Setup of the paper*. The paper consists of two main parts. The first comprises of Secs. I–IV. In Sec. I, we present the model and briefly explain the ED-CDMFT method. In Sec. II we present the raw cluster DMFT results, mainly stressing their evolution with doping and showing the appearance (at small doping) of two distinct energy scales. It is not however straightforward to interpret these cluster quantities in terms of physical observables. Therefore, in Sec. III, we cope with the problem of extracting lattice quantities (which can be more easily compared with experimental results) from the corresponding cluster ones, i.e., we present and justify different periodization methods. We show that nodal and antinodal regions of momentum space turn out having different physical properties which require different periodization schemes to be rightly described. In Sec. IV we characterize the different properties in the nodal and antinodal regions, according to the periodization schemes introduced. We link our findings with experimental results from ARPES, showing the doping-driven evolution of quasiparticle spectra and extracting the nodal velocity. We extract also the doping dependence of the nodal Raman response, also measured in penetration depth measurements.

The second part starts from Sec. V, where, in order to be able to compare our results with experiments resolved in momentum space, we employ a more general mixed-periodization scheme. This latter, interlacing the nodal and antinodal properties in all the momentum space, allows us to propose a description of the evolution of quasiparticle spectra in approaching the Mott transition. First the resulting local density of states (obtained by reintegrating over all momentum space) is compared with scanning tunneling experimental results. Momentum-dependent spectra, which are directly comparable with ARPES on the cuprates, are then presented in detail in Sec. VI. In Sec. VII we present peculiar characteristics of the dispersion of the spectra, the so-called "kink" features, also comparing with photoemission results. Finally, in Sec. VIII, by applying a phenomenological Boltzmann approach on our CDMFT mixed-periodization result, we derive the Hall resistivity, which is a direct probe of the charge carries in the system. We compare its evolution as a function of doping with magnetotransport experiments and draw conclusions on a topological phase transition of the Fermi surface, which takes place at low doping within the mixed-periodization scheme introduced in Sec. V. We finally present our conclusions in Sec. IX.

A. Model

We consider the one-band two-dimensional Hubbard model on a square lattice (setting the lattice spacing $a_0=1$ if not otherwise stated),

$$\mathcal{H} = -\sum_{\langle i,j\rangle,\sigma} t_{ij}(c^{\dagger}_{i,\sigma}c_{j,\sigma} + \text{H.c.}) + U\sum_i n_{i\uparrow}n_{i\downarrow} - \mu\sum_i n_i, \quad (1)$$

which is universally considered as a minimal description of cuprate-based materials.[61] Here $c_{i,\sigma}(c^{\dagger}_{i,\sigma})$ are destruction (cre-

ation) operators for electrons of spin σ, $n_{i\sigma}=c_{i\sigma}^{\dagger}c_{i\sigma}$ is the density of electrons, μ is the chemical potential tuning doping, and t_{ij} are the orbital hopping integrals. For convenience's sake we consider only the nearest-neighbor amplitude $t=1$ and a next-nearest-neighbor hopping $t'=-0.3t$. We set the on-site repulsion $U=12t$, larger than the bandwidth $8t$, to be in the Mott regime.

B. ED-CDMFT procedure

Similarly to single-site DMFT,[6] in CDMFT the original model [Eq. (1)] is described in terms of an effective action containing a Weiss dynamical field $\hat{\mathcal{G}}_0(\tau)$ describing the degrees of freedom outside the cluster (in the bath) as a time dependent hopping within the cluster,

$$S_{\text{eff}}=\int_0^{\beta}d\tau d\tau'\Psi_{\tau}^{\dagger}[\hat{\mathcal{G}}_{0\tau-\tau'}^{-1}]\Psi_{\tau'}+U\sum_i\int_0^{\beta}n_{i\uparrow}n_{i\downarrow}d\tau. \quad (2)$$

$i=1,\ldots,N_c$ ($N_c=4$ in the 2×2 plaquette) labels the degrees of freedom inside the cluster. For the case of a 2×2 plaquette considered in this paper, a convenient Nambu-spinor notation has been introduced,

$$\Psi^{\dagger}\equiv(c_{1\uparrow}^{\dagger},\ldots,c_{4\uparrow}^{\dagger},c_{1\downarrow},\ldots,c_{4\downarrow}). \quad (3)$$

With this notation the Weiss field $\hat{\mathcal{G}}_0$ is a 8×8 matrix with both normal (particle-hole) and anomalous (particle-particle) components.[36] Physically, this action describes a cluster embedded in a self-consistent bath of free electrons with dSC correlations. In the CDMFT procedure, a starting guess of the Weiss field $\hat{\mathcal{G}}_0$ is given as input. Then the cluster single-particle propagator $\hat{G}_c$ is computed through the effective action Eq. (2) and the cluster self-energy is determined through the Dyson's equation,

$$\hat{\Sigma}_c=\hat{\mathcal{G}}_0^{-1}-\hat{G}_c^{-1}. \quad (4)$$

Here,

$$\hat{G}_c(\tau,\tau')=\begin{pmatrix}\hat{G}_{\uparrow}(\tau,\tau') & \hat{F}(\tau,\tau')\\ \hat{F}^{\dagger}(\tau,\tau') & -\hat{G}_{\downarrow}(\tau',\tau)\end{pmatrix} \quad (5)$$

is an 8×8 matrix and $G_{ij,\sigma}\equiv\langle-Tc_{i\sigma}(\tau)c_{j\sigma}^{\dagger}(0)\rangle$ and $F_{ij}\equiv\langle-Tc_{i\downarrow}(\tau)c_{j\uparrow}(0)\rangle$ ($i,j=1,\ldots,N_c$ label sites of the cluster) are the normal and anomalous cluster Green's functions, respectively. From the cluster self-energy $\hat{\Sigma}_c$, we use the CDMFT self-consistency condition to recompute the local cluster Green's function $\hat{G}_{loc}(i\omega_n)=\Sigma_K\hat{G}(K,i\omega_n)$, where

$$\hat{G}(K,i\omega_n)=[i\omega_n+\mu-\hat{t}(K)-\hat{\Sigma}_c(i\omega_n)]^{-1}. \quad (6)$$

In Eq. (6) $\hat{t}(K)$ is the Fourier transform of the hopping matrix defined on the lattice formed by the clusters and the sum over K is therefore performed over the Brillouin zone reduced by the partition of the lattice into clusters.[62] We finally rederive a Weiss field,

$$\hat{\mathcal{G}}_0^{new}(i\omega_n)^{-1}=\hat{G}_{loc}^{-1}(i\omega_n)+\hat{\Sigma}_c(i\omega_n) \quad (7)$$

and iterate until convergence is reached.

In practice, as we mentioned in the introduction, in order to solve the cluster impurity problem, in this work (as in Refs. 36 and 55) we use the exact diagonalization method.[51] A parametrized Anderson-impurity Hamiltonian describes the action [Eq. (2)] and couples the cluster impurity with a discrete number N_b of bath orbitals,

$$\mathcal{H}_{\text{imp}}=\sum_{ij\sigma}E_{ij\sigma}c_{i\sigma}^{\dagger}c_{j\sigma}+U\sum_i n_{i\uparrow}n_{i\downarrow}+\sum_{k\sigma}\epsilon_{k\sigma}a_{k\sigma}^{\dagger}a_{k\sigma}+\sum_{ki\sigma}V_{ki\sigma}a_{k\sigma}^{\dagger}c_{i\sigma}+\text{H.c.}+\sum_{ki\sigma}V_{ki\sigma}^{\text{sup}}a_{k\sigma}^{\dagger}c_{i\bar{\sigma}}^{\dagger}+\sum_{ki\sigma}V_{ki\sigma}^{\dagger\text{sup}}c_{i\bar{\sigma}}a_{k\sigma}. \quad (8)$$

Here $E_{ij\sigma}=-\mu\delta_{ij}$, $E_{ij\sigma}=-t\delta_{i,j\pm1}$. We fix throughout this work $N_b=8$, which is the limit in practice accessible with standard computational resources. Though the truncation of the bath represents an important approximation in the ED-CDMFT procedure, as also enlightened in the recent work in Ref. 63, physically meaningful results can be obtained already with minimal size approaches. For example, the "two-site" DMFT introduced in Ref. 64 has demonstrated that a reasonable description of the mean-field physics of the one band Hubbard model in infinite dimension can be obtained with only one bath site. The study in Ref. 41 has extended to a cluster approach the two-site DMFT method (introducing two sites in the cluster and two sites in the bath). The authors have determined the doping-dependent phase diagram of the two-dimensional Hubbard model, which displays a rich variety of competing phases (among which antiferromagnetism, pseudogap, and Pomeranchuk instabilities) close to the Mott transition. The bath-size dependence of our ED-CDMFT method has been previously tested in the one-dimensional Hubbard chain,[53,54] where results could be benchmarked with the exact solution (*Bethe ansatz*[65]) and with density matrix renormalization group calculations. In this latter case we have considered two-site cluster and growth of the size of the bath from two to eight sites. Solution appears evolving toward a stable one,[53,54,63] approaching the infinite-bath solution (result then supported by the QMC-CDMFT study in Ref. 66, where the bath size is ideally infinite). Our results however show that the physical properties are qualitatively well portrayed (as compared with the eight-site bath) already with two site in the bath in the insulating phase and four site in the doped system. We think therefore that $N_b=8$ bath sites is a minimal but physically reasonable dimension for a four-site cluster (see also comments in Ref. 134).

In order to satisfy the self-consistency constraint of Eqs. (6) and (7), the bath parameters $\varepsilon_{k\sigma}$, $V_{ki\sigma}$, and $V_{ki\sigma}^{\text{sup}}$ have to be determined at each CDMFT iteration. In our procedure we fit the Anderson-impurity Weiss field [Eq. (7)] with a N_b-pole bath function $\hat{\mathcal{G}}_{N_b}^{new}(i\omega_n)=i\mathbf{1}\omega-\hat{E}-\hat{\Delta}$,

$$\hat{\Delta}=\sum_k^{N_b}\mathbf{V}_k^{\dagger}(i\mathbf{1}\omega-\hat{\varepsilon}_k)^{-1}\mathbf{V}_k, \quad (9)$$

$$\mathbf{V}_k(2\times 8)=\begin{pmatrix} V_{ki\uparrow} & V^{sup}_{ki\uparrow} \\ -V^{sup}_{ki\downarrow} & -V_{ki\downarrow}\end{pmatrix}_{i=1,N_c}, \tag{10}$$

$$\mathbf{E}_k(2\times 2)=\begin{pmatrix} \varepsilon_{k\uparrow} & 0 \\ 0 & -\varepsilon_{k\downarrow}\end{pmatrix}. \tag{11}$$

The fitting is obtained via a conjugate gradient minimization algorithm, which uses a distance function,[53]

$$f=\sum_{ij}\sum_{n}^{\omega_{max}} |\hat{\mathcal{G}}^{new}_0(i\omega_n)-\hat{\mathcal{G}}^{new}_{N_b}(i\omega_n)|_{ij}/\omega_n, \tag{12}$$

evaluated on the imaginary axis $\omega_n=(2n-1)\pi/\beta$ up to a high cutoff frequency $\omega_{max}\sim 2U$ (involving a number of points $\sim$1024) and emphasizing the lowest frequencies with the $1/\omega_n$ weight. This introduces an effective inverse temperature β, which is a fitting parameter (it is not the real temperature which is $T=0$ in our study) and is set $\beta t=300$ (much higher than the $\beta t=50$ used in publication in Ref. 36) throughout the whole paper. This parameter determines the energy resolution accessed in this work (see also Appendix A). On a practical level, to search for physically sensible solutions in a large parameter space, it is most useful to introduce a reduced parametrization of the bath, which enlightens the symmetries of the input guess $\hat{\mathcal{G}}_0(i\omega_n)$. The constrain on the bath parameters can be then relaxed to allow for other symmetries to be explored. In particular we could verify that the paramagnetic state determined in this work is stable (i.e., is a well-defined mean-field solution) toward other possible breaking of lattice symmetries. Further details are given in Appendix B.

II. CLUSTER RESULTS

We start this section by considering raw cluster quantities, which directly output from the cluster-impurity solution.

A. *d*-wave superconducting state

As we explained above, within CDMFT a superconducting state can be studied by allowing particle-particle pairing terms $V^{sup}_{ki\sigma}a_{k\uparrow}c_{i\downarrow}$ in the impurity Hamiltonian (8) (or equivalently upon a unitary rotation, pairing bath terms $a_{q\uparrow}a_{k\downarrow}$, see Appendix B). CDMFT self-consistency condition may accept nonzero values of the $V^{sup}_{ki\sigma}$ terms, resulting in a nonzero superconducting-pair Green's function $F_{i,j}(\tau)=T_\tau\langle c_{i\uparrow}(\tau)c_{j\downarrow}\rangle$. In drawing a parallel with the classical mean-field example of the Ising model,[6] this is equivalent to assume a nonzero on-site magnetization $m=\langle S^z_i\rangle$ as starting hypothesis in building an effective Hamiltonian and to determine then m self-consistently. As reported in previous work,[36] CDMFT supports indeed a *d*-wave superconducting state in a region of doping that precedes the Mott transition. This is shown in Fig. 1, where we display the doping $\delta=1-\langle n_i\rangle$ versus the chemical potential μ and the *d*-wave order parameter (dOP), defined as $F_{i,i\pm 1}(\tau=0)$, as a function of δ too. As expected, δ versus μ is monotonically decreasing. The dOP has a dome-like shape and its sign is alternating by exchange of the *x*-*y*

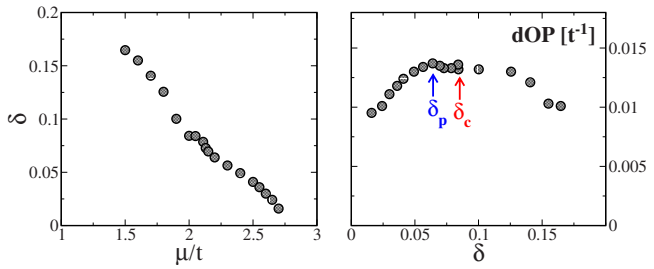

FIG. 1. (Color online) Left panel: doping $\delta=1-\langle n\rangle$ versus chemical potential μ. Right panel: cluster *d*-wave order parameter $(\mathrm{dOP})=\langle\langle c_{i\uparrow}c_{i+1\downarrow}\rangle\rangle_{(\tau=0)}$ as a function of doping δ.

bonds on the cluster plaquette. We can locate the maximum only with some degree of uncertainty around $\delta_p\sim 0.06<\delta<\delta_c\sim 0.08$. The two doping values $\delta_p\sim 0.06$ and $\delta_c\sim 0.08$ present as two special points, which mark changes in the physical properties of the system. We will come back on these two points throughout the paper. Here we stress that at δ_c in particular, our dynamical mean-field result seems to branch two different lines of solution. This is evident either in the δ-μ or the dOP-δ plot. In mean-field approaches this behavior may be the signature of a phase transition. It is therefore intriguing that we find such a behavior close to the maximum of the dOP dome.

Following the nomenclature typical for cuprate materials, we will call hereafter the region $\delta<\delta_p$ as underdoped, $\delta>\delta_c$ as overdoped, and $\delta_p\sim 0.06<\delta<\delta_c\sim 0.08$ as optimal doping region. It is clear that we do not intend to draw a quantitative parallel with cuprate-based systems, where the typical optimal doping (unambiguously defined as the maximum of critical temperature T_C) is around $\delta_c\sim 0.15$, but we rather follow the qualitative aspects of the physics of these materials, marking a correspondence with our CDMFT results on the Hubbard model in two dimensions.

B. Cluster self-energies

It is worth to investigate in detail the cluster outputs. The typical output of the CDMFT scheme is a cluster self-energy $\hat{\Sigma}_c$ [Eq. (4)], which can be expressed as a $2\times N_c\times N_c$ ($N_c=4$ for the 2×2 plaquette) matrix with normal and anomalous components in the Nambu notation introduced in Eq. (3). We first look at the normal components, which are shown on the Matsubara-frequency axis in Fig. 2. The real parts are displayed on the left and the imaginary parts on the right column from high doping for $\delta=0.14$ (the overdoped side in our solution) to close to the Mott transition for $\delta=0.02$ (in the underdoped side). From the top row to the bottom we have the local self-energy Σ_{11}, the next neighbor Σ_{12}, and the nearest-next neighbor Σ_{13}. At high doping, the local components are dominant. We expect in this region that the single-site DMFT is already a good approximation. By decreasing δ, however, also the nonlocal components Σ_{12} and Σ_{13} grow considerably, becoming comparable with the local one. This effect is totally missed by single-site DMFT and it is only captured by using a cluster extension. The growing of the nonlocal normal components of $\hat{\Sigma}_c$ deter-

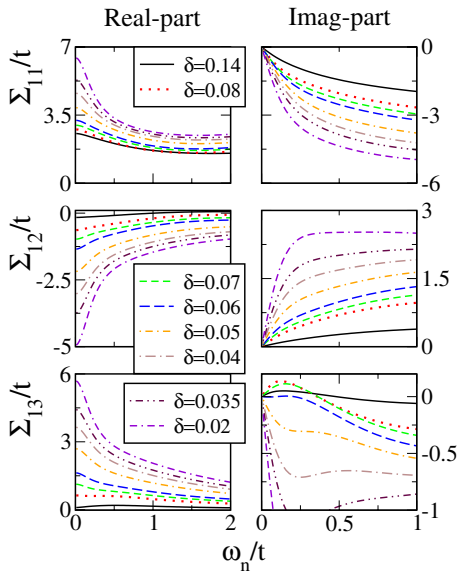

FIG. 2. (Color online) Normal components of the cluster self-energy $\hat{\Sigma}_c$ vs the Matsubara frequency ω_n as a function of doping δ. The real parts are displayed in the left column; the imaginary parts are displayed in the right column. From the top row to the bottom row we show the local Σ_{11}, the next-neighbor Σ_{12}, and nearest-next-neighbor Σ_{13} self-energies.

mines the physical properties of the system in approaching the Mott transition in a fundamental way, as we explain in the following. The imaginary parts (right column) display a low-energy Fermi-liquid-like behavior $\mathrm{Im}\,\Sigma \sim \alpha\omega_n$. The slope α is connected with the quasiparticle residuum (see the following). Here we note that the energy range of linear behavior in the nearest-next neighbor $\mathrm{Im}\,\Sigma_{13}$ is narrower with respect to the other components and that its slope α also changes behavior in passing through the doping $\delta_c \sim 0.08$ (it grows for $\delta < \delta_c$, decreases for $\delta > \delta_c$). α also changes sign for $\delta_p < 0.06$. This behavior is the only mark we find in the cluster self-energy of the special nature of the points δ_c and δ_p that we identified in Fig. 1. The local and next-neighbor components show instead a smooth continuous behavior as a function of doping δ.

As in Refs. 34 and 59, it is convenient to look at the eigenvalues of the cluster-self-energy matrix, which can be directly related to the corner points of the quadrant of the Brillouin zone (as we will explain in more detail in the following section). A convenient way is to re-express the Nambu-spinor notation [Eq. (3)] by grouping 2×2 the up and down spin construction/destruction operators on each cluster site,

$$\Psi^\dagger \equiv [(c_{1\uparrow}^\dagger, c_{1\downarrow}), \ldots, (c_{4\uparrow}^\dagger, c_{4\downarrow})]. \tag{13}$$

The cluster self-energy matrix assumes the form

$$\mathbf{\Sigma}_c = \begin{pmatrix} \hat{\Sigma}_0 & \hat{\Sigma}_{1x} & \hat{\Sigma}_2 & \hat{\Sigma}_{1y} \\ \hat{\Sigma}_{1x} & \hat{\Sigma}_0 & \hat{\Sigma}_{1y} & \hat{\Sigma}_2 \\ \hat{\Sigma}_2 & \hat{\Sigma}_{1y} & \hat{\Sigma}_0 & \hat{\Sigma}_{1x} \\ \hat{\Sigma}_{1y} & \hat{\Sigma}_2 & \hat{\Sigma}_{1x} & \hat{\Sigma}_0 \end{pmatrix}, \tag{14}$$

where the 2×2 matrices are a function of cluster elements $\Sigma_{ij,\sigma} = \Sigma_{|i-j|,\sigma}$,

$$\hat{\Sigma}_0 = \begin{pmatrix} \Sigma_{0\uparrow} & 0 \\ 0 & -\Sigma_{0\downarrow} \end{pmatrix}, \quad \hat{\Sigma}_{1x} = \begin{pmatrix} \Sigma_{1\uparrow} & \Sigma_{ano} \\ \Sigma_{ano} & -\Sigma_{1\downarrow} \end{pmatrix},$$

$$\hat{\Sigma}_2 = \begin{pmatrix} \Sigma_{2\uparrow} & 0 \\ 0 & -\Sigma_{2\downarrow} \end{pmatrix}, \quad \hat{\Sigma}_{1y} = \begin{pmatrix} \Sigma_{1\uparrow} & -\Sigma_{ano} \\ -\Sigma_{ano} & -\Sigma_{1\downarrow} \end{pmatrix}. \tag{15}$$

We follow the procedure used to diagonalize the cluster-self-energy matrix in Ref. 67,

$$\mathbf{\Sigma}_c = \begin{pmatrix} \hat{\Sigma}_{00} & 0 & 0 & 0 \\ 0 & \hat{\Sigma}_{\pi\pi} & 0 & 0 \\ 0 & 0 & \hat{\Sigma}_{0\pi} & 0 \\ 0 & 0 & 0 & \hat{\Sigma}_{\pi 0} \end{pmatrix}. \tag{16}$$

The diagonal elements are linear combination of the original cluster self-energies matrices,

$$\hat{\Sigma}_{00} = \hat{\Sigma}_0 + \tilde{\Sigma}_1 + \Sigma_2,$$

$$\hat{\Sigma}_{0\pi} = \hat{\Sigma}_0 + \tilde{\Sigma}_a - \Sigma_2,$$

$$\hat{\Sigma}_{\pi 0} = \hat{\Sigma}_0 - \tilde{\Sigma}_a - \Sigma_2,$$

$$\hat{\Sigma}_{\pi\pi} = \hat{\Sigma}_0 - \tilde{\Sigma}_1 - \Sigma_2. \tag{17}$$

For convenience's sake we have defined

$$\tilde{\Sigma}_1 = 2\begin{pmatrix} \Sigma_{1\uparrow} & 0 \\ 0 & -\Sigma_{1\downarrow} \end{pmatrix}, \quad \tilde{\Sigma}_a = 2\begin{pmatrix} 0 & \Sigma_{ano} \\ \Sigma_{ano} & 0 \end{pmatrix}. \tag{18}$$

Notice that from Eq. (17) the anomalous self-energy appears only in the $(0,\pi)$ and $(\pi,0)$ components, where we expect the dSC gap to open. The 2×2 eigenvalue matrices of the cluster self-energy are interpreted as describing the four momentum-space points (0,0), $(0,\pi)$, $(\pi,0)$, and (π,π) (hence the choice of the labels), as we will explain in detail in Sec. III.

The normal components of the eigenvalues of $\hat{\Sigma}_c$ are shown in Fig. 3, in a fashion similar to Fig. 2. The first striking difference with respect to Fig. 2 is that the eigenvalue Σ_{00} changes little as a function of doping (either the real or the imaginary part). $\Sigma_{0\pi}$ and $\Sigma_{\pi\pi}$ both grow in reducing doping δ, but the growth in $\Sigma_{\pi\pi}$ is on order of magnitude bigger. This eigenvalue is indeed the one that drives the system into the Mott insulating state as $\delta \to 0$, as evident from the big values of both the real part and the slope of the imaginary part at small doping. This behavior are very similar (i.e., it appears as a smooth continuation) to the one dis-

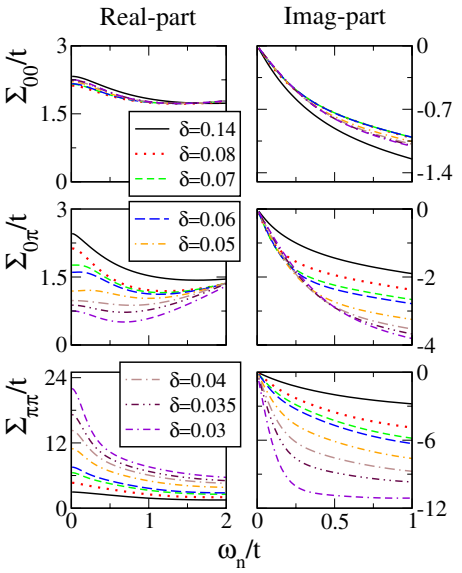

FIG. 3. (Color online) Eigenvalues of the normal component of the cluster self-energy $\hat{\Sigma}_c$ vs the Matsubara frequency ω_n as a function of doping δ. The real parts are displayed in the left column; the imaginary parts are displayed in the right column. From the top row to the bottom we show the self-energy corresponding to the points $k=(0,0)$, $(0,\pi)$, and (π,π) in the first quadrant of the Brillouin zone (see Sec. III).

played by the self-energy of the normal state ED-CDMFT study published in Ref. 34. With respect to this latter study, however, here we display the *normal components of a superconducting solution* (while in Ref. 34 no superconductivity is allowed) and the energy resolution achieved ($\beta t=300$) is an order of magnitude higher than in Ref. 34 ($\beta t=32$). This allows us to extract the very low-energy properties. In particular, as expected by the fact that $\hat{\Sigma}_c$ has to be negative in order to respect causality, we can observe in Fig. 3 that the slope α of the $\mathrm{Im}\,\Sigma \sim \alpha\omega_n$ is always negative. The fact that the $\omega_n \to 0$ behavior of $\mathrm{Im}\,\Sigma$ is linear indicates that these eigenvalues components have Fermi liquid properties. Following a standard Fermi liquid approach, it is instructive to define cluster quasiparticle residua $Z_X=(1-\partial\,\mathrm{Im}\,\Sigma_X/\partial\omega_n)$ with $X=(0,0)$, $(0,\pi)$, and (π,π), even if these quantities have a real physical meaning only in correspondence of a real Fermi surface (i.e., Z_X has to be interpreted here as renormalized cluster quantity). In the standard picture of the Mott transition,[6] the quasiparticle residuum, $Z \to 0$, as doping is reduced, $\delta \to 0$. From Fig. 4 we see that only $Z_{(\pi,\pi)}$ appears to display this behavior, while $Z_{(0,0)}$ and $Z_{(0,\pi)}$ clearly extrapolate to a nonzero value. A last remark concerns once again the special critical doping δ_c, where remarkably the $Z_{(0,\pi)}$ shows a clear change in behavior. For $\delta > \delta_c$ it closely follows $Z_{(\pi,\pi)}$, decreasing with doping as expected in the standard Mott transition picture. At δ_c, however, $Z_{(0,\pi)}$ departs from $Z_{(\pi,\pi)}$ and shows a behavior more similarly to $Z_{(0,0)}$. This once again indicates a quick change in the physical properties of the system in correspondence of δ_c. Later we will discuss the physical interpretation of these observations on the cluster quasiparticle residua (see Sec. IV).

We now turn to the anomalous component of $\hat{\Sigma}_c$, which we show on the left side of Fig. 5 on the Matsubara frequency ω_n. As resulting output of our CDMFT solution, only the real part of the nearest-neighbor component is appreciably nonzero on the Matsubara axis, and it assumes a *d*-wave sign bond-alternating value on the cluster plaquette. $\mathrm{Re}\,\Sigma_{ano}$ starts assuming appreciably nonzero values in the overdoped side $\delta=0.14$ and grows for decreasing doping until $\delta_c \sim 0.08$ is reached. In the underdoped side however at $\delta < \delta_p \sim 0.06$ the curves change tendency, and they decrease by further decreasing doping. The qualitative change in the behavior is better enlightened by looking at the $\omega \to 0$ limit: in the underdoped side the curves reach $\omega=0$ with a finite slope, while in the underdoped side (after $\delta \leq 0.08$) the slope has a smaller value. On right side of Fig. 5 we show the $\omega_n \to 0$ extrapolated value of $\mathrm{Re}\,\Sigma_{ano}$ as a function of doping δ. In first approximation this value can be related to the superconducting gap [as we will explain in detail in Sec. III, see Eq. (30)]. The behavior of the $\mathrm{Re}\,\Sigma_{ano}$ as a function of doping shows therefore to be nonmonotonic and roughly tracks the behavior of the order parameter (see Fig. 1), similarly to standard BCS theory. This result is fundamental and it is in striking contrast with slave-boson resonating valence bond theories,[1,57,68] where the amplitude associated to a particle-particle paring channel is a monotonically decreasing function with doping and it has its maximum close to the insulating transition. In Sec. IV we will better discuss the physical consequences of these results, making connection with recent spectroscopy experiments on cuprate-based materials.

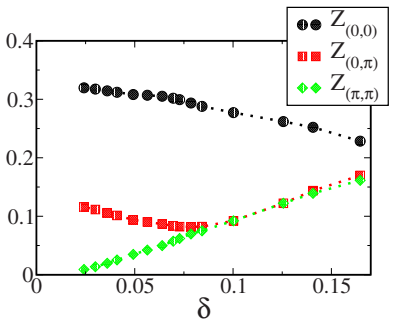

FIG. 4. (Color online) Cluster quasiparticle residua, associated with the eigenvalues of the cluster self-energy matrix, as a function of doping δ.

With the ED-CDMFT procedure it is straightforward to analytically continue on the real axis[6] (differently from other computational methods, such as, e.g., quantum Monte Carlo,

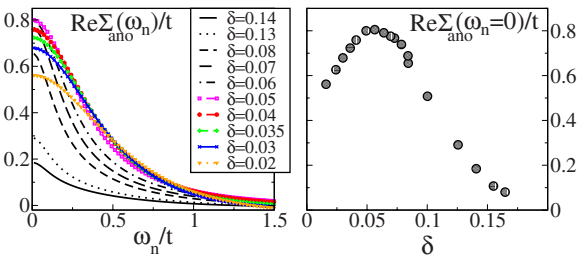

FIG. 5. (Color online) Left panel: real part of the anomalous component of the cluster-self-energy Σ_{ano} (the imaginary part is negligible) vs Matsubara frequency ω_n for different doping δ. Right panel: $\mathrm{Re}\,\Sigma_{ano}(\omega_n \to 0)$ versus doping δ.

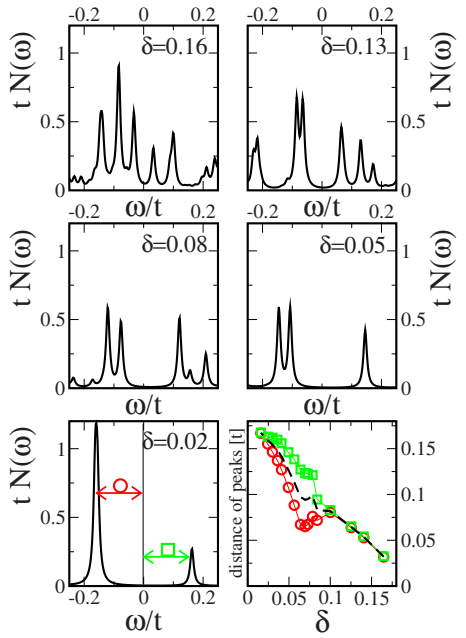

FIG. 6. (Color online) Local density of state $N(\omega)=-\frac{1}{t\pi}\mathrm{Im}[\hat{G}_c]_{11}(\omega)$ obtained from the cluster-impurity solution [Eq. (8)] for various doping δ (from top to bottom). The broadening used for display is $\eta=7\times10^{-3}$. A measure of the energy scale associated with the one-particle gap (always present in the superconducting state) is given by the left (red circle) and right (green square) distances of the ED poles from the Fermi level $\omega=0$. These are displayed as a function of doping δ in the right bottom panel.

which require further approximate methods). The cluster Green's function $\mathbf{G}_c(\omega_n)$ and the cluster self-energy $\mathbf{\Sigma}_c(\omega_n)$ via Dyson's equation [Eq. (4)] are expressed in a pole expansion form containing terms of the form $b/(\omega_n-a)$. To go from the Matsubara to the real axis it is then enough to substitute $i\omega_n\rightarrow\omega+i\eta$, where η is a small broadening introduced to display poles (for more details see Appendix A). The price to pay comes from the discreteness introduced by truncating the bath in the impurity model [Eq. (8)] with a finite number N_b of orbitals. This reproduces continuous functions, such as $\mathbf{G}_c(\omega_n)$ and $\mathbf{\Sigma}_c(\omega_n)$, through a finite number of poles.

In Fig. 6 we display on the real axes the local density of states $N(\omega)=\frac{1}{\pi}\mathrm{Im}[\mathbf{G}_c(\omega)]_{11}$, obtained from the cluster-impurity output [see Eq. (4)], for different doping δ (from top to bottom), using a small imaginary broadening $i\eta=7i\times10^{-3}$. As we will explain in detail in the following section, in a d-wave superconducting state a linear in ω "V-shaped" density of states is expected for $\omega\rightarrow0$. This behavior cannot be captured by the discreteness of our ED-CDMFT solution for small ω; hence we have rather a "U-shape for $\omega\rightarrow0$ given by the broadening η. The shape of $N(\omega)$ and the energy scales of the superconducting gap can however be estimated by the location and intensities of the peaks. So, in looking at $N(\omega)$ from the overdoped side (top row, left panel for $\delta=0.16$) to the underdoped side (bottom row, left panel for $\delta=0.02$) of the phase diagram, we can make interesting observations:

(1) $N(\omega)$ is asymmetric function around $\omega=0$ at low doping ($\delta<\delta_c$). A rather symmetric shape is instead observed around optimal doping $\delta_c\sim0.08>\delta>\delta_p\sim0.06$ (in agreement with previous cluster DMFT results in Ref. 52).

(2) The total superconducting gap, which can be evaluated by measuring the distance of the spectral peaks from $\omega=0$, is increasing by reducing doping δ.

To better elucidate these observations, we have measured the distance from the Fermi level of the left (red circle) and right peaks (green square) and displayed them as a function of doping δ (bottom row, right panel). In the overdoped side ($\delta>\delta_c$) the peaks are equally distant from $\omega=0$, i.e., the superconducting d-wave gap is symmetric at low frequency, as expected in a standard d-wave BCS theory. At optimal doping $\delta_p<\delta<\delta_c$, however, the asymmetry in the gap strikes in, and it is present in all the underdoped side ($\delta<\delta_p$). This is in agreement with the cluster DMFT results obtained in Ref. 52 and it is in nice agreement with scanning tunneling microscope (STM) (Ref. 69) experiments on cuprate materials. The fact that $N(\omega)$ is most symmetric close to optimal doping $\delta\sim\delta_c$ (as evident from the red circle line changing slope as a function of δ) is in line with the observation carried in Fig. 1 on the special nature of the optimal doping region $\delta_p<\delta<\delta_c$ (see also the avoided-quantum-critical-point scenario proposed in the CDMFT study in Ref. 50). The black dashed line is the average of the right and left gaps, and the fact that it is increasing by reducing doping (similarly to the predictions of resonating valence bond slave boson theories[1,57,68]) shows the important result of the presence of another energy scale in our solution, which is different from the energy scale marked by the behavior of $\mathrm{Re}\,\Sigma_{ano}(\omega_n\rightarrow0)$ (see right panel of Fig. 5). The interpretation of these two energy scales brings to interesting physical insights, which can be put in relation with recent experiments on the cuprate materials,[70–77] as presented in a previous short publication.[55] This study is reproposed more in detail in the following sections.

III. MOMENTUM DEPENDENT QUANTITIES: PERIODIZATION PROCEDURES

We want now to interpret the cluster results we presented in the previous section in terms of physical observables, which could be possible related to experiments. The relevant information is typically embodied in the one-particle Green's function, which in a superconducting state can be conveniently written in a Nambu-matrix notation,

$$\mathbf{G}_\sigma^{-1}(k,\omega)=\begin{pmatrix}\omega-\xi_k-\Sigma_k(\omega) & -\Sigma_{ano}(k,\omega)\\ -\Sigma_{ano}(k,\omega) & \omega+\xi_k+\Sigma_k^*(-\omega)\end{pmatrix}. \quad (19)$$

Here $\xi_k=t_k-\mu$ is the free band dispersion of our model [see Eq. (1)]. In order to determine Green's function we need therefore to determine the momentum dependent self-energy from the cluster solution, i.e., we need a periodization scheme. In previous work[33–35] various periodization schemes have been proposed. The idea consists in determining the most local quantity W_r, which can be captured within the dimension of the cluster impurity and construct its truncated Fourier expansion,[22]

$$W_\sigma(k) = \frac{1}{N_c}\sum_{ij} e^{-ik_i} W_\sigma(|i-j|) e^{ik_j}. \quad (20)$$

The smaller the neglected Fourier coefficients are (for $|i-j| > \sqrt{N_c}$), compared to the cluster $W_\sigma(|i-j|)$, the more the k-dependent quantity $W_\sigma(k)$ is well approximated. In the following we present two possible cluster quantities that can be adopted to construct the k-dependent self-energy, showing in which cases they can be considered good local quantities.

A. Self-energy Σ periodization

The cluster self-energy [Eq. (14)] is a natural candidate. It is convenient, for the discussions in the following sections, to recast formula (20) in terms of the cluster eigenvalues [Eq. (16)],

$$\hat{\Sigma}_\sigma(k) = \sum_X \hat{\Sigma}_{X\sigma}\gamma_X(k), \quad (21)$$

where $\hat{\Sigma}_\sigma(k)$ is a 2×2 matrix containing normal and anomalous components,

$$\hat{\Sigma}_\sigma(k) = \begin{pmatrix} \Sigma^{nor}_{k\uparrow}(\omega) & \Sigma_{ano}(\omega) \\ \Sigma_{ano}(\omega) & -\Sigma^{nor}_{k\downarrow}(-\omega)^* \end{pmatrix}. \quad (22)$$

We note that with this formula the cluster eigenvalues $\hat{\Sigma}_X$ are directly related to the corner points in first quadrant of the Brillouin zone $X=(0,0)$, $(0,\pi)$, $(\pi,0)$, and (π,π) [and we justify the notation introduced in Eq. (16)]. $\gamma_X(k)$ are positive functions, such $\Sigma_X \gamma_X(k)=1 \ \forall k$,[46,59]

$$\gamma_{00} = \frac{1}{4}(1+\cos k_x + \cos k_y + \cos k_x \cos k_y),$$

$$\gamma_{\pi\pi} = \frac{1}{4}(1-\cos k_x - \cos k_y + \cos k_x \cos k_y),$$

$$\gamma_{0\pi} = \frac{1}{4}(1+\cos k_x - \cos k_y - \cos k_x \cos k_y),$$

$$\gamma_{\pi 0} = \frac{1}{4}(1-\cos k_x + \cos k_y - \cos k_x \cos k_y). \quad (23)$$

We remark that, by construction, with this procedure we assume that the system is a simple Fermi liquid. We have, in fact, shown in Fig. 2 that the normal components of the eigenvalues of the cluster self-energy have Fermi-liquid behavior ($\mathrm{Im}\,\Sigma_X \to 0$ for $\omega \to 0$). Their simple linear combination extends this property to all the k space. The anomalous component of the lattice self-energy $\Sigma_{ano}(k)$ turns out to have a d-wave shape,

$$\Sigma_{ano}(k) = 2\Sigma_{ano}(\cos k_x - \cos k_y), \quad (24)$$

in agreement with the symmetry of the superconductive gap measured in experiments on cuprates.[19,20]

B. Cumulant $\mathcal{M}$ periodization

In a normal state study of the two-dimensional Hubbard model in Refs. 46 and 59 it has been shown that a more suitable local quantity to describe the Mott transition is the two point irreducible cumulant $\mathcal{M}$, which arises from the atomic limit by perturbatively expanding the hopping term t in Hamiltonian (1). It is simply related to the normal-component lattice self-energy Σ^{nor}_k by

$$\mathcal{M}^{nor}_k(\omega) = \frac{1}{i\omega + \mu - \Sigma^{nor}_k}. \quad (25)$$

In the cluster impurity we have $2N_c \times N_c$ cumulant relations (2 is for the spin degeneracy), conveniently represented by a $N_c \times N_c$ cumulant-cluster matrix $\hat{\mathcal{M}}_{\sigma c}$,

$$\hat{\mathcal{M}}^{nor}_{\sigma c}(\omega) = [(i\omega+\mu)\mathbf{1} - \hat{\Sigma}^{nor}_{\sigma c}]^{-1}, \quad (26)$$

where $\mathbf{1}$ is the $N_c \times N_c$ identity matrix. The eigenvalues of the cumulant matrices are straightforwardly related to the eigenvalues of the self-energy matrices [Eq. (16)],

$$\mathcal{M}^{nor}_X = (i\omega + \mu - \Sigma^{nor}_X)^{-1}, \quad (27)$$

where the notation is again $X=(0,0)$, $(0,\pi)$, $(\pi,0)$, and (π,π). As in Eq. (21), we obtain the lattice cumulant $\mathcal{M}^{nor}_k$ by periodizing the eigenvalues of the cluster cumulants,

$$\mathcal{M}^{nor}_k = \sum_X \mathcal{M}^{nor}_X \gamma_X(k). \quad (28)$$

Inverting Eq. (25), we finally obtained the normal-component lattice self-energy Σ^{nor}_k in the $\mathcal{M}$ periodization.

C. Nodal and antinodal dichotomies: Σ vs $\mathcal{M}$ periodization

It is not trivial to decide whether it is better to periodize the self-energy Σ or the cumulant $\mathcal{M}$. The choice could be strongly dependent on the physical properties of the system, which are not *a priori* well known. It is not trivial either understanding *a priori* to which extend the two approximated schemes could be able to describe such properties. In this case, we rely on experimental results on cuprate materials, such as, e.g., the already mentioned ARPES,[19,20] to fix a physically reasonable starting hypothesis. It is a well established experimental fact that approaching the Mott insulator the normal state Fermi surface (measured at temperatures above T_C) breaks up, displaying well-defined quasiparticles in the regions (nodes) close to the centers of the quadrants of the Brillouin zone $k \sim (\pm\frac{\pi}{2}, \pm\frac{\pi}{2})$, while quasiparticles disappear in the strong scattering regions (antinodes) close to the corners of the quadrants $k \sim (0, \pm\pi)$ and $(\pm\pi, 0)$. Besides photoemission experiments, measures of transport properties show anomalous (non-Fermi liquid) power-low exponents in the temperature dependence, especially in the underdoped regime of cuprate materials. In this case, a series of phenomenological approaches, which try to explain these experimental observations in the framework of Boltzmann theory,[60,78–80] has been based on dividing the momentum space in regions of high quasiparticle scattering rate, *hot spots* around the antinodal points, and regions of low quasiparticle scattering rate, *cold spots* around the nodal point, where quasiparticles have a much longer lifetime. The simple idea underlying this choice is that the nodal region

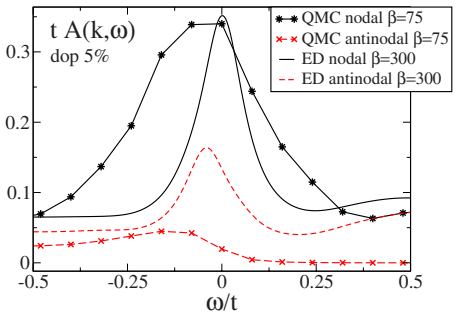

FIG. 7. (Color online) We compare the nodal and antinodal quasiparticle peaks obtained from the normal component of the superconductive ED-CDMFT solution at zero temperature and the QMC-CDMFT normal state solution at much higher temperature T ($\beta = t/T = 75$). The functions on the real axis with QMC are obtained with the maximum entropy method. To display the ED-CDMFT curves the slightly ω-dependent broadening $\eta(\omega) = 0.075 + \omega^2$ was used (see discussion in Appendix A).

behaves as a standard Fermi liquid, while the system in the antinodal region is like an insulating state.

This *nodal/antinodal dichotomy* fits into the CDMFT frame as the natural path taken by the system to approach the doping-driven Mott transition.[34,35,46,59] This is a general property independent of the periodizing scheme adopted. Some important differences however hold between the Σ and the cumulant $\mathcal{M}$ periodizations, which we will illustrate in the following.

In Fig. 7 we show, for example, the spectral functions $A(k,\omega) = -\frac{1}{\pi} \mathrm{Im}\, G_k^{nor}(\omega)$ in the nodal $k \sim (\frac{\pi}{2}, \frac{\pi}{2})$ (black continuous line) and antinodal $k \sim (0, \pi)$ (red dashed line) points of momentum space, obtained via $\mathcal{M}$ periodization for the case $U/t = 12$, $t' = -0.3t$, and 5% doping. We confront our zero temperature ED-CDMFT result with a QMC-CDMFT (Refs. 33 and 81) at much higher temperature ($T = t/75$), where the system is in the normal state. In the ED case we have extracted the normal part of the superconducting solution [setting $\Sigma_{ano} = 0$ in Eq. (19)], interpreting it as a low-temperature normal state parent of the high-temperature QMC solution. This is far from being a trivial statement, as the normal component of a superconducting solution is not generally a normal state solution. Our aim in this picture is, however, to present a qualitative comparison between two very different impurity solving methods in two very different regimes to show the generality and solidity of the nodal/antinodal dichotomy concept. This figure serves also to compare results of maxent analytic continuation of Fye-Hirsch QMC scheme with the ED results at low temperatures. The qualitative agreement is reasonably good, supporting the observation we made above on experimental results and the dichotomy nature of the physical properties in this system.

We observe in particular in Fig. 7 that the antinodal quasiparticle peak is very broad in the high-temperature QMC solution, denoting a short lifetime of quasiparticles, while it is sharper in the low-temperature ED solution, much more than the narrowing due to the different temperature (we have scaled the heights of the peaks taking the high of the nodal quasiparticle peak as reference to fix the scale between the ED and QMC curves). This goes in the direction of ARPES experimental observations, which show a sharpening of the antinodal quasiparticle in going from the normal to the superconductive state[82] by decreasing temperature. We finally point out that with the $\mathcal{M}$ periodization used in Fig. 7, in the antinodal point the quasiparticle peak shifts to negative energies, opening a pseudogap. This is also in line with the above mentioned ARPES observations. On the contrary, by using the Σ periodization the antinodal peak always remains (for all dopings) at the Fermi level but with reduced spectral weight compared to the nodal point.[34]

All these observations, either from experimental facts or from the output of our method, point toward a dichotomy of the nodal and antinodal regions of momentum space, which show different coherence energies. The nodal region has the highest coherence scale and sharp quasiparticles. In the antinodal region a pseudogap opens in the spectrum, and quasiparticles, if present at the gap edge, are more broad and incoherent. It is therefore natural to assume that the Fermi-liquid nodal region is better portrayed by the Σ periodization (which as we mentioned above describes a Fermi liquid by construction), while the antinodal insulating region is better described by the $\mathcal{M}$ periodization (as shown in Fig. 7).

Taking this last assumption as starting point, we compare the results of the Σ and $\mathcal{M}$ periodizations, stressing virtues and defaults in the frame of the physical observations carried above. A stringent test is given by reconstructing the local density of states $N(\omega) = -\frac{1}{\pi} \Sigma_k \mathrm{Im}\, G_k(\omega)_{11}$ [where $G_k(\omega)$ is obtained by Eq. (19)], which can be compared with the local Green's function $G_{imp} = (\hat{G}_c)_{11}$, obtained directly in the cluster-impurity solution. This test is presented in Fig. 8. First, it is once again instructive to separately study the normal component of the superconducting state by setting $\Sigma_{ano} = 0$ in Eq. (19). We focus the attention on a small-doping case $\delta = 0.05$ close to the Mott transition point. The top panel displays a full energy range which includes the lower Hubbard band (LHB) and upper Hubbard band (UHB). The cluster-impurity density of states $N(\omega)$ is represented by the continuous black line, the $\mathcal{M}$-periodization result by a red dotted-dashed line, and the Σ-periodization result by a green dashed line. Already at small doping, in the region labeled A, the formation of a Mott gap is visible in the cluster solution. The $\mathcal{M}$ periodization is capable to describe this part of the spectrum quite well (matching the continuous black line of the impurity result). On the contrary, the Σ periodization creates artificial states in the Mott gap. This is true also at low energy (region labeled B). A closeup on the Fermi level ($-t < \omega < t$) is displayed in the middle panel (with again $\Sigma_{ano} = 0$). The $\mathcal{M}$ periodization reproduces the formation of a low-energy pseudogap in the normal component of the spectra, as already remarked in previous normal-state studies,[46,59] while, once again, the Σ periodization introduces artificial states that fill the pseudogap. This simple test therefore evidences the failure of the Σ periodization in well describing the high- and low-energy normal components of Green's function, in the regions of momentum space where a pseudogap is present, like in the antinodal k point of Fig. 7. The scenario is different if we look at the low-energy *superconducting* density of states $N(\omega)$ by restoring $\Sigma_{ano} \neq 0$ in Eq. (19), as presented in the bottom panel of Fig. 8. Here it

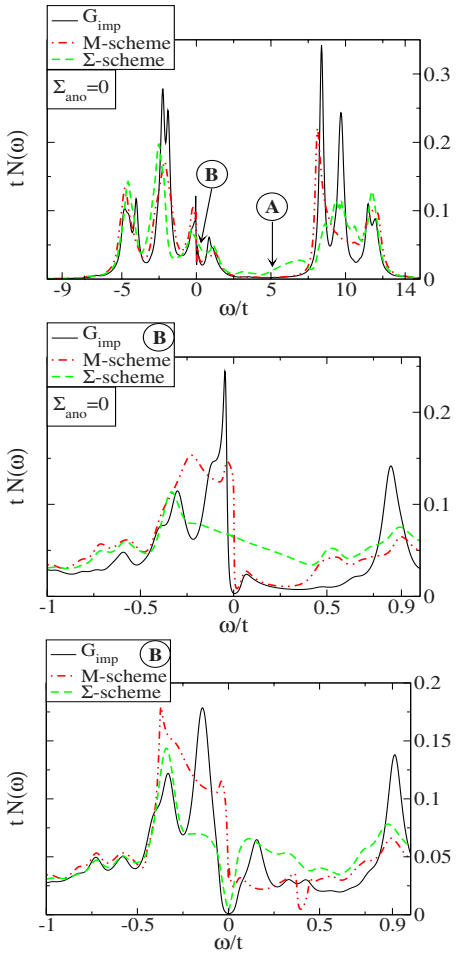

FIG. 8. (Color online) Top panel: reconstructed local density of states $N(\omega)=-\frac{1}{t\pi}\Sigma_k G_k^{nor}(\omega)$ for the normal component ($\Sigma_{ano}=0$) of Green's function at small doping ($\delta=0.05$). $G_k^{nor}(\omega)$ has been obtained by either the cumulant $\mathcal{M}$ periodization (red point-dashed line labeled $\mathcal{M}$ scheme) and by the Σ periodization (green dashed line labeled Σ scheme) and confronted with the local density of states of the cluster-impurity solution (black continuous line). Middle panel: closeup at the Fermi level. Bottom panel: the local density $N(\omega)$ of states of full superconducting solution ($\Sigma_{ano}\neq 0$) selects in the k summation only the nodal points. A low-energy confront with the cluster-impurity solution shows a different matching of the cumulant and self-energy periodizations with the cluster-impurity result. The display on the real axis of Green's function has been obtained by introducing a ω-dependent broadening $i\eta(\omega)$ (see Appendix A for details).

is the Σ-periodization line (green dashed line) which better portrays the cluster spectrum (black continuous line). The $\mathcal{M}$ periodization this time introduces spurious states close to the Fermi level ($\omega=0$). This is not contradictory with respect to the result presented above on the normal component of the system (top and middle panels). By adding the d-wave superconducting gap, in fact, we select at low energies ($\omega\rightarrow 0$) only the region of momentum space close to the nodal points, where the gap is zero. These points dominate, in fact, the sum $-\frac{1}{\pi}\Sigma_k \mathrm{Im}\, G_k(\omega)_{11}$. $N(\omega)$ for $\omega\rightarrow 0$ is therefore a direct probe of the nodal point behavior only (while without superconducting gap, i.e., $\Sigma_{ano}=0$, all k points eventually contribute in the summation at low energies).

We clarify this last statement. Let us assume as starting point that at the nodes quasiparticles are well defined on the full range of doping. We can extract from Eq. (19) the low-energy ($\omega_n\rightarrow 0$) Green's function

$$\mathrm{Re}\,\Sigma_k(\omega_n)\sim \mathrm{Re}\,\Sigma_k(0),$$

$$\mathrm{Im}\,\Sigma_k(\omega_n)\sim (1-Z_k^{-1})\omega_n,$$

and

$$G(k,\omega_n)\sim \frac{\frac{Z_k}{2}(1-\tilde{\xi}_k/E_k)}{i\omega_n+E_k}+\frac{\frac{Z_k}{2}(1+\tilde{\xi}_k/E_k)}{i\omega_n-E_k}. \quad (29)$$

For convenience's sake, we have enlighten the quasiparticle dispersion,

$$\tilde{\xi}_k=Z_k[\xi_k+\mathrm{Re}\,\Sigma_k(0)],$$

$$E_k=\sqrt{|\tilde{\xi}_k|^2+|Z_k\Sigma_{ano}(k,0)|^2}. \quad (30)$$

The nodal point is the only one gapless at low energies and the quasiparticle spectrum can be linearized [Eq. (30)],

$$E_{k_{nod}}=\sqrt{|\tilde{\xi}_{k_{nod}}|^2+|Z_{k_{nod}}\Sigma_{ano}(k_{nod})|^2}=\sqrt{v_{nod}^2k_\perp^2+v_{ano}^2k_\parallel^2}. \quad (31)$$

$v_{nod}=|\nabla_k\tilde{\xi}_k|$ is the quasiparticle Fermi velocity perpendicular to the Fermi surface and $v_{ano}=Z_{nod}|\nabla_k\Sigma_{ano}(k)|$ is parallel to the Fermi surface. After analytic continuation $\omega_n\rightarrow\omega+i\eta$, it is now easy to calculate the low-energy behavior of the one-particle density $N(\omega)=\frac{1}{\pi}\Sigma_k \mathrm{Im}\, G_k(\omega)$,

$$N(\omega)\sim\frac{1}{\pi}\sum_j^{\mathrm{nodes}}\frac{Z_{k_{nod}}^j}{v_{nod_j}v_{ano_j}}\omega, \quad (32)$$

i.e., $N(\omega)$ is linear in frequency close to the Fermi energy and the slope is uniquely determined by the quasiparticle nodal velocity v_{nod}, by the nodal derivative of the superconducting gap v_{ano}, and by the nodal quasiparticle residuum $Z_{k_{nod}}$. In other words, the low-energy density of states in the d-wave superconductor is a direct measure of the spectra at the nodes. This result explains the low-energy spectrum of the cluster density of states (black continuous line in Fig. 8), which is roughly linear for $\omega\rightarrow 0$, in the limit of the energy resolution given by ED impurity solver.

The fact that here the Σ periodization better portrays the cluster result is consistent with the hypothesis of Fermi-liquid behavior at the nodal points of momentum space, well described by the self-energy. The results of the normal component of the system suggest instead that in other regions of momentum space (at least close to the Mott transition point), a pseudogap opens in the spectrum and quasiparticles die in the antinodes. In the latter regions a cumulant $\mathcal{M}$ periodization is more appropriate than the Σ periodization.

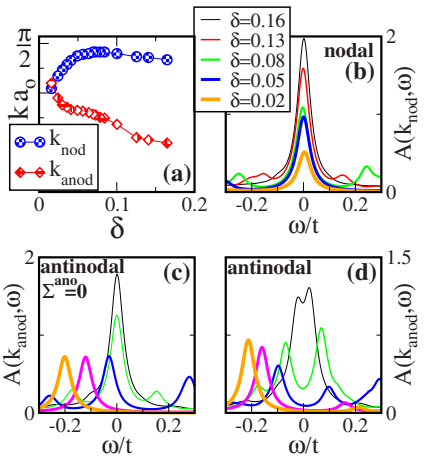

FIG. 9. (Color online) Panel (a): nodal k_{nod} and antinodal k_{anod} x-axis components of the positions of the quasiparticle peaks, in the first quadrant of the Brillouin zone, as a function of doping δ. Panel (b): Nodal peaks are found always at the Fermi level and decrease with doping δ in approaching the insulator. Panel (c): at high doping ($\delta > \delta_c \sim 0.08$) antinodal peaks are also found at the Fermi level in the normal component of the system [set $\Sigma_{ano}=0$ in Eq. (19)]. For ($\delta < \delta_p \sim 0.06$) however they shifts to negative energy opening a pseudogap. Panel (d): the actual antinodal spectra [$\Sigma_{ano} \neq 0$ in Eq. (19)] show to become asymmetric for $\delta < \delta_c$ when the pseudogap starts opening in the normal component [see panel (c) and bottom right panel of Fig. 6].

IV. PROPERTIES OF THE NODAL AND ANTINODAL POINTS

In this section we follow the observations presented above on the nodal/antinodal dichotomy and study the physical properties of the system in the nodal and antinodal points, completing in detail the work presented in Ref. 55. In order to be able to make contact with the experiments, we need to extract the fully momentum dependent Green's function $\hat{G}_k(\omega)$ [see Eq. (19)], which can be generally related to the response functions. We employ therefore a periodizing procedure to extract the k-dependent normal and anomalous components $\Sigma_k(\omega)$ and $\Sigma_{ano}(k,\omega)$ of the k-dependent self-energy. As discussed above, it is reasonable to start by assuming a d-wave shape of the superconducting gap, which is naturally obtained in our scheme by periodizing the anomalous component of the cluster self-energy via Eq. (24). At the nodes, we periodize also the normal component of the self-energy via Eq. (21). This guarantees in particular Fermi liquid properties in the nodal region of momentum space. At the antinodes instead the insulating properties of the normal component of the system (like the formations of a pseudogap at low energy and of the Mott gap at higher energies; see Fig. 8) are better portrayed by periodizing the cumulant $\mathcal{M}^{nor}$, according to Eq. (28).

A. Nodal and antinodal spectra

By adopting this procedure we can first obtain quasiparticle spectra in the *nodal and antinodal points of momentum space*, as it is shown in Fig. 9. In order to define the **k** vectors in the nodes and in the antinodes, we follow an operative definition, similar to the one used in the ARPES experiments in Ref. 71. The nodal point $\mathbf{k}_{nod}$ (antinodal point $\mathbf{k}_{anod}$) is chosen as the one having the sharpest quasiparticle peak in moving on the path $(0,0) \rightarrow (\pi,\pi)$ [$(0,\pi) \rightarrow (\pi,\pi)$] of momentum space. The x-axis components of the vectors $\mathbf{k}_{nod}=(k_{nod},k_{nod})$ and $\mathbf{k}_{anod}=(k_{anod},0)$ are shown in panel (a) of Fig. 9 as a function of doping δ. We notice that k_{anod} is a monotonic decreasing function of the δ. This is intuitively expected in a standard Fermi liquid, where the approach to the Mott transition at $\delta=0$ is accompanied by an increase in the volume enclosed by the Fermi surface in momentum space, which is proportional to the density $n=1-\delta$ of the system (Luttinger theorem[83]). The k_{nod} vector component on the contrary displays a nonmonotonic behavior, showing to decrease by reducing doping in correspondence of the special doping $\delta_c \sim 0.08$, which appears in our study as a critical point marking a change in the physical properties of the system. In the following section we will show that we can relate this behavior of the nodal and antinodal **k** points to a topology change in the Fermi surface.

In the remaining panels of Fig. 9, we show the spectral function $\mathrm{Im}[\hat{G}_k(\omega)]_{11}$ [from Eq. (19)]. As previously explained (see also Appendix B), within the ED-CDMFT method it is possible to display Green's functions on the real frequency axis ω by expressing them in a pole expansion, displayed by adding in the denominator a small imaginary part $i\eta$ (here we adopted $\eta=0.03t$). At the nodal point [panel (b)] the d-wave superconducting gap is zero, and a Fermi liquid quasiparticle peak is always found at the Fermi level ($\omega=0$) for different doping δ. The approach to the Mott insulator ($\delta \rightarrow 0$) is marked by a progressive reduction in the quasiparticle peaks. This behavior is reminiscent of the Mott transition described in the standard infinite dimensional Hubbard model. At the antinodal point the superconducting gap is maximal, a gap in the spectra is therefore expected. Before looking at the full antinodal spectrum, however, it is instructive to look at the contribution coming from the normal component, which can provide information on the physical properties of the liquid underlying the superconducting state. The normal-component spectra can be simply obtained in our scheme by zeroing the anomalous component of the self-energy $\Sigma_{ano}(k,\omega)$ in Eq. (19). These spectra are displayed in panel (c) of Fig. 9. At doping $\delta > \delta_c$, a Fermi liquid quasiparticle peak is also found at the Fermi level ($\omega=0$). In this region of the phase diagram, the normal properties of the system are therefore Fermi-liquid-like (and also k_{nod} and k_{anod} are monotonically decreasing with δ, as described above). In correspondence of the critical doping δ_c, however, a pseudogap opens and a quasiparticle peak is found at the gap edge at negative energy ($\omega<0$). The pseudogap increases in approaching the Mott transition ($\delta \rightarrow 0$), while, differently from the nodal point, the peaks show a roughly constant height. This behavior at the antinodes of the normal component of this superconducting solution can be smoothly connected to results previously obtained in CDMFT studies of the normal state.[46,59] For $\delta < \delta_c$, therefore, the normal component of the system is not a Fermi liquid in the strict sense, at least in the region of momentum space close to the

antinodal points [but a behavior unusual for a Fermi liquid is also detected by the decreasing value of k_{nod} in panel (a)]. This behavior appears also in the total antinodal spectra [upon restoring the superconducting gap $\Sigma_{ano} \neq 0$ in Eq. (19)], which we show in panel (d). At doping $\delta > \delta_c$, the quasiparticle peaks present in the normal component are parted into two bands by the opening of a superconducting gap, resulting in the typical BCS symmetric spectra. For $\delta < \delta_c$, however, the pseudogaps already present in the normal component superimpose to the superconducting gap, resulting in asymmetric spectra. This antinodal spectra nicely explains Fig. 6, where the local density of states $N(\omega)$, directly obtained from the cluster-impurity solution, is displayed. The appearance of the asymmetry for $\delta < \delta_c$ is therefore interpreted by our k-momentum analysis as the appearance of the pseudogap phase, which marks a departure from a Fermi liquid based BCS superconductor, once again at the critical doping δ_c. These observations must be directly linked to experimental spectra, either in the antinodes of momentum space, obtained for example with angle resolved photoemission,[19,20] and locally in real space, with, for example, scanning tunneling spectroscopy.[69]

B. Nodal and antinodal quasiparticle residua

In order to characterize the Mott transition, it is useful to extract the quasiparticle residuum, which is defined as

$$Z_k = \left(1 - \frac{\partial \,\mathrm{Re}\,\Sigma^{nor}(k,\omega)}{\partial \omega}\right)^{-1}_{\omega \to 0, k = k_F} \tag{33}$$

with $k_F = k_{nod}$ or k_{anod} in our case. This quantity corresponds to the area of the quasiparticle peaks [e.g., panel (b) of Fig. 9]; it is 1 in the noninteracting case and less than 1 in an interacting Fermi liquid. In the standard description of the Mott transition (i.e., the infinite dimensional Hubbard model) $Z \to 0$ linearly as $\delta \to 0$ (see Ref. 6). It is interesting therefore to observe how this quantity behaves in the nodal and antinodal k-points by varying doping δ, as we show in Fig. 10. We can give in this way a momentum space interpretation of the corresponding cluster Z_X that we have discussed in Fig. 4. As we have already mentioned, at the nodes well-defined quasiparticle peaks are observed at the Fermi level for every doping δ. The residuum Z_{nod} is therefore well defined according to the expression given above (which is strictly valid at $\omega = 0$), as in a typical Fermi liquid. This is confirmed by the good numerical agreement between the blue circles (calculated by integrating the area of the peaks, which are displayed by introducing the artificial broadening parameter $\eta = 0.03t$) and the green crosses [calculated more precisely within our method by using Eq. (33) on the Matsubara axis]. For comparison's sake, we present also the nodal quasiparticle residuum extracted in a CDMFT study implemented with a different impurity solver, the CTQMC,[52] in the two-dimensional Hubbard model with Hamiltonian parameters $U = 12t$ and $t' = 0t$. The comparison is only qualitative and it is aimed to get insight into the physical trends. We indeed observe a monotonically decreasing Z_{nod} as a function of the doping δ, similarly to the standard infinite dimensional Hubbard model. We cannot however state within our numerical resolution if $Z_{nod} \to 0$ exactly at the Mott point $\delta = 0$ (as it seems also to suggest the CTQMC result) or rather it extrapolates to a finite but very small ($Z_{nod} < 0.02t$) value. In the antinodal point more attention has to be paid in defining a quasiparticle residuum Z_{anod}. As stressed above, for $\delta > \delta_c \sim 0.08$ quasiparticle peaks are present at the Fermi level [panel (c) of Fig. 9], and Z_{anod} can be well defined by Eq. (33). For $\delta < \delta_c \sim 0.08$ however a pseudogap opens. Even if a peak can be identified at the gap edge, it is not strictly speaking a Landau-Fermi liquid quasiparticle, as the imaginary part of the self-energy is nonzero (even if small); i.e., the quasiparticle has a finite lifetime. Formula (33) cannot be directly employed. However we can still calculate the area of the peak and display its behavior as a function of the doping δ. We find in our result that for $\delta < \delta_c$, once the pseudogap opens and the peaks move to negative frequency, the weight Z_{anod} stays constant up to the Mott transition point. The behavior of Z_{nod} and Z_{anod} here presented has to be connected with the effective cluster correspondents Z_X (Fig. 4). According to Eq. (23), these are interpreted in momentum space as the quasiparticle residua in the corner points of the first quadrant of the Brillouin zone (therefore far from the Fermi surface), while Z_{nod} and Z_{anod}, which are calculated on the Fermi surface, have a real physical meaning. In spite of this, however, the cluster Z's already embody the physical properties (a Z going to zero and another nondecreasing for $\delta \to 0$), characteristic of the Mott transition in this two-dimensional system.

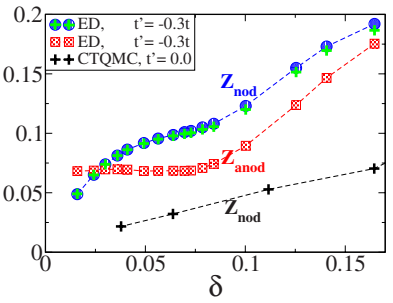

FIG. 10. (Color online) Quasiparticle residuum at the nodal point Z_{nod} and antinodal points Z_{anod} as a function of the doping δ, evaluated as area of the quasiparticle peaks shown in Fig. 9 (as a cross-check, Z_{nod} is also evaluated as the slope of the imaginary part of the self-energy on the Matsubara axis, green crosses). While Z_{nod} monotonically decreases with doping, as in the standard picture of the Mott transition, the antinodal Z_{anod} shows to stay constant upon opening of the pseudogap ($\delta < \delta_c \sim 0.08$). For comparison's sake, we display the nodal Z_{nod} obtained by CTQMC (Ref. 52) on the two-dimensional Hubbard model with similar parameters ($U = 12t$, $t' = 0.0$, $\beta = 200$). These quasiparticle residua should be compared with their cluster counterparts in Fig. 4.

We stress that the description of the Mott transition we find in this study of the two-dimensional Hubbard model is very different from the standard Mott transition picture in infinite dimension.[6] In our system different regions of momentum space behave very differently in approaching the transition point. In this way we can go from a Fermi-liquid-based superconductor (realized for $\delta > \delta_c$) into the Mott insulator (at $\delta = 0$) by passing through a phase $0 < \delta < \delta_p$, where the system is at the same time insulating in the antin-

odal region and Fermi liquid in the nodal region of momentum space. This latter appears to approach the Mott point in a more standard (infinite dimensional Hubbard model) way, with a quasiparticle residuum $Z_{nod} \to 0$ (at least within our numerical precision). In the antinodal region instead the quasiparticle peak (which underlies the superconducting gap) stops reducing at $\delta = \delta_c$ and shifts to negative energies opening a pseudogap. This behavior is reminiscent of the *orbital selective Mott transition*, found, e.g., in two band Hubbard-type models,[84–86] where the spectral weight is not transferred from the low energy ($\omega = 0$) to the Hubbard bands (located at a energy scale of order $\sim U$), as in the standard Mott transition, but rather onto a smaller energy scale of the order of an exchange coupling $J \sim 1/U^2$, inside the Mott gap. In spite our model is a one band one, different regions of momentum space appear to behave as different bands. By decreasing doping δ, a first orbital selective Mott transition takes place at δ_c in the antinodal regions, and a full Mott transition takes finally place at $\delta = 0$.

C. Nodal and antinodal quasiparticle velocities

Useful information on the nodal point can be extract by performing a low-energy expansion of Green's function [see Eqs. (29) and (31)], taking advantage of the Fermi liquid properties of the nodal point. In particular the nodal velocity has two components, one coming from the normal part $v_{nod} = |\nabla_k \tilde{\xi}_k|$, perpendicular to the Fermi surface, and the other related to the superconducting gap $v_{nod} = Z_{nod} |\nabla_k \Sigma_{ano}(k)|$, parallel to the Fermi surface. v_{nod} can be experimentally extracted, e.g., from the ARPES quasiparticle dispersion at the node,[87] while v_{ano} can be determined, e.g., as the slope of the superconducting gap at the node.[71] In Fig. 11 v_{nod} and v_{ano} are displayed as a function of doping δ. For comparison's sake, in the top panel we show experimental nodal velocity extracted from different materials (the figure has been taken from the supplementary material in Ref. 87). In the bottom panel we show our result and also insert for a qualitative comparison the CTQMC-CDMFT result in Ref. 52. v_{nod} shows to be greater than v_{ano}, in agreement with experimental observation (see, e.g., Ref. 19). In ED-CDMFT it slightly oscillates around a constant value from the overdoped to the underdoped ($\delta < \delta_c$) side of the phase diagram, while in the CTQMC case it is slightly decreasing with decreasing doping. This behavior is in good qualitative agreement with experimental results reported in the top panel (a quantitative comparison would roughly held for a lattice spacing $a_0 \sim 4$ Å and a $t \sim 0.5$ eV, $v_{nod} \sim 1$ eV Å, which is of the order of magnitude of experiments). Remarkably, either with ED and with CTQMC, v_{ano} displays a domelike shape, with a maximum around optimal doping $\delta_p < \delta < \delta_c$ (note that in the ED case $t' = -0.3t$, $\delta_c \sim 0.08$ while in the CTQMC case $t' = 0$, $\delta_c \sim 0.12$). This is an important result: as shown in formula (30) and discussed in Ref. 55, the anomalous velocity $v_{ano} = \sqrt{2} Z_{nod} \Sigma_{ano}(\omega = 0) \sin k_{nod}$ can be interpreted as a direct measure of the superconducting gap in the nodal region, which reveals to be nonmonotonic with doping, in agreement with some recent experimental spectroscopy results.[70,71] The agreement in the trend of v_{ano} between the ED and CTQMC

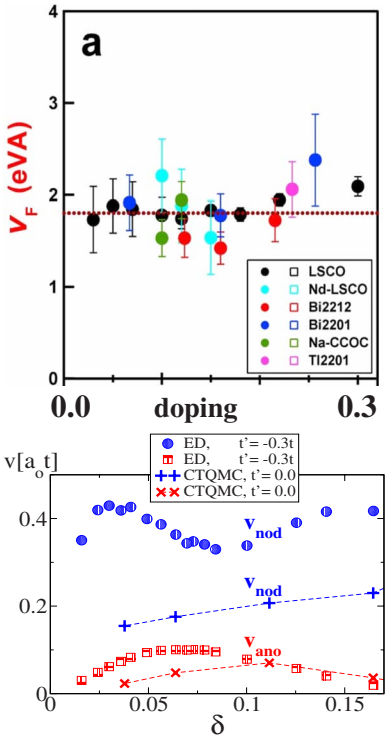

FIG. 11. (Color online) Top: Nodal velocity as a function of doping measured from the quasiparticle dispersion of different materials (figure taken from Ref. 87). To be confronted with the nodal component of the velocity v_{nod} calculated in our work and displayed in the bottom. Bottom: Nodal anomalous velocity $v_{ano} = \sqrt{2} Z_{nod} \Sigma_{ano}(k_{\rm nod})$ (tangent component of the nodal velocity) and nodal quasiparticle velocity $v_{nod} = Z_{nod} |\nabla_k \xi_{k_{nod}}|$ (component of the nodal velocity perpendicular to the Fermi surface) as a function of doping δ (units are $a_0 t$, where a_0 is the square lattice spacing). The trends are compared with CTQMC-CDMFT (Ref. 52) calculations on the two-dimensional Hubbard model with similar parameters ($U = 12t$, $t' = 0.0$, $\beta = 200$).

shows that this result is solid from the theoretical side too. We will come back to discuss the nodal and antinodal gaps more in detail at the end of this section.

D. Low-energy nodal density of states and Raman response

At the nodal point, the combination of the quasiparticle residuum Z_{nod} and nodal velocities can give further information, which can be confronted with experimental observable quantities and which can further support the physical description drawn from our CDMFT result. Based on the Fermi liquid assumption at the nodes, in Eq. (32) we have, for example, extracted the low energy ($\omega \to 0$) behavior of the local density of states $N(\omega) \sim \frac{Z_{nod}}{v_{nod} v_{ano}} \omega$. The slope $\frac{Z_{nod}}{v_{nod} v_{ano}}$ is displayed as a function of doping δ in Fig. 12, comparing the ED-CDMFT results of this work (with $t' = -0.3t$) with the CTQMC-CDMFT results in Ref. 52 (with $t' = 0$). Once again it is the trend we want to compare rather than the quantitative values. Starting from the overdoped side, the slope of $N(\omega)$ is decreasing monotonically by decreasing doping, until showing a slight up turn close to the Mott transition (observ-

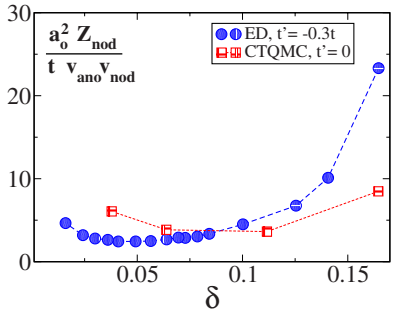

FIG. 12. (Color online) The slope of the low-energy local density of states $N(\omega) \sim \frac{Z_{nod}}{v_\Delta v_{nod}} \omega$ is displayed as a function of doping δ. Trends are compared with CTQMC-CDMFT (Ref. 52) calculations on the two-dimensional Hubbard model with similar parameters ($U=12t$, $t'=0.0$, $\beta=200$).

able both in the ED and CTQMC cases). While the linearity of $N(\omega)$ is well established in scanning tunneling experiments,[69] the behavior of the slope as a function of doping is at the moment very difficult to extract (as it is not possible to obtain absolute values for different doping). Our result (in particular the up-turn tendency at small doping) has to be therefore considered a theoretical prediction.

A further ratio of experimental relevance can be connected at first order to the low-energy ($\omega \to 0$) linear behavior of the B_{2g} Raman response function $\chi_{B_{2g}} \sim \frac{Z_{nod}^2}{v_{nod} v_{ano}} \omega$ (see Ref. 70) and the low-temperature ($T \to 0$) behavior of the superfluid stiffness $\rho_s(T) - \rho_s(0) \sim \frac{Z_{nod}^2}{v_{nod} v_{ano}} \omega$, which can be extracted from measures of the penetration depth.[88,89] Our results (together with the CTQMC-CDMFT results in Ref. 52) are shown in the bottom panel of Fig. 13 and compared with the aforementioned Raman and penetration depth data presented in the top panel (the figure has been taken from Ref. 70). The remarkable feature, found in experiments and supported in our calculation, is the constant value displayed by this ratio in the underdoped region ($\delta < \delta_c$). While in the experimental results a sum rule is assumed, in order to being able to compare measures from different doping/samples, our theoretical results are derived from a bare strongly correlated electron model, where other kinds of assumptions and approximations (as explained in the previous sections) are implied. The convergence of experimental and theoretical results therefore strongly supports these findings, presenting them as distinctive feature of the cuprate superconductor nodal dispersion.

E. Nodal and antinodal gaps in spectroscopy

The behavior of the spectra presented in Fig. 9 can be directly connected to spectroscopy experiments. In particular, a lively debate has recently risen on the momentum resolved structure of the superconducting gap.[72–75,90–93] We proceed as in ARPES experiments (see, e.g., Ref. 71) and extract the quasiparticle gap in the nodal and antinodal points of momentum space, taking advantage of the periodizing scheme we have introduced. To this purpose, it is convenient to use the low energy ($\omega \to 0$) expansion carried out in Eq.

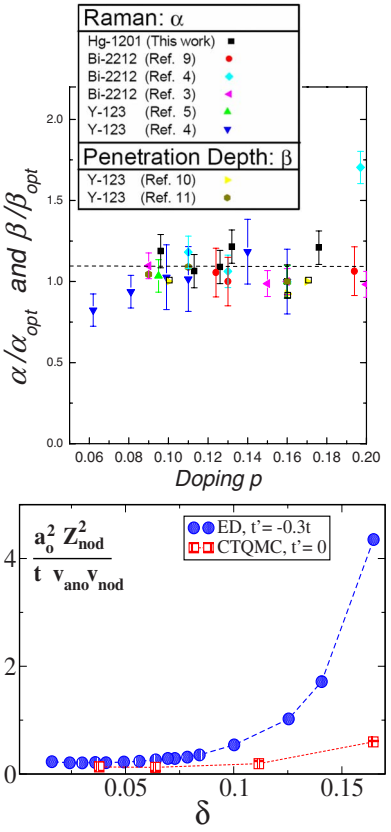

FIG. 13. (Color online) Top: the linear coefficient of the low energy Raman response $\chi_{B_{2g}}(\omega) \sim \alpha\omega$ and the low temperature superfluid stiffness (from penetration depth) $\rho_s(T) - \rho_s(0) \sim \beta T$, extracted from various experiments (figure taken from Ref. 70). Quantities are normalized at the optimal doping value. Bottom: the linear coefficient of the Raman response and superfluid stiffness as extracted from our calculation $Z_{nod}^2/(v_\Delta v_{nod})$ and displayed as a function of doping δ. Trends are compared with CTQMC-CDMFT (Ref. 52) calculations on the two-dimensional Hubbard model with similar parameters ($U=12t$, $t'=0.0$, $\beta=200$).

(29). In particular we have seen that quasiparticle peaks are always found in our result, even if not in a strict sense (in the pseudogap region $\delta < \delta_c$ quasiparticle peaks are located at the gap edge and have finite lifetime), and therefore we expect the expansion to be reasonably good at small frequency (i.e., $\omega \leqslant$ the superconducting gap). We can, in this case, write the total gap $\Delta_{tot}(k,\omega)$ as the quadratic sum of two contributions [see Eq. (30)],

$$\Delta_{tot}^2(k,\omega) = \Delta_{nor}^2(k,\omega) + \Delta_{sc}^2(k,\omega), \tag{34}$$

where $\Delta_{sc}(k,\omega) = Z_k \Sigma_{ano}(k,\omega)$ is the usual d-wave superconducting gap [note that it is directly connected, except for constant factors, to the anomalous component of the nodal velocity $v_{ano} \sim Z_{k_{nod}} \Sigma_{ano}(\omega=0)$ discussed in Fig. 11] and $\Delta_{nor}(k,\omega) = \tilde{\xi}_k(\omega) = Z_k [\xi_k + \mathrm{Re}\, \Sigma_k(\omega)]$ is a normal contribution to the gap which can arise only if, for some k and $\omega \to 0$, the normal component of the self-energy $\Sigma_k(\omega)$ grows enough so that the band equation $\tilde{\xi}_k = 0$ cannot be satisfied (i.e., there is not Fermi surface). Now, this does not take place at the nodes, where quasiparticles are found for all

dopings [panel (b) of Fig. 9], $\tilde{\xi}_k=0$; the system presents standard Fermi liquid properties, and the total spectral gap coincides with the superconducting gap $\Delta_{tot} \equiv \Delta_{sc}$. (This already suggests that looking for the "real" superconducting gap of the system one should look at the nodal region gap. Recent theoretical[52] and experimental Raman spectroscopy studies[94] point at this direction.) In the antinodal region, instead, we have observed that a pseudogap opens in the normal component for $\delta < \delta_c \sim 0.08$ [panel (c) of Fig. 9], and this fact is associated in our calculation with the appearance of lines in k space close to the antinodal region where the self-energy is diverging (see Refs. 46 and 59). It is not possible therefore to satisfy the equation $\tilde{\xi}_k=0$, and a Fermi surface does not exists anymore. The normal contribution Δ_{nor} kicks in and determines the properties of the total antinodal gap Δ_{tot}, originating the asymmetric spectra we already described in panel (d) of Fig. 9.

We can extract, like in ARPES experiments (e.g., Ref. 71), the antinodal gap Δ_{tot} from the spectra of panel (d) of Fig. 9 by measuring the distance of the quasiparticle peaks at the gap edge from the Fermi level $\omega=0$. In the same way, from panel (c) of Fig. 9, we can measure the normal contribution Δ_{nor}. We display Δ_{tot} and Δ_{nor} as a function of doping δ in the bottom panel of Fig. 14, comparing directly with experimental results, shown in the top panel (for convenience's sake we extract the picture from the Raman results in Ref. 70 but ARPES points are also displayed). The antinodal gap Δ_{tot} is a monotonic decreasing function of doping (curve labeled "antinodal B_{1g}" in the top panel of Fig. 14), as it has been known from experiments since a long time (see, e.g., Refs. 19 and 20) and predicted in the most popular theories of high-temperature superconductivity (e.g., resonating valence bond theory;[1] for a recent general review see, e.g., Ref. 57). In our calculation we show that at small doping an important contribution comes indeed from the normal component Δ_{nor}, which appears at δ_c and it is also monotonic. From the experimental side, the novelty comes from precise measures of the nodal gap, recently obtained by Raman spectroscopy[70] and ARPES,[71] which show surprisingly that in this region of momentum space the spectral gap is nonmonotonic with doping δ, tracking instead the behavior of the critical temperature T_C (curve labeled "nodal B_{2g}" in the top panel of Fig. 14). In our calculation the nodal gap corresponds to the anomalous component of the nodal velocity v_{ano}, which we have discussed in Fig. 11 and which shows indeed a behavior strongly similar to these experimental results. We clarify now how it is possible that the nodal component of the gap tracks T_C as a function of doping δ, while at the same time the antinodal component is monotonic, by disentangling the superconducting contribution $\Delta_{sc}=\sqrt{\Delta_{tot}^2-\Delta_{nor}^2}$, which we also display in the bottom panel of Fig. 14 (green diamonds). To check the validity of our formula (34) and making connection with $v_{ano} \sim Z_{k_{nod}} \Sigma_{ano}$, which has been evaluated at the nodal point, we also evaluate and display $\Delta_{sc}=Z_{anod}\Sigma_{ano}(k_{anod}, \omega=\Delta_{nor})$, finding numerical agreement (blue triangles). This shows indeed that the total antinodal gap Δ_{tot} has indeed two distinct contributions, displaying opposite trends with dopings. In the underdoped side Δ_{nor} dominates in the antinodes and creates a monotonically increasing total gap. In the nodes, instead, Δ_{nor} is zero and only the superconducting gap is detectable. In our results we connect therefore the experimentally observed two-gap phenomenon with the opening of the pseudogap at the antinodes at a finite critical doping δ_c. According to our point of view, this is an effect arising in a strongly correlated electron system that approaches the doping-driven Mott transition in a two-dimensional lattice. The fact that Δ_{sc} tracks T_C (Ref. 94) is remarkably similar to the standard BCS superconductivity. These results put strong constrains on the theories of cuprate-based superconductivity, which have to consider the presence of these two distinct components in the spectral gap and its interplay with the domelike shape of the order parameter, the rise of the pseudogap phase, and the approach to the Mott insulator. Our cluster results, interpreted via a periodization procedure, well fit the experimental observations and give a simple interpretation in terms of a combination of all these effects.

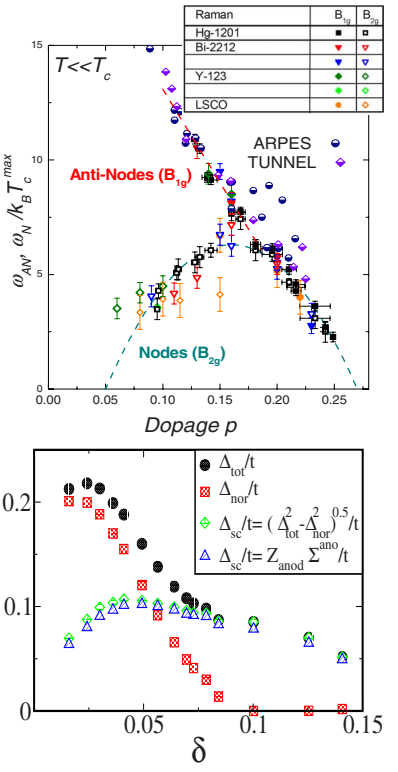

FIG. 14. (Color online) Top: Nodal (B_{1g}) and antinodal (B_{2g}) quasiparticle gaps extracted by different spectroscopy experiments as a function of doping (the figure is extracted from the Raman spectroscopy results in Ref. 70). Bottom: the antinodal gap Δ_{tot} and the nodal Δ_{sc} extracted from the spectra of Fig. 9 as a function of doping δ. Δ_{sc} can be directly related to the tangential component of the nodal velocity v_{ano} presented in Fig. 11 (here displayed by the blue triangles). Δ_{nor} is the pseudogap in the normal component extracted in panel (c) of Fig. 9.

V. MIXED-PERIODIZATION SCHEME

The discussion presented in the previous sections is valid close to the nodal and antinodal points of momentum space,

where we have shown that periodizing the self-energy or the cumulant is a reasonable approximation. Obtaining information in intermediate region of momentum space, between the nodal and antinodal ones, is beyond the limits of a pure 2×2 plaquette study. In this region, in fact, the Fermi liquid physical properties of the nodal points have to interlace in some nontrivial way with the insulatinglike properties of the antinodal point. A detailed description of this phenomenon can be taken into account by studying bigger cluster [i.e., obtaining a better truncation of the Fourier expansion in Eq. (20)] at present not possible with ED-CDMFT. Nevertheless we want to keep in this section a low profile and introduce a first-order description of the spectral properties in all momentum space, which could be compared to experimental results (such as, e.g., ARPES). We want therefore to introduce a periodizing scheme able to describe

(1) a Fermi liquid quasiparticle in correspondence of the nodal point,

(2) the opening of a pseudogap in the antinodal points in the underdoped regime, and

(3) the formation of the Mott gap at high energies in approaching the Mott insulator (see top panel of Fig. 8, region marked A).

We can satisfy the first condition by using the self-energy Σ periodization. The second and third points are instead obtained by using the cumulant $\mathcal{M}$ periodization, which is able to describe the formation of the antinodal gap.

In order to combine all these requests, we take advantage from ideas introduced in phenomenological Fermi-liquid Boltzmann approaches to the normal-state transport properties of cuprate superconducting materials.[60,78–80] We base in particular on the work in Ref. 60, where the division of momentum space in nodal Fermi-liquid-like regions, *cold spots*, and antinodal insulatorlike regions, *hot spots*, is achieved by projecting the quasiparticle scattering operator $C_{kk'}$ on a basis of patches $\{\phi_\alpha\}$ in momentum space with different temperature scattering dependencies,

$$C_{kk'} = \sum_{\alpha\beta} \phi_\alpha(k) C_{\alpha\beta}(T) \phi_\beta(k). \tag{35}$$

Within this approach, it is possible to solve exactly the Boltzmann equation for the simple case of two patches (one marking the nodal and the other the antinodal region). The shape and the scattering properties of the cold patch (modeled by a small set of parameters) were fixed in Ref. 60 by obtaining the best fit on few transport quantities (resistivity, Hall coefficient), and a systematic correspondence with other transport quantities (magnetoresistance and thermoelectric power) was then obtained. For comparison, the nodal patch Φ_k used in Ref. 60 is shown on the left-hand side of Fig. 15 (the antinodal patch is simply defined as $1-\Phi_k$).

In the same spirit, we employ here a mixed periodization scheme, by projecting the lattice self-energy $\Sigma_k(\omega)$ on a nodal $\Phi(k,\omega)$ and an antinodal $1-\Phi(k,\omega)$ patch in momentum space,

$$\Sigma_k(\omega) = \Phi(k,\omega)\Sigma_k(\omega)[\hat{\Sigma}] + [1-\Phi(k,\omega)]\Sigma_k(\omega)[\hat{\mathcal{M}}], \tag{36}$$

where $\Sigma_k(\omega)[\hat{\Sigma}]$ is obtained by periodization of the cluster Σ and $\Sigma_k(\omega)[\hat{\mathcal{M}}]$ by periodization of the cluster cumulant $\mathcal{M}$

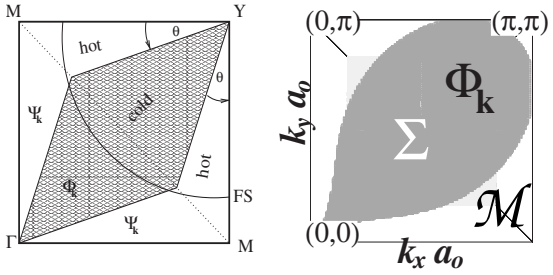

FIG. 15. Left: the shaded region is the patch Φ_k used in the phenomenological Boltzmann approach in Ref. 60 in the first quadrant of the Brillouin zone. Right: the patch Φ_k used in this work [see formula (37)].

[Eq. (26)]. The patch $\Phi(k,\omega)$ separates the Σ periodized from the $\mathcal{M}$-periodized regions (right-hand side of Fig. 15). For convenience's sake, we choose a form with k and ω separable,

$$\Phi(k,\omega) = \Psi(k)\Psi(\omega),$$

$$\Psi(\alpha) = \frac{1}{2}[1-\tanh(\beta_\alpha r_\alpha)], \tag{37}$$

where r_α is the distance from the a center in k or ω space,

$$r_k = \sqrt{(k_x-k_{x_c})^2+(k_y-k_{y_c})^2} - r_0(\theta),$$

$$r_\omega = |\omega| - \omega_0. \tag{38}$$

Here $(k_{x_c},k_{y_c}) \sim (\frac{\pi}{2},\frac{\pi}{2})$, $r_0(\theta) = r_0 e^{-(\theta-\pi/4)/\sigma_0^2}$, and $\theta = \arctan(k_y/k_x)$ can be chosen to properly shape the patch. We fix through all the rest of the paper $\omega_0 \sim 0.5t$, $\beta_k \sim 100$, and $\beta_\omega \sim 15$, which smooth the boundaries of the patch. It remains to fix the parameters $\mathbf{k}_c$, r_0, and σ_0, which have to be chosen to mimic the phenomenological patch of Fig. 15. There is of course a good degree of arbitrariness in the patch form. We want however to have a first-order qualitative description of the physical properties in momentum space, with the aim to address consideration that is only slightly dependent on the exact form of the patch.

A. Evolution of the Fermi surface

In order to fix the dimension of the patch $\Psi(k)$ in k space it is useful to follow the evolution of the Fermi surface in approaching the Mott insulator with the two periodization schemes Σ and $\mathcal{M}$, as shown in the panels of Fig. 16. At high doping (in our case $\delta=0.13$) all the system is well described by a Fermi liquid, the self-energy is mostly local, and the Σ (green dashed line) and $\mathcal{M}$ (blue continuous line) periodizations give in practice the same result. We can choose to describe the system with the Σ periodization and $\Psi(k)$ covering all the k space (for example, see the left panel of Fig. 17 for $\delta=0.13$, where the patch is marked by the gray region covering all of the quadrant). By reducing doping, however, the off-diagonal components of the cluster self-energy $\hat{\Sigma}_c$ are not negligible anymore, and the two periodizations produce different results. In particular, as we stressed in

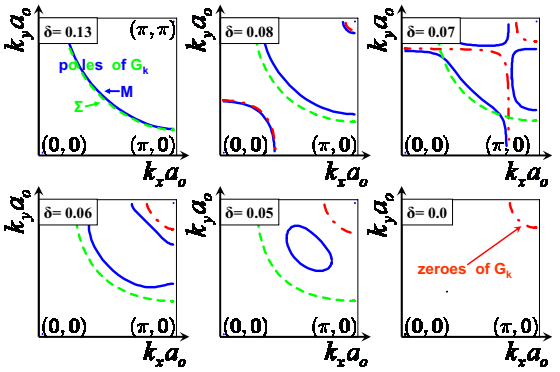

FIG. 16. (Color online) We show that the evolution of the normal-component Fermi surface (blue continuous line in the $\mathcal{M}$-periodization scheme; green dashed line in the Σ-periodization scheme) defined has $\xi_k + \mathrm{Re}\,\Sigma_k = 0$ in Eq. (19). Panels span from the overdoped region ($\delta = 0.13$ top-left panel) to the Mott insulator ($\delta = 0.0$ bottom-right panel). By periodizing the cumulant $\mathcal{M}$, the Fermi surface disappears in the insulating state and it is replaced by a line of zeroes of G_k (red dot-dashed lines). The way this takes place is via a topological phase transition around $\delta_p \sim 0.06 < \delta < \delta_c \sim 0.08$ from a large holelike Fermi surface to a pocketlike Fermi surface. The low doping region is marked by a phase where Fermi surface and lines of zeroes coexist. This gives origin to the pseudogap and the fragmentation of the Fermi arcs in measures of spectra of the normal state system (see, e.g., Fig. 18). By periodizing the self-energy Σ, by construction, the lines of zeroes cannot appear. The pseudogap is realized only through a modulation of the spectral intensity along the Fermi surface line, which extends always on all the Brillouin zone (see also Fig. 18).

the previous sections, doping $\delta_c \sim 0.08$ and $\delta_p \sim 0.06$ are special points. In the $\mathcal{M}$ periodization the Fermi surface shows a striking topological phase transition, produced by the appearance of lines of zeroes of Green's function $G_k(\omega \to 0)$ (marked by a red dot-dashed line in Fig. 16). The effect of the appearance of the lines of zeroes of Green's function is at the origin of the opening of a pseudogap in the spectral function close to the $(0,\pi)-(\pi,\pi)$ and $(\pi,0)-(\pi,\pi)$ sides of the first quadrant in the Brillouin zone [as shown, for example, in panel (c) of Fig. 9]. In the Σ periodization instead a more continuous evolution of the original high-doping Fermi surface (green dashed line) takes place at all dopings up to the Mott insulating state, where it disappears. We note however that the doping δ_c still marks a change in the curvature of the Fermi surface (even if with the Σ periodization the effect is more difficult to be noticed by naked eye), as evidenced in the downturn of the k_{nod} vector as a function of doping in panel (a) of Fig. 9. This effect was first noticed in Ref. 34 where we show that the result of periodizing Σ produces a Fermi surface which enhances its hole like curvature while reducing doping (and the antinodal spectral weight reduces too with respect to the nodal point). This behavior goes in the direction of forming a hole pocket, which however never arrives to be realized within the Σ periodization. Within the $\mathcal{M}$ scheme instead, the Fermi pocket forms at low doping and its progressive reduction in approaching the Mott transition describes the way the Fermi surface disappears. In the Mott insulating state Fermi lines have totally disappeared, but a line of zeroes of G_k [i.e., a line of divergent self-energy $\Sigma_k^{nor}(\omega=0)$] remains (red dot-dashed line) close to the corner $k=(\pi,\pi)$ of the first quadrant of the Brillouin zone.

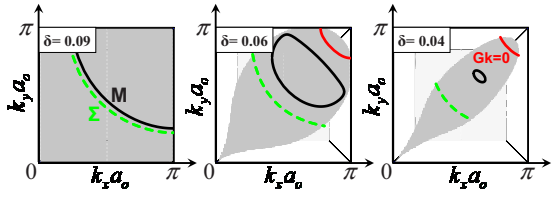

FIG. 17. (Color online) The dimension of the patch Ψ_k in momentum space (gray shaded region) is determined in such a way that the $\mathcal{M}$-Fermi surface (black continuous line) is cut away and replaced by the Σ-Fermi surface (green dashed line). On the red lines around the corner point (π,π) the self-energy Σ_k is diverging and $G_k = 0$.

It is very difficult to state how close to the real solution one or the other of the two descriptions are. Particularly intriguing is the $\mathcal{M}$-periodization result. Not only it well portrays the pseudogap in antinodes, it also produces, together with the Fermi surface, lines of zeroes of G_k. In this way it describes a continuity from the Fermi liquid at high doping (where only the Fermi surface is present) to the Mott insulating state (where only lines of zeroes are present). To this respect, it is clear that the Σ-periodization scheme fails in describing the Mott state, as it is unable by construction to build up lines of zeroes. Within our analysis, however, we cannot claim that in the real physical system a Fermi pocket, together with lines of zeroes, is actually present. Recent experiments on cuprate systems, where it has been possible to induce a low-temperature normal state by the application of an external magnetic field, have actually observed de Haas–van Alphen oscillations compatible with a Fermi pocket picture.[95] Hall resistivity measures, extracted at low temperature by suppressing superconductivity with the application of an external magnetic field,[96–98] are also compatible with the scenario of a topological phase transition of the Fermi surface. Our results are also in strong resemblance with the recent *ab initio* study on the cuprates in Ref. 99 and the theoretical phenomenological approach in Ref. 91 where similar conclusions on the evolution of the Fermi surface and the appearance of lines of zeroes have been drawn starting from an *ad hoc* model for the doping-driven Mott insulator transition in two dimensions. Other nonperturbative microscopic approaches have drawn conclusions in similar directions (see, e.g., Refs. 100 and 101). There are however some caveats in concerning the hole pocket which have to be considered.

In first place, according to the generalized Luttinger theorem[83,102–104] the volume enclosed between the Fermi surface and the line of zeroes (if present) should be equal to the particle density $n = 1 - \delta$. This theorem is quite respected (but not so much at low doping) by the Fermi surface derived with the Σ periodization (green dashed line in Fig. 16). It is not clearly obeyed instead at low doping by $\mathcal{M}$ periodization, as evident, e.g., by looking at the area enclosed between the Fermi pocket (blue line) and the lines of zeroes (red dot-dashed line) in the panel $\delta = 0.05$ of Fig. 16 (close to

half-filling the volume which gives the correct density should be half of the quadrant). Far from stating that the system is violating Luttinger theorem (which in strongly correlated system is actually a possibility[49,105]), this effect is likely an artifact coming from the truncated Fourier expansion in Eq. (20), which can be improved only by increasing the cluster size. A possible scenario is that in real systems the line of zeroes is closer to the zone diagonal which goes from $(0,\pi)\rightarrow(\pi,0)$, as actually we find at half-filling for a chemical potential value in the middle of the Mott gap $\mu\sim U/2$ (the panel displayed in Fig. 16 has a chemical potential close to the Mott gap edge $\mu\sim U/2-\Delta_M/2$, where Δ_M is the total Mott gap). This is, in fact, what was proposed in Ref. 91 as starting hypothesis. In this way, the side of the hole pocket facing the (π,π) corner point is "canceled" by the proximity of the lines of zeroes (see, for example, the spectral functions of Fig. 18), and the resulting picture is the presence of a Fermi arc in the nodal region, which is replaced by a lines of zeroes in the antinodal regions.

In second place, the discussion we have previously carried out (see Fig. 8 in Sec. III and the description of nodal properties in Sec. IV) shows that the low energy nodal point is better portrayed by periodizing Σ, i.e., at the nodal point we rather have a Fermi arc more than a pocket. This is important if the nodal point properties (presented in Secs. III and IV) have to be well portrayed. The real solution result at the nodes is likely to lay in between the $\mathcal{M}$- and Σ-periodization schemes.

B. Choice of the patch shape

In line with the discussion above, we choose therefore to assign to the nodal region the patch Ψ_k, which uses the Σ periodization. The rest of the k space (covered by $1-\Psi_k$) is described with the $\mathcal{M}$ periodization. By following this criterion we establish the evolution of $\Psi(k)$ with doping, as shown in Fig. 17. The size and shape of the patch Ψ_k are determined so that the $\mathcal{M}$ Fermi surface is cut away, and the only piece of Fermi surface inside Ψ_k is the one produced by periodizing Σ (green dashed line). By reducing doping δ the size of the patch Ψ_k progressively reduces, until possibly disappearing in the Mott insulating state ($\delta=0$) where only the $\mathcal{M}$ scheme reproduces well the gapped spectra. We have fixed the center of Ψ_k by choosing $(k_{x_c},k_{y_c})=(k_{x_{nod}},k_{y_{nod}})$, the momentum coordinate of the nodal point described in panel (a) of Fig. 9. A complete description of the patch parameters r_0 and σ_0 [see formula (37)] as a function of doping is given in the following table:

δ	>0.08	0.08	0.06	0.055	0.05	0.04	0.03
r_0	3.00	2.20	2.20	2.20	2.20	2.20	2.20
σ_0	$\pi/2$	$\pi/2.4$	$\pi/2.8$	$\pi/5$	$\pi/8$	$\pi/12$	$\pi/16$

We notice that with the choice of this patch most of the lines of zeroes disappear from the quadrant of the Fermi level. As mentioned above, we are not able to make definitive statements about the actual position of these lines of zeroes. If they were closer to the quadrant diagonal $(0,\pi)\rightarrow(\pi,0)$ (as conjecture in work in Ref. 91), they would reappear in the $1-\Psi_k$ region of momentum space, which is described by the cumulant. As stressed in the previous section, this would be important if one wants to respect the Luttinger theorem on the particle counting. In this mixed periodization used for the 2×2 plaquette result this does not take place. We remark however that in the $1-\Psi_k$ region scattering rate (i.e., self-energy) is very high (similar to the results in Ref. 101), and this fact is ultimately the reason for the appearance of a pseudogap, whether or not the line zeroes are effectively present. These physical effects are to some extent reminiscent of the results produced by the presence of a van Hove singularity in the electron spectrum, pinned at the Fermi level (see, for example, Ref. 135). The division of the k space via the patch Ψ_k is surely artificial, and it has no pretext describing in detail the real properties of the system. It is however capable of capturing in a unique scheme either the virtues of the Σ periodization (above all in the nodes) and of the $\mathcal{M}$ periodization (above all in the antinodes), which portray with some good degree of confidence the physical properties in different regions of momentum space (as we discussed in the previous sections).

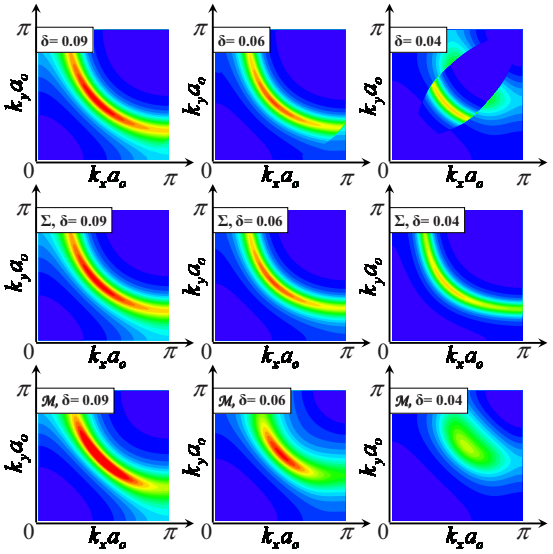

FIG. 18. (Color online) The spectral function $A(k,\omega)=-\frac{1}{\pi}\,\mathrm{Im}\,G_k(\omega\rightarrow0)$ in the first quadrant of the Brillouin zone obtained with the mixed periodization (top row) is confronted with one obtained from the self-energy (Σ) and the cumulant ($\mathcal{M}$) periodizations (second and third rows from the top). The broadening $\eta=0.052$; the color scale $x=0.5$ (see Appendix A for details).

A confrontation between the Σ, $\mathcal{M}$ and mixed periodizations is presented in Figs. 18 and 19. In Fig. 18 we show the normal-component spectral density $A(k,\omega)=\frac{1}{\pi}\,\mathrm{Im}\,G_k^{nor}(\omega\rightarrow0)$ in the first quadrant of the Brillouin zone for decreasing doping δ (from left to right). The mixed-periodization scheme (top row) is confronted with the Σ and $\mathcal{M}$ periodizations (bottom rows), showing how the patch Ψ_k is interlacing them. The well-known phenomenon of the Fermi arc breakup[19,20] is reasonably well described by all methods, showing this is a solid result of CDMFT. Moreover, the similarity with spectra calculated in previous CDMFT work on the normal state[46,59] shows the smooth continuity between

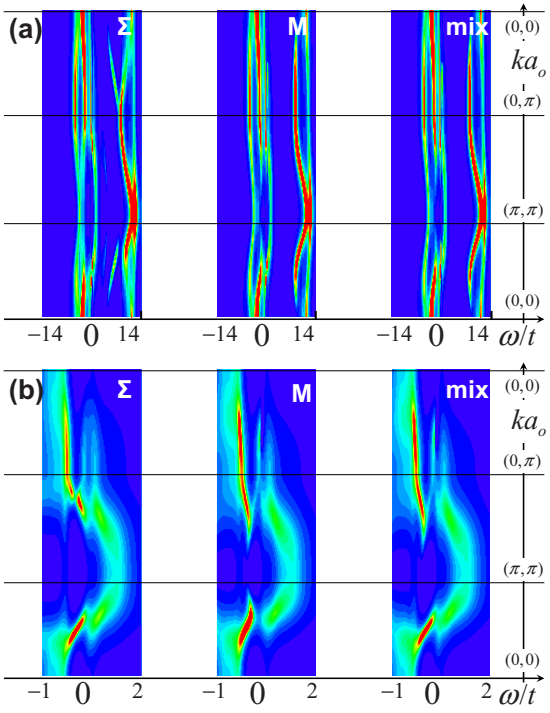

FIG. 19. (Color online) Comparison between the Σ-periodization scheme, the cumulant $\mathcal{M}$-periodization scheme, and the mixed-periodization scheme for a low doped system $\delta=0.05$. On the top row (a) we show the full energy range $-14<\omega<14$ covering the lower Hubbard and upper Hubbard bands. The gross features are very similar. Note that the Σ scheme introduces fake density of states in the Mott-Hubbard gap. In the bottom row (b) we show a closeup at low energy $-1<\omega<2$, where the methods are most different. The mixed scheme is constructed to retain a Σ-periodization character close to the nodal region $k\sim(\frac{\pi}{2},\frac{\pi}{2})$ and a $\mathcal{M}$-periodization character in the antinodal region $k\sim(0,\pi)$. Spectral functions are displayed by introducing a ω dependent broadening $i\eta(\omega)$ and the maximal color scale value is $x=0.20$ [0.25] for the top [bottom] panel (see Appendix A).

the normal component spectra of this superconducting state solution with the spectra of a normal state result. In Fig. 19 we show the band spectrum $A(k,\omega)$ plotted as a function of the energy ω along the path $(0,0)\rightarrow(\pi,\pi)\rightarrow(0,\pi)\rightarrow(0,0)$ in the first quadrant of the Brillouin zone. In the top panel (a) we confront the full energy range $-14<\omega<14$ covering upper Hubbard band and lower Hubbard band. At this energy resolution the three schemes are qualitatively very similar. We just stress that the Σ periodization artificially introduces spectral weight in the Mott gap (as discussed in Fig. 8 and evident in the figure around $\omega\sim3-7t$). This justify the choice of cutting the patch $\Psi(\omega)$ at low energies $\omega\leqslant0.5t$, using the $\mathcal{M}$ periodization in the remaining energy range. In the bottom panel (b) of Fig. 16 we show a close up at low energy $(-1<\omega<2)$. In this energy range the methods most differ; however the qualitative results are still very similar. In particular, the mixed scheme has been designed to well describe a Fermi liquid linear dispersion at the node and the right description of the Mott gap, especially in the antinodal region. In the analysis of the following sections we will therefore apply the mixed scheme introduced

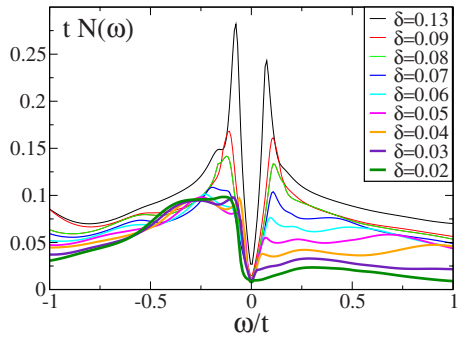

FIG. 20. (Color online) Local density of states $N(\omega)$ as a function of the doping obtained with the mixed-periodization scheme. The V shape at $\omega\rightarrow0$ is expected from a d-wave superconductor with nodal Fermi liquid quasiparticles. For doping $\delta<\delta_p\sim0.6$ spectra develop a marked asymmetry. This result interprets the cluster result of Fig. 6 and it is in good agreement with scanning tunneling experiments (see, e.g., Ref. 69). The display on the real axis of Green's function has been obtained by introducing a ω-dependent broadening $i\eta(\omega)$ (see Appendix A for details).

here through formula (36) to periodize the normal component of the self-energy [while the anomalous component $\Sigma_{ano}(\omega)$ is always obtained through formula (24), implying by construction a d-wave shape of the superconducting gap].

C. Local density of state with the mixed scheme

We use now the mixed periodization to recalculate the local density of states $N(\omega)=-\frac{1}{t\pi}\Sigma_k \mathrm{Im}\, G_k(\omega)$ at low energy, beyond the cluster energy resolution (which is due to the finite dimension of the truncated Anderson impurity model used to implement CDMFT; see Fig. 6). As widely explained above, this relies on the implicit assumption that the superconducting gap has a d-wave form [see Eq. (24)] and at the node we have a well-defined Fermi liquid arc. The result is shown in Fig. 20. A "V-shaped" $N(\omega)$ is observed either in the overdoped or underdoped regions. Coming from the overdoped side toward the underdoped side, the slope is always decreasing, until reaching a saturating value at the small doping (until eventually showing a small up turn for the smaller doping; see Fig. 12). The slopes well fit the analytical value extracted at low energy in formula (32). On a wide range of energy $(-1<\omega<1)$, the V shape is quite symmetric in the overdoped region $\delta\geqslant\delta_c\sim0.08$ (as already remarked in the CTQMC-CDMFT study in Ref. 52). Spectra become strongly asymmetric in the underdoped region $(\delta\leqslant\delta_p\sim0.06)$ when the pseudogap in the normal part of the system opens and superimposes to the superconducting gap [as commented in panel (d) of Fig. 9]. The qualitative behavior of these curves should be compared with the raw cluster result of Fig. 6. The periodizing mixed scheme we discussed should be considered as the best fit we could achieve to our cluster DMFT results, based on few reasonable solid assumptions on the physical properties of the system (like the d-wave superconducting gap, the pseudogap formation, and the Fermi liquid properties at the node). This allows us to recover a momentum dependent Green's function and access physical quantities comparable to experimental results on

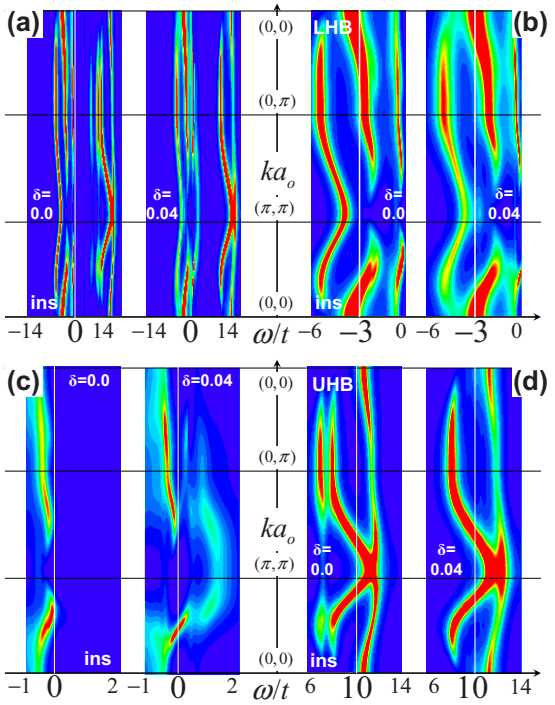

FIG. 21. (Color online) Band dispersion $A(k,\omega)$ along the path $(0,0)\rightarrow(\pi,\pi)\rightarrow(0,\pi)\rightarrow(0,0)$ in the first quadrant of the Brillouin zone. The Mott-insulating state ($\delta=0$) is confronted with a small doping ($\delta=0.04$) state. Panel (a): the full range of energies ($-15<\omega<15$) covered by the one-particle spectrum is displayed. The gross band structure, displaying a LHB ($-6<\omega<0$) and a UHB ($10<\omega<15$) separated by a Mott gap ($0<\omega<10$), remains unchanged in going from the insulator into the metal. Panel (b): detail of the LHB, which rigidly shifts in going from the insulating to the metallic state. Panel (c): detail of the low energy ($-1<\omega<2$) feature. In going into the metallic state, the shift of the bands is not rigid and spectral weight appears at positive energy as soon as doping is added into the system. Panel (d): detail of the UHB. Upon doping, a rigid shift in the metallic state is accompanied by a transfer of spectral weight to low energies. The color scale maximum value is always $x=0.20$, except for panel (d), where it is set $x=0.25$. We refer to Appendix A for the choice of the broadening $i\eta(\omega)$.

cuprates. The qualitative behavior of $N(\omega)$ we determined well portrays, in fact, results of scanning tunneling experiments,[69] and it supports a comparison in momentum space.

VI. QUASIPARTICLE SPECTRA FROM THE SUPERCONDUCTOR TO THE INSULATOR

In this section we use the mixed-periodization scheme and derive a detailed description of the connection between the spectra of the Mott insulator and the superconductor by varying doping.

A. Doping a Mott insulator

To this purpose, we analyze in Fig. 21 the spectral functions, $A(k,\omega)=-\frac{1}{t\pi}\,\mathrm{Im}\,G(k,\omega)$ in the $\omega-k$ space, along the k path $(0,0)\rightarrow(\pi,\pi)\rightarrow(0,\pi)\rightarrow(0,0)$ in the first quadrant of the Brillouin zone. We compare the insulating state ($\delta=0$) with a slightly doped state ($\delta=0.04$). In panel (a) we display a wide energy range $-14<\omega<14$, which covers the lower Hubbard band (LHB) and upper Hubbard band (UHB). We notice that, upon adding a small doping, the gross structure of the lower Hubbard band ($-6<\omega<0$) and the upper band ($10<\omega<15$), which are separated by a Mott gap ($0<\omega<10$), remains substantially unchanged. A detail of the lower Hubbard band, a closeup of the Fermi level ($-1<\omega<2$), and a detail of the upper Hubbard band are presented in panels (b), (c), and (d), respectively. The LHB [panel (b)] rigidly shifts in going from the insulating to the metallic state, loosing spectral intensity, which goes to build up quasiparticles at the Fermi level $\omega=0$ [panel (c)]. This structure bears resemblance (at least to some extend), with QMC results,[106,107] performed at high temperatures ($T>0.1t\sim T_C$). In these studies a four-band structure is found, consisting of two coherent bands close to the Fermi level and two incoherent bands forming the LHB and UHB. In our ED-CDMFT the Hubbard bands show a more rich structure (which partially reflects the pole-expansion structure of Green's functions in the ED implementation), but they both present a nondispersive incoherent feature at higher energies, similarly to the findings in Ref. 107. According to this latter study, upon doping, the chemical potential (at $\omega=0$) gradually cuts the topmost of the lower coherent band. This rigid-shift description is accompanied by a transfer of spectral weight from the high-energy Hubbard bands to lower coherent band close to the Fermi level, as in our CDMFT results. The different outcome from the CDMFT calculation, as compared with early QMC studies,[106,107] consists in the anisotropic fashion quasiparticles that first occupy the Fermi level in momentum space. The comparison is better elucidated in a closeup of the band dispersion around the Fermi level [panel (c)]. The region where first quasiparticles appear is close to $k=(\frac{\pi}{2},\frac{\pi}{2})$. In fact, already in the insulating state ($\delta=0$), we observe that around $k=(\frac{\pi}{2},\frac{\pi}{2})$ a heavy-particle hook-shaped band is closest to the $\omega=0$ level, while in the proximity of $k=(0,\pi)$ there is a "pseudogap" and the band disperses at negative energies. This kind of band structure survives upon doping, as we can observe in the $\delta=0.04$ panel. Contrary to the Hubbard bands, however, the low-energy band does not shift rigidly as doping is added to the insulator rather it stays pinned at the Fermi level, and the shift in frequency is only a small fraction of the change in chemical potential. We also observe the appearance of spectral weight at positive energy, coming from both the LHB and UHB, which starts building up a full Fermi-liquid-like band, as we show more in detail in the following. In panel (d) of Fig. 21 we finally show the UHB. In this case a rigid shift in the metallic state is accompanied by a strong reduction in spectral weight. In fact, according to our result, the UHB narrows with respect to the insulating state.

B. Approaching the Mott insulator from the overdoped side

We start now from the viewpoint of the highly doped system and observe how the approach to the Mott insulator

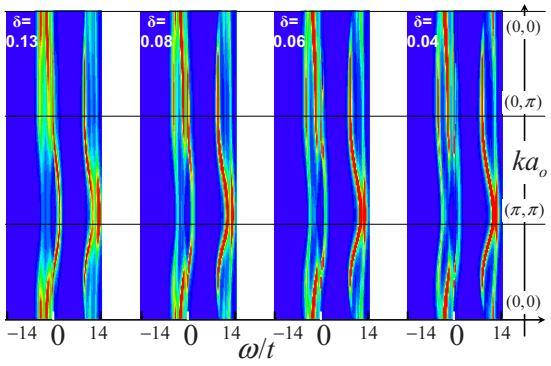

FIG. 22. (Color online) Evolution of the one-particle spectrum from the overdoped (left side, $\delta=0.13$) to the underdoped (right side, $\delta=0.04$) state. The typical Fermi-liquid band, well visible in a narrow energy range $(-1<\omega<1)$ around the Fermi level at high doping $\delta=0.13$, is progressively destroyed by reducing doping, while the upper and lower Hubbard bands build up acquiring spectral weight. These features are shown in detail in Figs. 23 and 24. The color scale maximum value is $x=0.20$ and we refer to Appendix A for the choice of the broadening $i\eta(\omega)$.

affects the electronic structure of the superconducting state. The high-doping system offers the advantage of having more standard Fermi-liquid-like properties [the patch $\Psi(k)$ introduced in the previous section covers all the momentum space]. In Fig. 22 we show the electronic band $A(k,\omega)$ in the k-ω space, once again in the path $(0,0)\rightarrow(\pi,\pi)\rightarrow(0,\pi)\rightarrow(0,0)$ of the first quadrant of the Brillouin zone, on the full energy range $10<\omega<15$ covering the LHB and UHB. Here we want to display the evolution from high doping (left) to small doping (right). At high a doping $\delta=0.13$ a Mott Hubbard gap which separates a LHB structure from the UHB is already visible. A narrow but Fermi-liquid-like band is however present, and it crosses the Fermi level both in the region of momentum space around $k=(\frac{\pi}{2},\frac{\pi}{2})$ and $k=(0,\pi)$ (see also Fig. 24). These features are also in good agreement with what is known already from QMC results.[107] Reducing the doping δ, we see that this narrow band loses intensity more and more [follow the horizontal line at $k=(\pi,\pi)$ in $\omega\sim0$] to the advantage of the Hubbard bands, which instead gain spectral weight in approaching the Mott insulator. To have a glance on how this is taking place we look in the following figures at the different energy regions of the band in further detail.

Figure 23 shows the UHB and the LHB. The statements made above are confirmed: both Hubbard bands gain spectral weight in decreasing doping, mainly in the region of momentum space close to the antinodes $k\sim(0,\pi)$ (follow once again the horizontal line) while rigidly shifting with respect to the change in chemical potential $\Delta\mu$ (one can actually show that the shift of the bands in energy is equal to $\Delta\mu$). The behavior of the Hubbard bands is therefore in agreement with a picture describing the approach to the Mott insulator as a rigidly moving bands,[6,107] which transfer part of their weight to low energy. As mentioned in the previous section, the different outcome of our CDMFT result in finite dimension, with respect to the standard vision of the Mott transition given by single-site DMFT in infinite dimension and

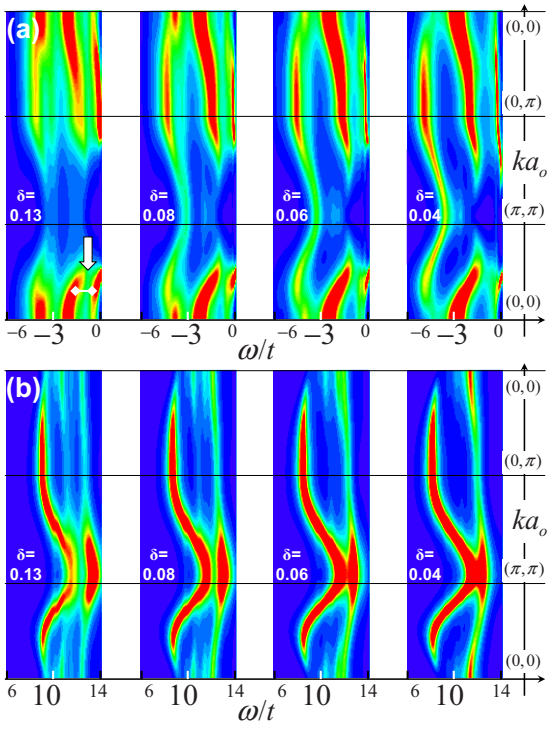

FIG. 23. (Color online) Panel (a): Evolution of the LHB from the overdoped (left side, $\delta=0.13$) to the underdoped (right side, $\delta=0.04$) state. The LHB rigidly shift according to the change in chemical potential by reducing doping, acquiring structure [follow the horizontal line at $k\sim(0,\pi)$]. Panel (b): Evolution of the UHB from the overdoped (left side, $\delta=0.13$) to the underdoped (right side, $\delta=0.04$) state. The UHB rigidly shift according to the change in chemical potential by reducing doping and, as evident in the color intensity, it gains spectral weight. The color scale maximum value is $x=0.20$ and we refer to Appendix A for the choice of the broadening $i\eta(\omega)$.

early QMC studies at higher temperature, is that this transfer of spectral weight takes place in a very anisotropic fashion, with the antinodal regions $k\sim(0,\pi)$ getting insulating before the nodal ones. The spectral weight at the Fermi level around $k\sim(0,\pi)$ is reduced, while it is enhanced at higher energies, rebuilding the dispersionless incoherent high-energy features of the Hubbard bands (as pointed out though, without the k anisotropy, already in Ref. 107).

A closer look (see Fig. 24) to the behavior at low energy (not accessible in the early QMC studies, like, e.g., Ref. 107) reveals much richer phenomena taking place. In the top panel we show the spectra resulting from one-particle Green's function $G_{11}(k,\omega)$ [Eq. (19)] in the superconducting state. First of all, contrary to the behavior of the Hubbard bands, the low-energy part of the band does not shift proportionally to $\Delta\mu$, in agreement with the observation already made in Fig. 21. The Fermi-liquid-like band at high doping (left side, $\delta=0.13$) is progressively destroyed by decreasing doping (with progressive reduction in spectral weight in the arc-shaped band at $0<\omega<2$). In the region close to $k=(0,\pi)$ instead, the d-wave superconducting state opens a gap by removing spectral weight from positive and negative energies (a Bogoliubov band is formed at $\omega>0$). As widely discussed in the previous sections, however, the presence of

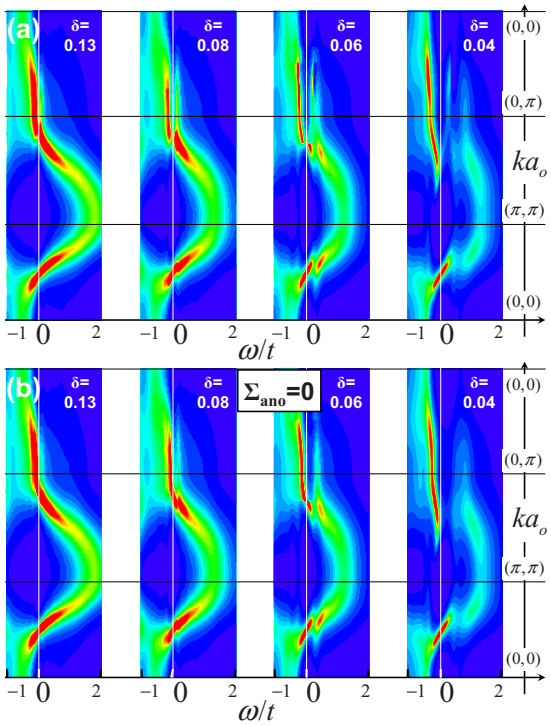

FIG. 24. (Color online) Panel (a): we show the evolution of the low-energy one-particle spectral band from the overdoped (left side, $\delta=0.13$) to the underdoped (right side, $\delta=0.04$) state. A Fermi-liquid-like band at high doping (left side, $\delta=0.13$) is progressively destroyed by decreasing doping. Around the region $k=(\frac{\pi}{2},\frac{\pi}{2})$ the dispersion presents a Fermi liquid quasiparticle crossing the Fermi level. Around the region $k=(0,\pi)$, the d-wave superconducting state opens a gap by removing spectral weight from the Fermi level to positive and negative energies. Panel (b): we show the contribution to the low-energy band coming from the normal component of the system (we set the anomalous self-energy $\Sigma_{ano}=0$). In particular, we observe that in the underdoped side ($\delta\leqslant 0.08$) a gap (the pseudogap) opens in the $k=(0,\pi)$ region even if the superconductive term is absent. For convenience's sake, the color scale maximum value is set $x=0.30$ for $\delta=0.13$ and $x=0.25$ for all the other doping values. We refer to Appendix A for the choice of the broadening $i\eta(\omega)$.

lines of zeroes in Green's function kicks in the underdoped region ($\delta<0.08$), opening a pseudogap in the normal component of $G_{11}(k,\omega)$ around $k=(0,\pi)$. This is shown in the bottom row of Fig. 24, where the same panels of the top row are reproduced by imposing the anomalous self-energy identically zero $\Sigma_{ano}=0$ in Eq. (19). Switching off superconductivity has in general little effect on the quasiparticle bands, except indeed close to the antinodal point $k\sim(0,\pi)$ and close to the Fermi level $\omega\sim 0$ [the nodal points $k\sim(\frac{\pi}{2},\frac{\pi}{2})$ are practically unaffected]. The differences are most evident in the overdoped region [see, e.g., $\delta\sim 0.13-0.08$ close to $k\sim(0,\pi)$], where the superconducting gap has disappeared and the quasiparticle band is reconstructed. The weight in the Bogoliubov branch at $\omega>0$ also disappears. For $\delta>\delta_c\sim 0.8$ differences are much less evident (above all $\delta=0.04$). A gap is also present in the normal component solution; the structure of the quasiparticle dispersion around $k\sim(0,\pi)$ is very reminiscent of the superconducting solution in the corresponding top row. It seems that in the underdoped region the superconducting gap completes the structure already present in the normal component solution. This suggests that the pseudogap, appearing in the normal component of the system (and present at temperatures above T_C), and the d-wave superconducting gap are possible answers of the system to the same instability, and they coexist in the underdoped region (while in the overdoped only the superconducting gap is present). This instability is, in our view, connected to the approach to the Mott transition, and it reflects the anisotropic way chosen by the Hubbard system in two dimensions to approach the insulating state: the regions around the antinodes $k\sim(0,\pi)$ become insulating (at $\delta=\delta_c\sim 0.08$) before the regions close to the nodes $k\sim(\frac{\pi}{2},\frac{\pi}{2})$ (which become insulating only at $\delta=0$).

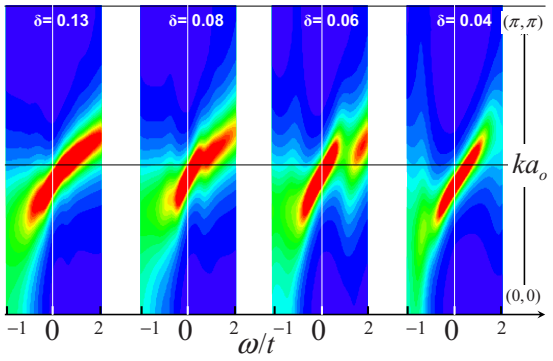

FIG. 25. (Color online) The low-energy kink feature in the spectral intensity at the nodal point for various values of doping. For convenience's sake, the color scale maximum values are set to $x=0.35$ for $\delta=0.13$ and $x=0.30$ for all the other doping values. We refer to Appendix A for the choice of the broadening $i\eta(\omega)$.

VII. LOW-ENERGY KINK IN THE QUASIPARTICLE SPECTRA

We can now compare the quasiparticle spectra presented in the previous section with the spectra measured, e.g., by photoemission, in cuprate-based systems. Unlike the linear dispersion predicted by simple band calculations, in recent years a series of experiments on the electronic structure of many H-T_C superconductor compounds has shown sharp breaks in the dispersion of spectra, kinks, at binding energies of the order of 50–80 meV.[109–113] Sudden changes in the quasiparticle velocity were reported by a factor 2 or more. This break in the dispersion is evident at and away from the d-wave node line, and its magnitude shows doping and temperature dependence. Kinks may provide useful information on the nature of the coupling between electrons and possible single-particle or many-body excitations, which are at the origin of strongly correlated many-body properties of the system. In H-T_C superconductors these features have been associated either with phonons[109,110] or spin-fluctuation based[111,112] pairing mechanisms.

In Fig. 25 the dispersion we observe in the quasiparticle band of our result around $k=(\frac{\pi}{2},\frac{\pi}{2})$ is similar to the experimentally observed kink (see, e.g., Ref. 108). A neat linearly

dispersing quasiparticle crosses the Fermi level ($\omega=0$) in the k-ω plot, but around $\omega\sim-0.2t$, the dispersion suddenly changes in slope and gets more incoherent, as evidenced by the broadening spectra. If we set $t\sim300$ meV as order of magnitude, we have that the kink appears at $\omega\sim60$ meV, in good agreement with the observed experimental energy range. The kink present in a wide range of doping, from the underdoped to the overdoped regime, and its slope are increasing with decreasing doping.

This energy kink in H-T_C superconductors raises the debate on the possible nature of the electron-electron coupling. In order for superconductivity to take place in metals, it is necessary that electrons bind into pairs, which condense in a phase-coherent quantum state. In standard BCS superconductivity, coupling between electrons and phonons (lattice vibrations) drives the formation of the pairs. The existence of the kink low-energy scale, not explicable in band theory calculation, may give a hint on the low-energy nature of the interaction between electrons and hence help revealing the pairing mechanism of the unconventional H-T_C superconductivity. The single-band Hubbard model studied in this paper does not take into account phonons by construction. Therefore the presence of the kink supports the idea that the origin of these features is indeed purely electronic, in agreement with the DMFT and CDMFT studies in Refs. 114 and 115. In Fig. 26 we present the spectral function $A(k,\omega)=-\frac{1}{\pi}\,\mathrm{Im}\,G(k,\omega)$ calculated in our theory, confronted with experimental ARPES data taken from Ref. 108. Panel (a) in the top of Fig. 26 shows $A(k,\omega)$ as a function of the energy ω, along two vertical cuts in the first quadrant of the Brillouin zone in correspondence of the nodal and antinodal regions, $(k_{nod},0)\sim(\frac{\pi}{2},0)\rightarrow(k_{nod},k_{nod})\sim(\frac{\pi}{2},\frac{\pi}{2})$ and $(k_{anod},0)\sim(\pi,0)\rightarrow(k_{anod},k_{nod})\sim(\pi,\frac{\pi}{2})$. The system is close to optimal doping $\delta_c\sim0.08$. In the left column we display the CDMFT calculation, while in the right column the experimental data, taken from Ref. 108. The nodal quasiparticle clearly shows a dispersion, which from the Fermi level propagates at negative frequencies until $\omega\sim-0.2t$, where it has a sudden broadening, indicating a strong incoherence. The antinodal quasiparticle shows instead a much flatter dispersion at energy corresponding to the superconductive gap, and the antinodal quasiparticle (which shows to have less weight than the nodal quasiparticle) does not lose much coherence. These plots have a good resemblance with the experimental data in the right column. The comparison between the energy scale of our results in the left $-t<\omega<0$ and of the experimental data -300 meV$<\omega<0$ shows also that the esteem we have used, $t\sim300$ meV, is a reasonable order of magnitude.

The same comparison is also presented in the intensity color plot in the bottom of Fig. 26, panel (b), where the nodal (left side) and the antinodal (right side) dispersions calculated with CDMFT are displayed (top rows), together with the experimental plots in Ref. 108 (bottom rows). From these diagrams, it is more evident the quasiparticlelike dispersion in the nodal point, which compares very well with the data from photoemission. In the photoemission, however, at $\omega\sim-0.075$ eV the quasiparticle appears loosing coherence (effect marked by the loss of red color that gets yellow) and at the same time the slope of the dispersion changes substantially. In the CDMFT calculation instead, as soon as the quasiparticle loses coherence (around $\omega\sim-0.2t$), the dispersion stops [i.e., is $\omega(k)\sim$const], and no spectral weight is present in the region at smaller energy ($\omega<-0.2t$). The kink appears

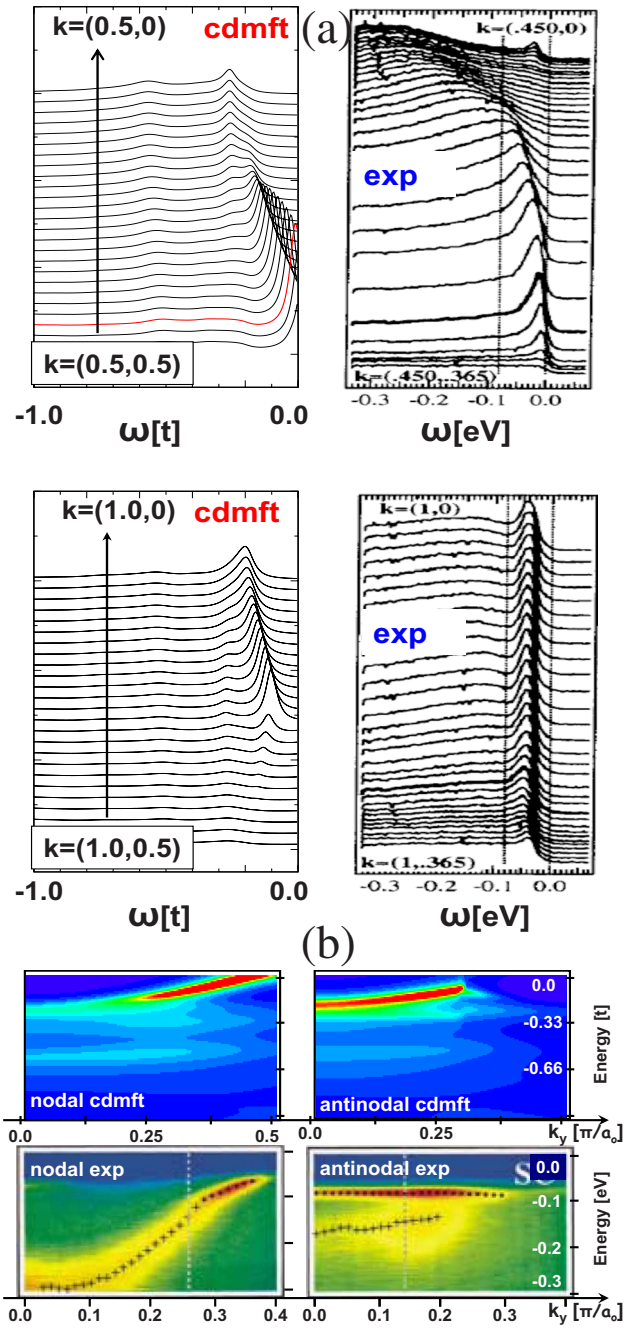

FIG. 26. (Color online) Top panel: The low energy spectral intensity $A(k,\omega)$ vs ω calculated within CDMFT (left) is confronted with the experimental result in Ref. 108 in the nodal and antinodal regions. Vertical cuts are traced in k space close to the node and the antinode, as traced on the figures. $\mathbf{k}$ is expressed in units of (π,π). Bottom panel: Color-intensity plots of the spectral intensity $A(k,\omega)$ in the k-ω space in the nodal (left) and antinodal (right) cuts of momentum space (the same used in the top panel). The color scale is set $x=0.30$ (see Appendix A). In the bottom row the experimental result in Ref. 108 are displayed for comparison. We refer to Appendix A for the choice of the broadening $\mathrm{i}\eta(\omega)$.

in our result as a "gap" in the ω vs k spectra. A similar phenomenon takes place at higher energies, as marked by an arrow in the top left panel of Fig. 23, where an evident gap is present in between the low energy band and the lower Hubbard band. This could be possibly associated with the "waterfall" dispersion features recently observed in many cuprate materials (see, e.g., Refs. 116 and 117) at energies ~350–600 meV, where the same k vector marks the dispersion $\omega(k)$ in a rather extensive range of energy. In our calculation this phenomenon is described as a gap in the dispersion. The antinodal point, where the superconducting gap is present, is nondispersing at low energy (right-bottom side in Fig. 26), and the resemblance of our result with the photoemission data is rather good.

VIII. HALL RESISTIVITY TO DETECT THE TOPOLOGICAL PHASE TRANSITION OF THE FERMI SURFACE

We have shown in Sec. V that in the underdoped region ($\delta < \delta_p \sim 0.06$) a different regime sets in our solution, marked by a topological transition from a large to a small Fermi surface (which reduces to an arc or pocket). The strong reduction in the Fermi surface area should correspond to a strong reduction in the carrier density too. This could be, in principle, experimentally detected by measuring the Hall resistivity $R_H = -\frac{1}{n_c e}$, which is directly related to the carrier density n_c, provided that superconductivity can be suppressed and the underlying normal liquid can be extracted. This latter is far from being a trivial procedure, which has many caveats. A standard method is, for example, to apply a magnetic field, which suppresses superconductivity. Recent publications have addressed this problem in $(Br_2Sr_{1.51}La_{49}CuO_{6+\delta})$ (BSLCO) (Ref. 98) and $La_{2-\delta}Sr_\delta CuO_4$ LSCO,[97] where magnetic field up to 65 T was applied, and in Nd-LSCO (Ref. 96) $(La_{1.6-x}Nd_{0.4}Sr_xCuO_4)$, where more moderate magnetic fields (up to 35 T) can totally suppress superconductivity. The results of these experiences on the Hall resistivity show, in fact, to be compatible with a reduction in the carrier density at low temperature in an underdoped sample (as we will discuss in more detail in the following).

In our study we can easily estimate the Hall resistivity by using a Boltzmann approach, similarly, for example, to the phenomenological study in Ref. 60. The Hall resistivity R_H can be expressed in terms of the in-plane conductivity (in the direction of an applied voltage) σ_{xx} and the transverse conductivity σ_{xy} (perpendicular to the applied voltage),

$$R_H = -\frac{\sigma_{xy}}{\sigma_{xx}^2 - \sigma_{xy}^2}\frac{1}{H}, \tag{39}$$

where H is the applied field. We can use the low-energy limit [similar to Eq. (30)] and extract the normal component of the system [by setting $\Sigma_{ano}=0$ in Eq. (19)]. Green's function is conveniently written on the Matsubara axis as

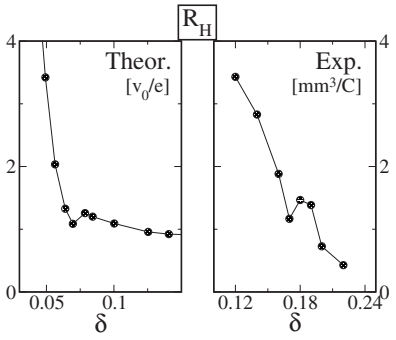

FIG. 27. Hall resistivity R_H as a function of doping δ. The topological phase transition of the Fermi surface is efficiently detected by a rapid change in the behavior in the Hall resistivity R_H, which indicates a change in the carrier density. Left: our theoretical result (units are in the unitary cell volume v_0 over electron charge e). Right: the experimental result for LSCO extracted from Ref. 97.

$$G(k,\omega_n) = \frac{1}{i\dfrac{(2n-1)\pi}{Z_k\beta} - \zeta_k}, \tag{40}$$

where a renormalized dispersion $\zeta_k = [\xi_k + \mathrm{Re}\Sigma_k(0)]$ and an inverse temperature β^{-1}, renormalized by the quasiparticle residuum Z_k, are introduced. We consider this liquid as the base on which to start applying a Boltzmann theory. The conductivities can then be expressed in the first order in H (see, e.g., Ref. 60),

$$\sigma_{xx} = -2e^2\tau\sum_k (v_k^x)^2 \frac{\partial f_{(Z_k\zeta_k)}}{\partial \zeta_k},$$

$$\sigma_{xy} = \frac{2e^3H\tau^2}{\hbar c}\sum_k v_k^x[v_k^y\partial_{k_x}v_k^y - v_k^x\partial_{k_y}v_k^y]\frac{\partial f_{(Z_k\zeta_k)}}{\partial \zeta_k}. \tag{41}$$

Here, $v_k^\nu = \partial\zeta_k/\partial k_\nu$ is $\nu = x,y$ component of the normal velocity, $f(x) = 1/(e^{\beta x}+1)$ is the Fermi function, and τ is the scattering time, which at $T=0$ is, for example, given by the impurities and which, for convenience's sake, we can hypothesize k independent in a first-order approach. In the pure model, such as the Hubbard model, this term is absent, so we have to add it in order to simulate the finite $T=0$ resistivity of a real material. As the Hall resistivity R_H is anyway independent of a constant τ, we do not need to make any special further assumption about it.

The Hall resistivity resulting from our calculation implemented via a mixed periodization and plugged into the Boltzmann expression is displayed on the left-hand side of Fig. 27 as a function of doping δ. The unit used to display R_H is the ratio between the unitary cell volume v_0 and the electron charge e. To give an idea of the order of magnitude, taking for LSCO (see, e.g., Ref. 118) an average lattice spacing $a_0 \sim 4$ Å $= 4\times10^{-7}$ mm in the Cu-O_2 planes, and $a_1 \sim 3a_0$ in the c axis, $\frac{v_o}{e} \sim 1.2$ mm^3/C, which well compares with the experimental results extracted from Ref. 97 [but similar results hold for BSLCO (Ref. 98)] and presented on the right-hand side. In the following, in drawing a parallel between

our theoretical result and the experimental data, one should keep in mind that in our study the "optimal doping" (which we can only identify with some degree of uncertainty as a maximum in the order parameter $\delta_c \sim 0.08 > \delta > \delta_p \sim 0.06$; see also the discussion in the conclusions) is situated at a smaller doping than the experimental value $\delta_{opt} \sim 0.17$.

R_H is positive, as expected by the holelike Fermi surface in the hole-doped system. As, in approaching the Mott insulator, the localization of particles reduces free carriers, R_H is generally expected to monotonically decrease with doping. Two regimes are clearly separable in our result (left side of Fig. 27). At $\delta \sim \delta_p \sim 0.06$ we observe a discontinuity in the behavior of R_H (which slightly decreases instead of increasing), and for $\delta < \delta_p$ a sudden increase in R_H, related to the topological phase transition of the Fermi surface presented in Sec. V, marks the reduction in the carriers in approaching the Mott state. Such a discontinuity is present and more evident in the experimental data (right side of Fig. 27). The presence of a local minimum at optimal doping $\delta_{opt} \sim 0.17$ represents a crucial point in the results presented in Refs. 97 and 98. This behavior is interpreted in terms of a quantum critical point, associated with a change in the topology from a large holelike Fermi surface (realized for $\delta > \delta_{opt}$) to a small (pocketlike) Fermi surface (realized for $\delta < \delta_{opt}$). According to their point of view, the force driving the superconductivity is related to the fluctuations around a critical point. This attractive force could overcome the mutual Coulomb repulsion of electrons, delocalizing and freeing carriers right in proximity of the quantum critical point. This fact would originate the local minimum in the Hall resistivity R_H (which is inversely proportional to the number of free carriers). The critical point would correspond then to the optimal doping δ_{opt}, where the critical temperature T_C is the highest.

Our result shows qualitatively very similar trends, with a minimum (even if milder) just at doping δ_p, where the topological transition of the Fermi surface takes place. This strongly supports the analysis of our results and the conclusion we have derived, in comparison with the experimental evidence on the Hall resistivity.

In our 2×2 plaquette study at $T=0$, however, we are not unfortunately able to state if δ_p is or not the optimal doping (which is defined at $T=T_C$). This point is as a matter of fact close to the maximum of the d-wave order parameter (as evident in Fig. 1). The study in Ref. 52 has pointed out that the exact determination of the optimal doping may depend on temperature. Also, we cannot demonstrate that $\delta_p \sim 0.06$ is a quantum critical point, as we have not clearly identified an order parameter or the divergence, to some order, in the free energy. Our study however finds good agreement with the experimental results in Refs. 96–98, and it is not in contradiction with their conclusions. We can, in fact, associate the discontinuity of R_H with a dramatic rearrangement of the electronic structure in the system, corresponding to the topological transformation of the Fermi surface. This happening is marked by a fast crossover region (between $\delta_c \sim 0.08 < \delta < \delta_p \sim 0.06$), where the maximum of order parameter is located, the pseudogap appears (at $\delta \sim \delta_c$), and the superconducting gap starts decreasing (at $\delta \sim \delta_p$). All these facts have striking consequences on spectra and transport properties, which we have presented throughout the paper.

More developments beyond the 2×2 plaquette CDMFT are needed, in order to be able to reveal if in reality $\delta_c \equiv \delta_p$ or rather they represent two different "transition" points. It would be then important to clarify if any of these points are a quantum critical point and their exact connection with the optimal doping δ_{opt} of the system. All these are important open questions left for future studies.

IX. CONCLUSION

A. Comparison with the resonating valence bond mean-field theory

CDMFT can be viewed as a generalization of the earlier slave boson resonating valence bond mean-field theory.[119,120] It is therefore useful to put our results in this context. RVB mean-field theories had numerous early successes, such as the prediction of d-wave superconductivity and a pseudogap phase having the same symmetry as the superconducting state.[68] Both RVB mean-field theories and our CDMFT study are formulated in terms of variables defined in a plaquette. The main differences stem from the fact that in CDMFT these variables are frequency dependent, and thus they are able to properly describe coherence to incoherence crossover in the momentum space. In the slave boson RVB mean-field theory there are two very important notions. The slave boson order parameter, which measures "Fermi liquid coherence," namely, the emergence of a well-defined quasiparticle peak in the spectral function, and the "spinon condensation" order parameter are both in the particle-particle and particle-hole channels. The position of the quasiparticle is shifted by a Lagrange multiplier which, adding to the bare chemical potential, forms a quasiparticle chemical potential. The dynamical mean-field picture of CDMFT develops these ideas, allowing them to acquire nontrivial dependence in momentum space.

To begin with, CDMFT describes naturally a high-temperature state showing poor coherence. As discussed in Ref. 34 and in Fig. 7, the peaks in the spectral functions in the normal state are broad and incoherent. It is only in the superconducting state that we can extract the Fermi liquid parameters discussed in this work. Coherence appears at low temperature in the nodal region more than in the antinodal region, as it is clearly seen, for example, in Fig. 7. Furthermore the weight of the quasiparticle is different (and larger in most of the phase diagram) in the nodal than in the antinodal region, as seen in Fig. 10. At small doping quasiparticles in the antinodal region cannot be defined in a strict Landau-Fermi liquid sense as a quasiparticle peak cannot be identified at the Fermi level anymore. As a matter of fact a pseudogap opens in the antinodal quasiparticle spectra. In the nodal region instead, quasiparticles are always well defined and their weight dramatically reduces as the doping is reduced. The slave boson RVB picture describes the pseudogap phase in terms of the formation of spin singlets, parametrized by order parameters, one describing correlations in the particle-particle channel and the second in the particle-hole channel. A similar but more complete description is achieved in terms of the dynamical anomalous and normal self-energies. Note the remarkable fact that the anomalous self-energy at low temperatures and at low frequencies has a similar order of magnitude as the normal self-energy (Figs. 2

and 5), indicating that, as in the RVB mean-field theory, they might both have a similar singlet-pairing origin deriving from the approach to the Mott insulator. On the other hand, the normal state self-energy has a more complicated angular dependence than the simple harmonic (d-wave) k dependence of the anomalous self-energy. In this sense, the normal and the anomalous gaps can also be viewed as competing for the same electrons, suggesting that further refinements of CDMFT along the lines in Ref. 121 are worth being pursued.

B. Scenario presented by our CDMFT results

While the dynamical frequency dependence introduced by DMFT well describes the low- to high-energy crossover, as well known from the infinite dimensional case,[6] the momentum dependence introduced by a cluster DMFT uncovers a wider spectrum of k-dependent physical phenomena, which turn out fundamental in describing the approach to the Mott transition in two dimensions.

In the first part of the paper (Sec. II) we have presented raw cluster quantities, which are direct output of the CDMFT procedure but which can be only partially interpreted in physical terms. Nevertheless we have shown that the doping-driven approach to the Mott transition takes place via an intermediate regime (rising after an "optimal doping region" $\delta_c \sim 0.08 > \delta > \delta_p \sim 0.06$), where physical properties depart from the standard picture of a BCS superconductor. In particular, we were able to identify two distinct energy scales, one associated with the anomalous component of the self-energy (see, e.g., Fig. 5) and the other better enlightened in the local density of states (see Fig. 6), showing different doping dependences. In the low doping regime the local spectra also show a strong asymmetry in ω, as observed in experiments[69] and contrary to the expectations from a BCS superconductor.

In order to physically interpret the genuine cluster results, we have restored the lattice translational invariance (broken in the CDMFT procedure) by introducing a periodization scheme. In Sec. III we have justified and compared two possible methods, based on periodization of the cluster self-energy and the cluster cumulant, respectively. To this purpose, we have discussed the physical properties of our system, taking advantage from either the cluster results (supported also by the comparison with CDMFT results obtained with QMC impurity-solver methods[33,52,81]) and experimental observation. We have performed a robust test on our approach by reconstructing the local quantities from the momentum-dependent Green's function $G(k,\omega)$ (see Fig. 20), which show to be not far from the corresponding cluster quantities obtained directly in the impurity model.

By introducing a periodization procedure in momentum space we were able to analyze our result in terms of experimentally observable quantities in the nodal and antinodal points of momentum space (Sec. IV), making contact with recent spectroscopy experiments.[70,71] In particular, we were able to interpret the two energy scales in terms of a pure superconducting gap (dominant in the nodes) coexisting with a normal component gap (related to the pseudogap of the normal state and dominant in the antinodal region of momentum space at low doping). We complete in this way the work presented in the short publication in Ref. 55.

We have then extended our procedure to describe in first approximation physical properties in all momentum space (Sec. V). The scenario which results presents an underdoped state where electronic structure undergoes a dramatic rearrangement. We could associate this fact with the appearance of a topological phase transition of the Fermi surface (see, e.g., Fig. 16), driven by the appearance in momentum space of lines of diverging self-energy fingerprints of the Mott physics. While these results may be quantitatively different for different periodizing methods, in terms of a large enhancement of the real part of the self-energies they indicate the same qualitative trends. Enhancement of self-energy Σ_k is most relevant in the cumulant scheme. The formation of a pseudogap in the antinodal region, however, only requires a large value of the self-energy and not a strict divergence (which in any case can only occur at $T=0$). Based on this physical idea, at finite doping the antinodal region is closer to the Mott insulating phase, while the nodal region is closer to the Fermi liquid state (see the band structure in Fig. 24 and the quasiparticle peaks in Fig. 9). We achieve in this way a consistent picture of the evolution of the electronic structure with doping within our formalism.

We were able to explain the strong asymmetry in the local density of states, observed, e.g., in scanning tunneling experiments.[69] We were able to give a complete description of the evolution of electronic spectra with varying doping, comparing the doped state with the Mott insulating one (see Sec. VI). In particular, we have shown that the transfer of spectral weight in approaching the Mott transition takes place in a strongly anisotropic fashion. We have described the behavior of the low-energy band close to the Fermi level, which is strongly renormalized by the interaction and progressively destroys by reducing doping, opening first a pseudogap in the antinodal region. This latter appears to be present already in the parent Mott insulator. We have stressed how this phenomenon is connected to the aforementioned lines of diverging self-energy. We have described how, from this underlying structure of the normal component, a d-wave superconducting gap rises. We have also shown (in Sec. VII) how the combination of these effects results in spectra which show kink features similar to the ones observed in the electronic dispersion of many photoemission experiments. Finally we have shown, using a simplified Boltzmann approach, how the-rising of the underdoped regime, associated in our study to a topological phase transition of the Fermi surface, is experimentally detectable from the doping-dependent behavior of transport quantities. Such as, for instance, a singularity in the Hall resistivity. All these properties are comparable with experiments on cuprate materials, and the good agreement we have found supports our study of the evolution with doping of the superconducting state of the Hubbard model, offering a self-consistent scenario of the approach to the Mott transition in two dimensions. This is most relevant in connection with cuprate H-T_C superconductors, in which the evolution of the electronic structure with doping (and its relation with H-T_C superconductivity) remains a fundamental open question. In particular, in recent times, the issue of two (nodal and antinodal) gaps[70,71] or one pure d-wave gap[122–124] has been at the center of the experimental and theoretical debate.[72,73,75] In this contest, our CDMFT results on the sim-

plest electronic model for H-T_C materials show a good agreement with the two-gap scenario and, at the same time, with many other electronic properties of cuprates.

An important question left open in our study is to determine the exact nature of the small "transition region" between $\delta_p \sim 0.06$ and $\delta_c \sim 0.08$, where fundamental changes take place in the physical properties of the system, in going from the Fermi liquid of the overdoped side into the anomalous liquid of the underdoped side of phase diagram. In particular, we have shown that lines of diverging self-energy appear at the Fermi level, a pseudogap opens in the one-particle spectrum, and a topological phase transition of the Fermi surface occurs (see Fig. 16). This small region of doping locates, within the numerical precision of our result, the "optimal doping," which we identify as a maximum in the d-wave order parameter (Fig. 1). All these observations point toward indicating a tight connection between the physical happening taking place in this optimal doping region and the H-T_C mechanism. We are not able to state within our study if behind lays a quantum critical point (which could provide the binding force for a high critical temperature). This scenario is actually supported by many theories[125–128] and experimental studies,[98,129,130] and it could be that further development of CDMFT (i.e., increasing cluster size) could reveal that the two points δ_p and δ_c actually coincide. Two distinct points could be actually present and one (or both) could have the characteristic of a quantum critical point. To reveal this, the right divergence in any order of the free energy and an order parameter should be clearly identified.

At present it is not possible to demonstrate that our solution will survive in the thermodynamic limit (i.e., in the infinite cluster size limit) in the sense that the real ground state of the Hubbard model in two dimensions could be another one of the possible competing instabilities, such as, e.g., stripe ordering or antiferromagnetism. The latter, in particular, is expected to be the ground state close to the Mott insulating state. Within a (dynamical) mean-field approach, however, we can study the pure paramagnetic phase, showing that it is a relevant phase even if it is not the true ground state of the system. We leave open the physical question of what terms need eventually to be added in the Hamiltonian in order to make this state a real ground state. In order to make our first-order picture more rigorous, further developments are needed. These should involve the cumulants directly in the self-consistency condition, as proposed, for example, in Refs. 46 and 121 and should exploit the flexibility of CDMFT, which can be formulated in terms of a set of adaptive patches in momentum space (on this line see the recent work[131]). Or CDMFT results could be used as the zeroth order approximation to include further nonlocal effects in a perturbative way, on the lines of Ref. 136. These extensions, as well as the use of more powerful solvers, which could allow going beyond a 2×2 cluster, are worth pursuing and are left for future studies.

ACKNOWLEDGMENTS

We thank G. Kotliar, who inspired many of the ideas in this work. We thank O. Parcollet and K. Haule for sharing their QMC results. We also acknowledge the fruitful discussion with A. Georges, M. Capone, and T. D. Stanescu. We enjoyed the exchange of ideas and the hospitality of A. Sacuto and the SQUAP group at the University of Paris 7. We acknowledge A.-M. S. Tremblay, S. S. Kancharla, B. Kyung, I. Paul, A. Cano, E. Kats, and P. Nozières for their useful comments. We thank V. Oudovenko for his prompt computing support.

APPENDIX A: DISPLAYING FUNCTION ON THE REAL AXIS WITH ED-CDMFT

Once the ground state $|\mathrm{gs}\rangle$ of the associate Anderson impurity model [Eq. (8)] has been determined via the Lanczos procedure, it is possible to determined the zero-temperature Green's function via a second Lanczos step (see, e.g., the review[6]). To this purpose, one has to take as initial vector $c_i^\dagger|\mathrm{gs}\rangle$ (i denoting the generic cluster-site index) and write the ground-state Green's function in a continued-fraction expansion, describing the "particle" and "hole" excitations

$$G(\omega_n) = G^{>}(\omega_n) + G^{>}(\omega_n), \tag{A1}$$

with

$$G^{>}(\omega_n) = \cfrac{\langle \mathrm{gs}|c_i c_i^\dagger|\mathrm{gs}\rangle}{\mathrm{i}\omega_n - a_0^{>} - \cfrac{b_1^{>2}}{\mathrm{i}\omega_n - a_1^{>} - \cfrac{b_2^{>2}}{\mathrm{i}\omega_n - a_2^{>} - \cdots}}},$$

$$G^{<}(\omega_n) = \cfrac{\langle \mathrm{gs}|c_i^\dagger c_i|\mathrm{gs}\rangle}{\mathrm{i}\omega_n - a_0^{<} - \cfrac{b_1^{<2}}{\mathrm{i}\omega_n - a_1^{<} - \cfrac{b_2^{<2}}{\mathrm{i}\omega_n - a_2^{<} - \cdots}}}. \tag{A2}$$

The parameters a_j^α and b_j^α ($j=1,\ldots$ number of Lanczos steps, $\alpha=>,<$) output directly from the second Lanczos step.[132] In the ED-CDMFT procedure the cluster Green's function and the self-consistency [Eq. (4)] are evaluated on the Matsubara axis. This implies introducing a parameter β which determines the grid of Matsubara points $\omega_n=(2n-1)\pi/\beta$ and which plays the role of a fictitious temperature (our solution is however at zero temperature). We can easily analytically continue Green's functions by replacing in the continued-fraction expansion [Eq. (A2)],

$$\mathrm{i}\omega \to \omega + \mathrm{i}\eta, \tag{A3}$$

where ω is the real axis frequency and η a small parameter used to display the poles. It is difficult to know *a priori* the smallest value we can assign to η. It depends on the physical problem considered, on the size of the associated Anderson impurity problem used in the Lanczos procedure, and on the energy resolution imposed in satisfying the self-consistency condition on the Matsubara axis (i.e., the parameter β). A reasonable guess for a lower bound value would be, for example, $\eta \approx \pi/\beta$. Moreover we expect η to be frequency dependent too. The Lanczos better determines the ground state of the system and portrays better low-energy properties. The

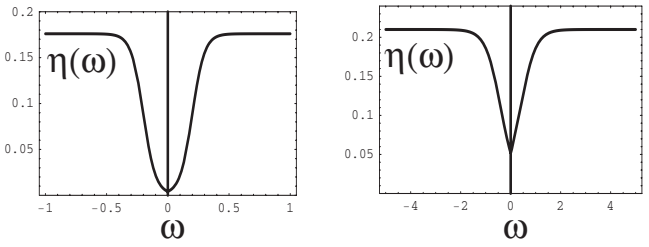

FIG. 28. Example of the broadening $\eta(\omega)$ used to display spectral function on the real axis. Left: the low energy range $-1<\omega<1$ example of Fig. 20. Right: the wide energy range example of Fig. 19. For a complete list of $\eta(\omega)$ see table in Appendix A.

uncertainty in the ground-state vector $|\mathrm{gs}\rangle$ propagates in the determination of the a_j^α and b_j^α coefficients (which is a further Lanczos step) and further propagates in the periodization procedures (Sec. III). The error in the second Lanczos step turns out much bigger at higher frequency, and, if η is chosen too small, this can create enormous errors and even break causality [which is instead by construction always satisfied in the impurity solver output, i.e., in the cluster Green's function of Eq. (6)]. A too big value of η results however in a poor resolution, which may hide important features, above all at small energy. In order to be able to display at the same time high- and low-energy features, we have introduced for convenience's sake in Sec. III (with the only exception of Fig. 7, see the corresponding caption) and V–VII a ω dependent η, arbitrarily choosing a function shape which quickly separates a low- from a high-energy range (see Fig. 28),

$$\eta(\omega) = \eta_0 + \frac{\eta_1}{e^{-|\omega-\omega_0|/T_w}+1}. \tag{A4}$$

The branching between the low- and high-energy regimes takes place in a Fermi-function-like step at $\omega=\omega_0$ with rapidity $1/T_w$. In Fig. 28 we report as example the $\eta(\omega)$ adopted to display the local density of states of Fig. 20 (on the left), where the low-energy range is $-1<\omega<1$, and (on the right) the $\eta(\omega)$ of the density plots of Figs. 19 and 21, where the full energy scale $-14<\omega<14$, including the lower and upper Hubbard bands, is considered. In the following we report exactly the values of the parameters determining $\eta(\omega)$ for all the figures involved:

Figures	η_0	η_1	ω_0	T_w
8, top panel	0.01	0.15	0.05	0.01
8, middle and bottom panels	0.001	0.05	0.05	0.01
19 and 21–25	0.01	0.2	0.4	0.3
20	0.001	0.175	0.2	0.05
26	0.025	0.04	0.2	0.025

It is clear that spectral peaks displayed with different $\eta(\omega)$ at different frequencies present uncomparable heights and widths. Our task is not however to make this kind of comparison but rather to focalize on the position of the spectral peaks and compare heights and widths at different dopings

FIG. 29. (Color online) Color scale code adopted in displaying the color-density plots. x is the maximum value of the scale.

(but at the same frequency). This has to be kept in mind when analyzing these figures.

Finally, the color code we adopted to display the density plots (see, e.g., Figs. 19 and 21–25) is shown in Fig. 29. x is the maximum value of the scale, which we have chosen according to the picture (see the corresponding caption). If the value of the function displayed is bigger than x, the color remains red.

APPENDIX B: SUPERCONDUCTING BATH PARAMETRIZATION WITHIN CDMFT

The general form of the associated cluster-Anderson impurity Hamiltonian $\mathcal{H}_{\mathrm{imp}}$ can be written as

$$\begin{aligned}\mathcal{H}_{\mathrm{imp}} = &\sum_{ij\sigma} E_{ij\sigma} c_{i\sigma}^\dagger c_{j\sigma} + U\sum_i n_{i\uparrow}n_{i\downarrow} + \sum_{k\sigma} \epsilon_{k\sigma} a_{k\sigma}^\dagger a_{k\sigma} \\ &+ \sum_{ki\sigma} V_{ki\sigma} a_{k\sigma}^\dagger c_{i\sigma} + \mathrm{H.c.} + \sum_{ki\sigma} V_{ki\sigma}^{\mathrm{sup}} a_{k\sigma}^\dagger c_{i\bar{\sigma}}^\dagger \\ &+ \sum_{ki\sigma} V_{ki\sigma}^{\dagger\mathrm{sup}} c_{i\bar{\sigma}} a_{k\sigma}.\end{aligned} \tag{B1}$$

Here $i,j=1,\ldots,N_c$ label the sites in the cluster and $E_{ij\sigma}$ represents the hopping and the chemical potential within the cluster. $\varepsilon_{k\sigma}$ is the energy level of the (k,σ) orbital in the free electron bath, V's represent the hybridization hopping amplitude either for a particle destruction/construction or for the singlet destruction/destruction (construction/construction) between the electrons in the impurity cluster and the bath. In order to drive the solutions toward physically interesting regions of the bath-parameter space, in this 2×2 plaquette study we have introduced a reduced bath parametrization[36] which allows exploiting the symmetries in the square lattice to gain a better physical insight of Green's-function symmetries. Moreover using fewer parameters the work required by the minimization procedure is faster, the number of CDMFT steps greatly reduced, and the result is simpler to interpret,

$$\begin{aligned}\mathcal{H}_{\mathrm{imp}}^R = &\sum_{ij\sigma} E_{ij\sigma} c_{i\sigma}^\dagger c_{j\sigma} + U\sum_i n_{i\uparrow}n_{i\downarrow} \sum_{mm'\sigma} \epsilon_{mm'\sigma}^\alpha a_{m'\sigma}^{\dagger\alpha} a_{m\sigma}^\alpha \\ &+ \sum_{mi\sigma} V_{mi\sigma}^\alpha a_{m\sigma}^{\dagger\alpha} c_{i\sigma} + \mathrm{H.c.} + \sum_\alpha \Delta^\alpha (a_{1\uparrow}^\alpha a_{2\downarrow}^\alpha - a_{2\uparrow}^\alpha a_{3\downarrow}^\alpha \\ &+ a_{3\uparrow}^\alpha a_{4\downarrow}^\alpha - a_{4\uparrow}^\alpha a_{1\downarrow}^\alpha + a_{2\uparrow}^\alpha a_{1\downarrow}^\alpha - a_{3\uparrow}^\alpha a_{2\downarrow}^\alpha + a_{4\uparrow}^\alpha a_{3\downarrow}^\alpha - a_{1\uparrow}^\alpha a_{4\downarrow}^\alpha) \\ &+ \mathrm{H.c.}\end{aligned} \tag{B2}$$

The energy levels in the bath are grouped into multiples of the cluster size ($N_c=4$) with the labels $m=1,\ldots,N_c$ and $\alpha=1,2$ such that we have eight bath energy levels $\varepsilon_{m\sigma}^\alpha$ coupled to the cluster via the hybridization matrix $V_{mi\sigma}^\alpha$. Using lattice symmetries we take $V_{mi\sigma}^\alpha \equiv V^\alpha \delta_{mi}$ and $\varepsilon_{m\sigma}^\alpha \equiv \varepsilon^\alpha$. Δ^α represents the amplitude of superconducting correlations in the bath. No static mean-field order parameter acts directly on the cluster sites.[36,133] ε^α, V^α, and Δ^α are determined by im-

posing the self-consistency condition in Eq. (4) using a conjugate gradient minimization algorithm with a distance function that emphasizes the lowest frequencies of the Weiss field[53] [see Eq. (12)]. The reduced form [Eq. (B2)] is, in fact, a subcase of the more general Hamiltonian (B1), and a canonical transformation connects Eq. (B2) to Eq. (B1). In order to see this, it is most convenient to express $\mathcal{H}$ in Nambu's form, introducing cluster-plaquette spinors,

$$\Psi_c^\dagger \equiv (c_{1\uparrow}^\dagger, \ldots, c_{4\uparrow}^\dagger, c_{1\downarrow}, \ldots, c_{4\downarrow}),$$

$$\Phi_a^\dagger \equiv (a_{1\uparrow}^\dagger, \ldots, a_{4\uparrow}^\dagger, a_{1\downarrow}, \ldots, a_{4\downarrow}), \tag{B3}$$

and recast the Hamiltonian,

$$\mathcal{H}_{\text{imp}} = \Psi^\dagger \mathbf{E} \Psi + U \sum_i n_{i\uparrow} n_{i\downarrow} + \sum_\alpha \Phi_\alpha^\dagger \mathbf{E}_B^\alpha \Phi_\alpha + \Phi_\alpha^\dagger \mathbf{V}_\alpha \Psi + \Psi^\dagger \mathbf{V}_\alpha^\dagger \Phi_\alpha, \tag{B4}$$

where the Hamiltonian coupling constants are expressed by 8×8 matrices (leaving for convenience's sake the multibath index α implicit),

$$\mathbf{E} = \begin{pmatrix} E_{i,j,\uparrow}(4\times 4) & 0 \\ 0 & E_{i,j,\downarrow}(4\times 4) \end{pmatrix},$$

$$\mathbf{E_B} = \begin{pmatrix} \mathbf{E}_{B_\uparrow}(4\times 4) & \mathbf{E}_B^S(4\times 4) \\ \mathbf{E}_B^{S\dagger}(4\times 4) & -\mathbf{E}_{B_\downarrow}(4\times 4) \end{pmatrix},$$

and

$$\mathbf{V} = \begin{pmatrix} \mathbf{V}_\uparrow(4\times 4) & \mathbf{V}_\uparrow^S(4\times 4) \\ -\mathbf{V}_\uparrow^{S\dagger}(4\times 4) & -\mathbf{V}_\downarrow(4\times 4) \end{pmatrix}.$$

In the more general case $\mathcal{H}_{imp}^{B1}$, the bath matrix is diagonal, so that $\mathbf{E}_{\mathbf{B}\sigma}^{\mathbf{k}\mathbf{k}'B1} = \delta_{kk'}\varepsilon_{k\sigma}$, and $\mathbf{E}_{\mathbf{B}}^{\mathbf{S}B1} = 0$. $\mathbf{V}_\sigma$ and $\mathbf{V}_\sigma^S$ have generally nonzero elements. In the reduced parametrization case instead [Eq. (B2)], the bath matrix is not diagonal but chosen to mimic a cluster plaquette by introducing in each multibath α the same bath energy $\varepsilon_{\alpha\sigma}$ on every bath site, a next-neighbor hopping t_b^α and a nearest-next-neighbor hopping $t_b'^\alpha$,

$$\mathbf{E}_{\mathbf{B}_\sigma}^{\alpha\ B2} = \begin{pmatrix} \varepsilon_{\alpha\sigma} & t_b^\alpha & t_b'^\alpha & t_b^\alpha \\ t_b^\alpha & \varepsilon_{\alpha\sigma} & t_b^\alpha & t_b'^\alpha \\ t_b'^\alpha & t_b^\alpha & \varepsilon_{\alpha\sigma} & t_b^\alpha \\ t_b^\alpha & t_b'^\alpha & t_b^\alpha & \varepsilon_{\alpha\sigma} \end{pmatrix}.$$

Moreover superconductive d-wave pairing terms Δ_α appear in the bath,

$$\mathbf{E}_{\mathbf{B}}^{\mathbf{S}\alpha B2} = \begin{pmatrix} 0 & \Delta_\alpha & 0 & -\Delta_\alpha \\ \Delta_\alpha & 0 & -\Delta_\alpha & 0 \\ 0 & -\Delta_\alpha & 0 & \Delta_\alpha \\ -\Delta_\alpha & 0 & \Delta_\alpha & 0 \end{pmatrix},$$

while the hybridization between the cluster and the bath is only normal $\mathbf{V}_\sigma^S = 0$ and simplified by connecting each site of the cluster i with only one site k_i^α of the multibath α with the same coupling constant $V_{\sigma\alpha}$,

$$\mathbf{V}_{\sigma\alpha}^{B2} = \begin{pmatrix} V_{\sigma\alpha} & 0 & 0 & 0 \\ 0 & V_{\sigma\alpha} & 0 & 0 \\ 0 & 0 & V_{\sigma\alpha} & 0 \\ 0 & 0 & 0 & V_{\sigma\alpha} \end{pmatrix}.$$

To connect the reduced parametrization equation [Eq. (B2)] to the general equation [Eq. (B1)] it is sufficient to diagonalize the Hermitian bath matrix $\mathbf{E}_{\mathbf{B}}^\alpha$ via a unitary transformation,[54]

$$\mathbf{E}_{\mathbf{B}}^{\alpha B1} = \mathbf{S}_\alpha^\dagger \mathbf{E}_{\mathbf{B}}^{\alpha B2} \mathbf{S}_\alpha \tag{B5}$$

and $\mathbf{S}_\alpha^{\mathbf{T}} \mathbf{S}_\alpha = \mathbf{1}$. This is, in fact, the requirement needed to have a canonical transformation which preserves the fermionic commutation relations. In fact, if we apply the transformation to the vectors,

$$\mathbf{\Phi}_\alpha^{\ B2} = \mathbf{S}_\alpha \mathbf{\Phi}_\alpha^{\ B1},$$

$$\mathbf{\Phi}_\alpha^{\dagger B2} = \mathbf{\Phi}_\alpha^{\dagger B1} \mathbf{S}_\alpha^\dagger, \tag{B6}$$

and we have

$$\{\mathbf{\Phi}_\alpha^{\ B2}, \mathbf{\Phi}_\alpha^{\dagger B2}\} = \mathbf{1}, \tag{B7}$$

it is

$$\{\Phi_{q\alpha}^{B1}, \Phi_{q\alpha}^{\dagger B1}\} \tag{B8}$$

$$= \sum_{kk'} S_{qk}^\dagger S_{k'q} \{\Phi_{k\alpha}^{B2}, \Phi_{k'\alpha}^{\dagger B2}\} \tag{B9}$$

$$= \sum_k S_{qk}^\dagger S_{kq} = 1. \tag{B10}$$

Finally $\mathbf{V}_\alpha$ is subjected to the same transformation,

$$\mathbf{V}_\alpha^{B1} = \mathbf{S}_\alpha^\dagger \mathbf{V}_\alpha^{B2}. \tag{B11}$$

[1] P. W. Anderson, Science **235**, 1196 (1987).
[2] J. G. Bednorz and K. A. Muller, Z. Phys. B: Condens. Matter **64**, 189 (1986).
[3] Y. Kamihara, T. Watanabe, M. Hirano, and H. Hosono, J. Am. Chem. Soc. **130**, 3296 (2008).
[4] C. Day, Phys. Today **61** (5), 11 (2008).
[5] W. Metzner and D. Vollhardt, Phys. Rev. Lett. **62**, 324 (1989).
[6] A. Georges, G. Kotliar, W. Krauth, and M. J. Rozenberg, Rev.

Mod. Phys. **68**, 13 (1996).
[7] G. Kotliar and D. Vollhardt, Phys. Today **57** (3), 53 (2004).
[8] M. Jarrell, Phys. Rev. Lett. **69**, 168 (1992).
[9] A. Georges and W. Krauth, Phys. Rev. B **48**, 7167 (1993).
[10] R. Zitzler, Th. Pruschke, and R. Bulla, Eur. Phys. J. B **27**, 473 (2002).
[11] M. Fleck, A. I. Lichtenstein, and A. M. Oleś, Phys. Rev. B **64**, 134528 (2001).
[12] M. Fleck, A. I. Lichtenstein, A. M. Oleś, and L. Hedin, Phys. Rev. B **60**, 5224 (1999).
[13] N. E. Zein, S. Y. Savrasov, and G. Kotliar, Phys. Rev. Lett. **96**, 226403 (2006).
[14] A. Lichteinstein and A. Liebsch, *Ruthenate and Rutheno-Cuprate Materials: Unconventional Superconductivity, Magnetism and Quantum Phase Transitions* (Springer-Verlag, Berlin, 2002).
[15] K. Held, A. K. McMahan, and R. T. Scalettar, Phys. Rev. Lett. **87**, 276404 (2001).
[16] K. Haule, V. Oudovenko, S. Y. Savrasov, and G. Kotliar, Phys. Rev. Lett. **94**, 036401 (2005).
[17] S. Savrasov, G. Kotliar, and E. Abrahams, Nature (London) **410**, 793 (2001).
[18] G. Kotliar, S. Savrasov, K. Haule, V. Oudovenko, O. Parcollet, and C. Marianetti, Rev. Mod. Phys. **78**, 000865 (2006).
[19] A. Damascelli, Z. X. Shen, and Z. Hussain, Rev. Mod. Phys. **75**, 473 (2003).
[20] J. C. Campuzano, M. R. Norman, M. Randeria, K. H. Bennemann, and J. B. Ketterson, *Physics of Superconductors II* (Springer, New York, 2004), pp. 167–273.
[21] Th. Maier, M. Jarrell, Th. Pruschke, and M. Hettler, Rev. Mod. Phys. **77**, 1027 (2005).
[22] G. Biroli, O. Parcollet, and G. Kotliar, Phys. Rev. B **69**, 205108 (2004).
[23] A. I. Lichtenstein and M. I. Katsnelson, Phys. Rev. B **62**, R9283 (2000).
[24] Th. Maier, M. Jarrell, Th. Pruschke, and J. Keller, Phys. Rev. Lett. **85**, 1524 (2000).
[25] A.-M. S. Tremblay, B. Kyung, and D. Sénéchal, Low Temp. Phys. **32**, 424 (2006).
[26] G. Kotliar, S. Y. Savrasov, G. Palsson, and G. Biroli, Phys. Rev. Lett. **87**, 186401 (2001).
[27] M. Fleck, A. I. Lichtenstein, M. G. Zacher, W. Hanke, and A. M. Oleś, Eur. Phys. J. B **37**, 439 (2004).
[28] J. E. Hirsch and R. M. Fye, Phys. Rev. Lett. **56**, 2521 (1986).
[29] R. M. Fye and J. E. Hirsch, Phys. Rev. B **40**, 4780 (1989).
[30] T. A. Maier, M. Jarrell, T. C. Schulthess, P. R. C. Kent, and J. B. White, Phys. Rev. Lett. **95**, 237001 (2005).
[31] T. A. Maier, M. S. Jarrell, and D. J. Scalapino, Phys. Rev. Lett. **96**, 047005 (2006).
[32] D. Sénéchal, and A.-M. S. Tremblay, Phys. Rev. Lett. **92**, 126401 (2004).
[33] O. Parcollet, G. Biroli, and G. Kotliar, Phys. Rev. Lett. **92**, 226402 (2004).
[34] M. Civelli, M. Capone, S. S. Kancharla, O. Parcollet, and G. Kotliar, Phys. Rev. Lett. **95**, 106402 (2005).
[35] B. Kyung, S. S. Kancharla, D. Sénéchal, A.-M. S. Tremblay, M. Civelli, and G. Kotliar, Phys. Rev. B **73**, 165114 (2006).
[36] S. S. Kancharla, B. Kyung, D. Sénéchal, M. Civelli, M. Capone, G. Kotliar, and A.-M. S. Tremblay, Phys. Rev. B **77**, 184516 (2008).
[37] M. Capone and G. Kotliar, Phys. Rev. B **74**, 054513 (2006).
[38] M. Aichhorn, E. Arrigoni, M. Potthoff, and W. Hanke, Phys. Rev. B **74**, 235117 (2006).
[39] M. Aichhorn, E. Arrigoni, M. Potthoff, and W. Hanke, Phys. Rev. B **74**, 024508 (2006).
[40] D. Sénéchal, P.-L. Lavertu, M.-A. Marois, and A.-M. S. Tremblay, Phys. Rev. Lett. **94**, 156404 (2005).
[41] E. C. Carter and A. J. Schofield, Phys. Rev. B **70**, 045107 (2004).
[42] Z. Tesanovic, Nat. Phys. **4**, 408 (2008).
[43] C. Huscroft, M. Jarrell, Th. Maier, S. Moukouri, and A. N. Tahvildarzadeh, Phys. Rev. Lett. **86**, 139 (2001).
[44] T. D. Stanescu and P. Phillips, Phys. Rev. Lett. **91**, 017002 (2003).
[45] F. H. L. Essler and A. M. Tsvelik, Phys. Rev. B **65**, 115117 (2002).
[46] T. D. Stanescu and G. Kotliar, Phys. Rev. B **74**, 125110 (2006).
[47] C. Berthod, T. Giamarchi, S. Biermann, and A. Georges, Phys. Rev. Lett. **97**, 136401 (2006).
[48] S. Sakai, Y. Motome, and M. Imada, Phys. Rev. Lett. **102**, 056404 (2009).
[49] T. D. Stanescu, P. W. Phillips, and T.-P. Choy, Phys. Rev. B **75**, 104503 (2007).
[50] K. Haule and G. Kotliar, Phys. Rev. B **76**, 092503 (2007).
[51] M. Caffarel and W. Krauth, Phys. Rev. Lett. **72**, 1545 (1994).
[52] K. Haule and G. Kotliar, Phys. Rev. B **76**, 104509 (2007).
[53] M. Capone, M. Civelli, S. S. Kancharla, C. Castellani, and G. Kotliar, Phys. Rev. B **69**, 195105 (2004).
[54] M. Civelli, Ph.D. thesis, Rutgers, The State University of New Jersey, 2006, arXiv:0710.2802
[55] M. Civelli, M. Capone, A. Georges, K. Haule, O. Parcollet, T. D. Stanescu, and G. Kotliar, Phys. Rev. Lett. **100**, 046402 (2008).
[56] J.-C. Domenge and G. Kotliar, arXiv:0808.2328 (unpublished).
[57] P. A. Lee, N. Nagaosa, and X.-G. Wen, Rev. Mod. Phys. **78**, 17 (2006).
[58] G. Biroli and G. Kotliar, Phys. Rev. B **65**, 155112 (2002).
[59] T. D. Stanescu, M. Civelli, K. Haule, and G. Kotliar, Ann. Phys. **321**, 1682 (2006).
[60] A. Perali, M. Sindel, and G. Kotliar, Eur. Phys. J. B **24**, 487 (2002).
[61] J. Hubbard, Proc. R. Soc. London, Ser. A **276**, 238 (1963).
[62] C. J. Bolech, S. S. Kancharla, and G. Kotliar, Phys. Rev. B **67**, 075110 (2003).
[63] E. Koch, G. Sangiovanni, and O. Gunnarsson, Phys. Rev. B **78**, 115102 (2008).
[64] Michael Potthoff, Phys. Rev. B **64**, 165114 (2001).
[65] E. H. Lieb and F. Y. Wu, Phys. Rev. Lett. **20**, 1445 (1968).
[66] B. Kyung, G. Kotliar, and A.-M. S. Tremblay, Phys. Rev. B **73**, 205106 (2006).
[67] K. Haule, Phys. Rev. B **75**, 155113 (2007).
[68] G. Kotliar and J. Liu, Phys. Rev. B **38**, 5142(R) (1988).
[69] K. McElroy, D.-H. Lee, J. E. Hoffman, K. M. Lang, J. Lee, E. W. Hudson, H. Eisaki, S. Uchida, and J. C. Davis, Phys. Rev. Lett. **94**, 197005 (2005).
[70] M. Le Tacon, A. Sacuto, A. Georges, G. Kotliar, Y. Gallais, D. Colson, and A. Forget, Nat. Phys. **2**, 537 (2006).
[71] K. Tanaka, W. S. Lee, D. H. Lu, A. Fujimori, T. Fujii, Risdiana, I. Terasaki, D. J. Scalapino, T. P. Devereaux, Z. Hussain, and Z.-X. Shen, Science **314**, 1910 (2006).
[72] A. Cho, Science **314**, 1072 (2006).

[73] A. J. Millis, Science **314**, 1888 (2006).
[74] G. Deutscher, Nature (London) **397**, 410 (1999).
[75] S. Huefner, M. A. Hossain, A. Damascelli, and G. A. Sawatzky, Rep. Prog. Phys. **71**, 062501 (2008).
[76] T. Kondo, T. Takeuchi, A. Kaminski, S. Tsuda, and S. Shin, Phys. Rev. Lett. **98**, 267004 (2007).
[77] K. K. Gomes, A. N. Pasupathy, A. Pushp, S. Ono, Y. Ando, and A. Yazdani, Nature (London) **447**, 569 (2007).
[78] L. B. Ioffe and A. J. Millis, Phys. Rev. B **58**, 11631 (1998).
[79] A. T. Zheleznyak, V. M. Yakovenko, H. D. Drew, and I. I. Mazin, Phys. Rev. B **57**, 3089 (1998).
[80] R. Hlubina and T. M. Rice, Phys. Rev. B **51**, 9253 (1995).
[81] O. Parcollet (private communication).
[82] H. Matsui, T. Sato, T. Takahashi, S.-C. Wang, H.-B. Yang, H. Ding, T. Fujii, T. Watanabe, and A. Matsuda, Phys. Rev. Lett. **90**, 217002 (2003).
[83] J. M. Luttinger, Phys. Rev. **119**, 1153 (1960).
[84] L. De Leo, M. Civelli, and G. Kotliar, Phys. Rev. Lett. **101**, 256404 (2008).
[85] M. Ferrero, F. Becca, M. Fabrizio, and M. Capone, Phys. Rev. B **72**, 205126 (2005).
[86] L. de'Medici, A. Georges, and S. Biermann, Phys. Rev. B **72**, 205124 (2005).
[87] X. J. Zhou, T. Yoshida, A. Lanzara, P. V. Bogdanov, S. A. Kellar, K. M. Shen, W. L. Yang, F. Ronning, T. Sasagawa, T. Kakeshita, T. Noda, H. Eisaki, S. Uchida, C. T. Lin, F. Zhou, J. W. Xiong, W. X. Ti, Z. X. Zhao, A. Fujimori, Z. Hussain, and Z.-X. Shen, Nature (London) **423**, 398 (2003).
[88] D. A. Bonn, Czech. J. Phys. **46**, 3195 (1996).
[89] C. Panagopoulos and T. Xiang, Phys. Rev. Lett. **81**, 2336 (1998).
[90] B. Kyung and A.-M. S. Tremblay, arXiv:cond-mat/0204500 (unpublished).
[91] Kai-Yu Yang, T. M. Rice, and Fu-Chun Zhang, Phys. Rev. B **73**, 174501 (2006).
[92] B. Valenzuela and E. Bascones, Phys. Rev. Lett. **98**, 227002 (2007).
[93] M. Aichhorn, E. Arrigoni, Z. B. Huang, and W. Hanke, Phys. Rev. Lett. **99**, 257002 (2007).
[94] W. Guyard, A. Sacuto, M. Cazayous, Y. Gallais, M. Le Tacon, D. Colson, and A. Forget, Phys. Rev. Lett. **101**, 097003 (2008).
[95] N. Doiron-Leyraud, C. Proust, D. LeBoeuf, J. Levallois, J.-B. Bonnemaison, R. Liang, D. A. Bonn, W. N. Hardy, and L. Taillefer, Nature (London) **447**, 565 (2007).
[96] R. Daou, D. LeBoeuf, N. Doiron-Leyraud, S. Y. Li, F. Laliberte, O. Cyr-Choiniere, Y. J. Jo, L. Balicas, J.-Q. Yan, J.-S. Zhou, J. B. Goodenough, and L. Taillefer, Nat. Phys. **5**, 31 (2009).
[97] F. F. Balakirev, J. B. Betts, A. Migliori, I. Tsukada, Yoichi Ando, and G. S. Boebinger, Phys. Rev. Lett. **102**, 017004 (2009).
[98] F. F. Balakirev, J. B. Betts, A. Migliori, S. Ono, Yoichi Ando, and G. S. Boebinger, Nature (London) **424**, 912 (2003).
[99] L. Hozoi, M. S. Laad, and P. Fulde, Phys. Rev. B **78**, 165107 (2008).
[100] N. M. Plakida and V. S. Oudovenko, JETP **104**, 230 (2007).
[101] A. Avella and F. Mancini, Phys. Rev. B **75**, 134518 (2007).
[102] I. E. Dzyaloshinskii, Phys. Rev. B **68**, 085113 (2003).
[103] F. H. L. Essler and A. M. Tsvelik, Phys. Rev. Lett. **90**, 126401 (2003).
[104] R. M. Konik, T. M. Rice, and A. M. Tsvelik, Phys. Rev. Lett. **96**, 086407 (2006).
[105] A. Rosch, Eur. Phys. J. B **59**, 495 (2007).
[106] R. Preuss, W. Hanke, and W. von der Linden, Phys. Rev. Lett. **75**, 1344 (1995).
[107] C. Gröber, R. Eder, and W. Hanke, Phys. Rev. B **62**, 4336 (2000).
[108] A. Kaminski, M. Randeria, J. C. Campuzano, M. R. Norman, H. Fretwell, J. Mesot, T. Sato, T. Takahashi, and K. Kadowaki, Phys. Rev. Lett. **86**, 1070 (2001).
[109] A. Lanzara, P. V. Bogdanov, X. J. Zhou, S. A. Kellar, D. L. Feng, E. D. Lu, T. Yoshida, H. Eisaki, A. Fujimori, K. Kishio, J.-I. Shimoyama, T. Noda, S. Uchida, Z. Hussain, and Z.-X. Shen, Nature (London) **412**, 510 (2001).
[110] Z.-X. Shen, A. Lanzara, S. Ishihara, and N. Nagaosa, Philos. Mag. B **82**, 1349 (2002).
[111] H. He, Y. Sidis, P. Bourges, G. D. Gu, A. Ivanov, N. Koshizuka, B. Liang, C. T. Lin, L. P. Regnault, E. Schoenherr, and B. Keimer, Phys. Rev. Lett. **86**, 1610 (2001).
[112] J. Hwang, T. Timusk, and G. D. Gu, Nature (London) **427**, 714 (2004).
[113] T. Cuk, F. Baumberger, D. H. Lu, N. Ingle, X. J. Zhou, H. Eisaki, N. Kaneko, Z. Hussain, T. P. Devereaux, N. Nagaosa, and Z.-X. Shen, Phys. Rev. Lett. **93**, 117003 (2004).
[114] K. Byczuk, M. Kollar, K. Held, Y.-F. Yang, I. A. Nekrasov, Th. Pruschke, and D. Vollhardt, Nat. Phys. **3**, 168 (2007).
[115] S. Chakraborty, D. Galanakis, and P. Phillips, Phys. Rev. B **78**, 212504 (2008).
[116] J. Graf, G.-H. Gweon, K. McElroy, S. Y. Zhou, C. Jozwiak, E. Rotenberg, A. Bill, T. Sasagawa, H. Eisaki, S. Uchida, H. Takagi, D.-H. Lee, and A. Lanzara, Phys. Rev. Lett. **98**, 067004 (2007).
[117] T. Valla, T. E. Kidd, W.-G. Yin, G. D. Gu, P. D. Johnson, Z.-H. Pan, and A. V. Fedorov, Phys. Rev. Lett. **98**, 167003 (2007).
[118] M. Z. Cieplak, A. Abal'oshev, I. Zaytseva, M. Berkowski, S. Guha, and Q. Wu, Acta Phys. Pol. A **109**, 573 (2006).
[119] G. Baskaran, Z. Zou, and P. W. Anderson, Solid State Commun. **63**, 973 (1987).
[120] A. E. Ruckenstein, P. J. Hirschfeld, and J. Appel, Phys. Rev. B **36**, 857 (1987).
[121] T. D. Stanescu and G. Kotliar, Phys. Rev. B **70**, 205112 (2004).
[122] M. Shi, J. Chang, S. Pailhés, M. R. Norman, J. C. Campuzano, M. Mansson, T. Claesson, O. Tjernberg, A. Bendounan, L. Patthey, N. Momono, M. Oda, M. Ido, C. Mudry, and J. Mesot, Phys. Rev. Lett. **101**, 047002 (2008).
[123] A. Kanigel, U. Chatterjee, M. Randeria, M. R. Norman, S. Souma, M. Shi, Z. Z. Li, H. Raffy, and J. C. Campuzano, Phys. Rev. Lett. **99**, 157001 (2007).
[124] A. Kanigel, U. Chatterjee, M. Randeria, M. R. Norman, G. Koren, K. Kadowaki, and J. C. Campuzano, Phys. Rev. Lett. **101**, 137002 (2008).
[125] S. Sachdev and J. Ye, Phys. Rev. Lett. **69**, 2411 (1992).
[126] A. Perali, C. Castellani, C. Di Castro, and M. Grilli, Phys. Rev. B **54**, 16216 (1996).
[127] S. A. Kivelson, E. Fradkin, and V. J. Emery, Nature (London) **393**, 550 (1998).
[128] C. M. Varma, Phys. Rev. Lett. **83**, 3538 (1999).
[129] Yoichi Ando, G. S. Boebinger, A. Passner, T. Kimura, and K. Kishio, Phys. Rev. Lett. **75**, 4662 (1995).
[130] G. S. Boebinger, Yoichi Ando, A. Passner, T. Kimura, M. Okuya, J. Shimoyama, K. Kishio, K. Tamasaku, N. Ichikawa, and S. Uchida, Phys. Rev. Lett. **77**, 5417 (1996).

[131] M. Ferrero, P. S. Cornaglia, L. De Leo, O. Parcollet, G. Kotliar, and A. Georges, arXiv:0806.4383 (unpublished).
[132] R. Haydock, V. Heine, and M. J. Kelly, J. Phys. C **8**, 2591 (1975).
[133] D. Poilblanc and D. J. Scalapino, Phys. Rev. B **66**, 052513 (2002).
[134] In the one-dimensional test with cluster size $N_c=2$, we could not obtain well converged solutions in the doped phase with a minimal approach ($N_b=2$ bath sites). Differently from Refs. 41 and 64, to fix bath parameters $\varepsilon_{k\sigma}$, $V_{ki\sigma}$, we adopt a minimization procedure which is not expressed by a well-defined set of n equations for n variables. In our case a minimum $N_b=4$ of bath parameters is required in order to satisfy the self-consistency relation [Eq. (7)] in the doped phase. In this two-dimension 2×2 plaquette study we could find converged solutions with $N_b=4$ bath parameters in the insulating (half-filling) case, while in doped systems solutions start to stabilize for $N_b\geq6$.
[135] V. U. Irkin, A. A. Katanin, and M. I. Katsnelson, Phys. Rev. Lett. **89**, 076401 (2002).
[136] A. N. Rubtsov, M. I. Katsnelson, A. I. Lichtenstein, and A. Georges, Phys. Rev. B **79**, 045133 (2009).